

## Quarterly Technical Report

## Solid State Research

1989:2

---

### Lincoln Laboratory

MASSACHUSETTS INSTITUTE OF TECHNOLOGY

*LEXINGTON, MASSACHUSETTS*



---

Prepared under Air Force Contract F19628-90-C-0002.

Approved for public release; distribution is unlimited.

ADA220597

This report is based on studies performed at Lincoln Laboratory, a center for research operated by Massachusetts Institute of Technology, with the support of the Department of the Air Force under Contract F19628-90-C-0002.

This report may be reproduced to satisfy needs of U.S. Government agencies.

The ESD Public Affairs Office has reviewed this report, and it is releasable to the National Technical Information Service, where it will be available to the general public, including foreign nationals.

This technical report has been reviewed and is approved for publication.

FOR THE COMMANDER

*Hugh L. Southall*

Hugh L. Southall, Lt. Col., USAF  
Chief, ESD Lincoln Laboratory Project Office

Non-Lincoln Recipients

**PLEASE DO NOT RETURN**

Permission is given to destroy this document  
when it is no longer needed.



**MASSACHUSETTS INSTITUTE OF TECHNOLOGY  
LINCOLN LABORATORY**

**SOLID STATE RESEARCH**

**QUARTERLY TECHNICAL REPORT**

**1 FEBRUARY — 30 APRIL 1989**

**ISSUED 30 NOVEMBER 1989**

**Approved for public release; distribution is unlimited.**

**LEXINGTON**

**MASSACHUSETTS**

## **ABSTRACT**

This report covers in detail the research work of the Solid State Division at Lincoln Laboratory for the period 1 February through 30 April 1989. The topics covered are Electrooptical Devices, Quantum Electronics, Materials Research, Submicrometer Technology, Microelectronics, and Analog Device Technology. Funding is provided primarily by the Air Force, with additional support provided by the Army, DARPA, Navy, SDIO, NASA, and DOE.



## TABLE OF CONTENTS

Abstract	iii
List of Illustrations	vii
List of Tables	xi
Introduction	xiii
Reports on Solid State Research	xv
Organization	xxv
<b>1. ELECTROOPTICAL DEVICES</b>	<b>1</b>
1.1 Theoretical Comparison of Lumped-Element and Traveling-Wave Integrated-Optic Phase Modulators	1
1.2 Comparison of the Thermal Stability of Semi-insulating InP:Fe and InP:Ti:Hg	4
1.3 Wafer Fusion by Mass Transport: A New Technique for Monolithic Integration	8
1.4 Mass Transport of GaInP	11
1.5 External Cavity Operation of InGaAsP Diode Laser Arrays	13
<b>2. QUANTUM ELECTRONICS</b>	<b>21</b>
2.1 Gain-Switched Pulsed Operation of Microchip Lasers	21
2.2 Suppression of Laser Spiking by Intracavity Second-Harmonic Generation	23
2.3 Scalable End-Pumped Nd:YAG Laser	29
2.4 Lateral-Mode Structure of External-Cavity Diode Lasers with Residual Facet Reflectivity	31
<b>3. MATERIALS RESEARCH</b>	<b>39</b>
3.1 Determination of MBE Growth Rate by Digital Signal Processing of Time-Dependent RHEED Intensity Data	39
<b>4. SUBMICROMETER TECHNOLOGY</b>	<b>43</b>
4.1 Optical Properties of Fused Silica Exposed to 193-nm Radiation from an Excimer Laser	43
4.2 Fabrication of Regrowth Field Effect Transistor Test Structures by Electron Beam Lithography	48
<b>5. MICROELECTRONICS</b>	<b>55</b>
5.1 Resonant-Tunneling Oscillators up to 420 GHz	55
5.2 Observation of Optically Pumped Intersubband Emission from Quantum Wells	58
5.3 Casting Process for Multichip Interconnects	53

## TABLE OF CONTENTS (Continued)

6.	ANALOG DEVICE TECHNOLOGY	67
6.1	Atomic Oxygen Source for Superconducting Films	67
6.2	Hybrid Analog/Digital Circuitry for a Superconductive Time-Integrating Correlator	71

## LIST OF ILLUSTRATIONS

Figure No.		Page
1-1	Schematic illustration of a lumped-element channel-waveguide electrooptic phase modulator. The phase modulation is proportional to the product of the applied voltage $V(t)$ and the electrode length $L$ .	1
1-2	Equivalent circuit containing the lumped-element phase modulator, electrical source, and matching circuit.	1
1-3	Equivalent circuit containing a traveling-wave modulator with electrode impedance $Z_m$ , matched termination, electrical source, and matching circuit.	2
1-4	Response of a lumped-element (LE) and traveling-wave (TW) modulator as a function of electrode length at a modulation frequency of 1 GHz. Impedance-matched operation is assumed. For $L > 20$ mm, approximations employed to calculate lumped-element operation are not valid.	3
1-5	SIMS profiles of Fe in semi-insulating InP:Fe for (a) an annealed substrate and (b) a substrate annealed at 800°C for 30 min with a $\text{Si}_3\text{N}_4$ encapsulant.	5
1-6	SIMS profiles of Ti and Hg in semi-insulating InP:Ti:Hg for (a) and (c), an unannealed substrate, and (b) and (d), a substrate annealed at 800°C for 30 min with a $\text{Si}_3\text{N}_4$ encapsulant.	6
1-7	Sheet-carrier concentration and mobility vs EOP-RTA anneal temperature for InP:Fe and InP:Ti:Hg samples implanted with $6 \times 10^{12} \text{ cm}^{-2}$ of 400-keV $\text{Si}^+$ at room temperature.	7
1-8	Schematic drawing of the transverse cross-sectional view of the wafer-fusion reactor. The actual device has an overall diameter of 2.5 cm and a length (in the direction perpendicular to the page) of 4 cm.	9
1-9	Optical micrographs showing (a) the cleaved cross section of the fused wafer and (b) the magnified view of a fused region. In (a), the long cavities between the fused regions are etched regions in one of the original wafers. In the fused region in (b), two small cavities can be seen (near center and left edge of the photograph).	10
1-10	Scanning electron micrographs of cleaved GaInP/GaAs DH structure with etched mesas before (top) and after (bottom) mass transport. There is a slight magnification difference between the two pictures.	12
1-11	(a) Optical micrograph of mass-transported two-dimensional microlens array. (b) Images formed by the microlenses.	14
1-12	Schematic of external-cavity elements and diagnostic optics.	15



## LIST OF ILLUSTRATIONS (Continued)

Figure No.		Page
1-13	Light-current characteristics of laser array with and without feedback from the external mirror.	15
1-14	Far-field patterns (a) and (c) and spatially resolved spectra (b) and (d) of the external cavity output. (a) and (b) are for incoherent operation, (c) and (d) for coherent operation of four elements with the spatial filter in the cavity.	16
2-1	Deconvolved output pulse of a Nd:YAG microchip laser when pumped with a 40-ns Ti:Al <sub>2</sub> O <sub>3</sub> pulse. The microchip laser cavity is 750 $\mu$ m long, with a 1.3 percent output coupler.	22
2-2	Temporal profiles of 160-mJ, TEM <sub>00</sub> , 1.06- $\mu$ m laser pulses (a) without intracavity second-harmonic generation and (b) with intracavity second-harmonic generation.	24
2-3	Leading edges of 1.06- $\mu$ m laser pulses (a) without intracavity second-harmonic generation and (b) with intracavity second-harmonic generation.	25
2-4	Temporal profile of 1.06- $\mu$ m spike-suppressed pulse after the leading spikes were “clipped” off by an external Pockel’s cell and the resulting 150-mJ pulse was amplified in a single-pass amplifier to 1.1 J.	26
2-5	Temporal profiles of mode-locked 1.06- $\mu$ m laser pulse with intracavity second-harmonic generation.	27
2-6	Temporal profiles of 70-mJ, TEM <sub>00</sub> , 1.32- $\mu$ m laser pulses (a) without intracavity second-harmonic generation and (b) with intracavity second-harmonic generation.	28
2-7	Schematic of the scalable end-pumped laser experiment. (a) Plane perpendicular to the junction. (b) Plane parallel to the junction.	30
2-8	Continuous wave output power as a function of input power for the middle array and all three arrays. The output for the other two arrays operating individually are not shown for reasons of clarity, but their output powers are slightly less than the middle array.	31
2-9	Schematic of the external-cavity laser.	32
2-10	(a) Power vs current for apertured external-cavity laser. The aperture permits single-frequency operation at current up to the threshold, $I_t$ , of a solitary diode indicated in the figure. (b) Power vs current for same laser without aperture.	33
2-11	(a) Fabry-Perot spectrum of output from a 0.6-W external-cavity laser with displaced feedback, showing predominant single-frequency component of spectrum. (b) Monochromator (low-resolution) spectrum of	

## LIST OF ILLUSTRATIONS (Continued)

Figure No.		Page
	laser output showing strong single-frequency signal from the region of the diode with strong feedback, and broad hump originating from the region of the diode with weak optical feedback.	34
2-12	Spatially resolved nearfield spectrum of diode in external cavity with displaced feedback. The bright, single-frequency spot and the broad, weaker spectrum originate from distinct spatial regions of the diode.	35
2-13	Spatially resolved nearfield spectrum of diode in external cavity with insufficient mode selectivity resulting from residual Fabry-Perot effects. Each lateral mode repeats at regular intervals corresponding to about four axial diode-mode spacings. Many lateral modes have similar net gain.	36
3-1	RHEED signal vs time for growth of GaAs on (100) GaAs substrate.	40
3-2	RHEED signal vs time for growth of GaAs on inferior (100) GaAs substrate.	40
3-3	Power spectrum obtained by digital signal processing of RHEED data for experiment of Figure 3-2.	41
4-1	Absorption spectrum of high-OH fused silica, induced by pulsed irradiation at 193 nm. The spectrum has been corrected for reflective and absorptive losses in unexposed areas of the same sample. The inset shows the spatial distribution of transmitted 632.8-nm light when the fused silica sample was placed between two crossed linear polarizers. The nonzero transmission is caused by stress birefringence in an annular area surrounding the excimer laser spot.	44
4-2	Variation of the absorption coefficient at 215 nm (E' centers) and the stress birefringence (square root of induced 633-nm transmission) with sample temperature during 193-nm irradiation. The measurements were performed at room temperature. Exposure conditions were 17 mJ cm <sup>-2</sup> /pulse and $1.4 \times 10^6$ pulses at 100 Hz.	45
4-3	Effect of irradiation history on the 215-nm absorption coefficient and the 633-nm stress birefringence. Three regimes are noted: (i) a linear increase at high (50 mJ cm <sup>-2</sup> /pulse) fluence, up to $\sim 10^6$ pulses; (ii) a sublinear increase at the high fluence for the next $\sim 1.5 \times 10^6$ pulses; and (iii) partial bleaching but no change in birefringence upon reducing the fluence to 12 mJ cm <sup>-2</sup> /pulse.	46
4-4	Layout of the "fan" test pattern. The details of each radial line cluster are shown in the inset.	49

## LIST OF ILLUSTRATIONS (Continued)

Figure No.		Page
4-5	Cross-sectional views illustrating the process for making RFET gratings: (a) initial multilayer stack, (b) after e-beam patterning and nickel evaporation, (c) after liftoff, and (d) after reactive-ion etching.	50
4-6	Effect of an astigmatic (ellipsoidal) spot on the linewidth produced when an electron beam is scanned at different angles. In addition to the purely geometric effect illustrated here, the dose per unit area is changed, affecting the developed width of the line.	51
4-7	Effect of field size on the stitching accuracy and lithographic quality of exposed features: (a) 150- $\mu\text{m}$ field and (b) 100- $\mu\text{m}$ field.	52
4-8	Nickel pattern produced by liftoff after electron beam exposure, showing the quality of stitching at a field boundary.	53
5-1	Experimental and theoretical power for a 4- $\mu\text{m}$ -diam. diode. The quantities $f_{\text{RCL}}$ and $f_{\text{RC}}$ are maximum oscillation frequencies calculated from the equivalent circuit shown in the inset. This circuit includes the differential conductance $G$ , the diode capacitance $C$ , the quantum-well inductance $L_{\text{QW}}$ , and the series resistance $R_{\text{S}}$ .	55
5-2	Cross-sectional schematic view of the GaAs/AlAs wafer used to fabricate diodes that oscillated up to 420 GHz.	56
5-3	Experimental current-voltage curve (solid and dotted) and the theoretical curve (dashed) for a representative 4- $\mu\text{m}$ -diam. diode at room temperature. The chair-like structure of the experimental curve is caused by self-detection of oscillations.	57
5-4	Transmission spectrum for coupled quantum wells at 25 K. Measurement was made with p-polarized light incident at Brewster's angle. The higher energy absorption is identified as the $E_1$ - $E_4$ transition, the lower as the $E_2$ - $E_3$ transition. The arrows mark the two energies used to pump the sample for far-infrared emission	59
5-5	Pump and emission geometry for measuring far-infrared emission.	
5-6	Far-infrared emission by coupled quantum wells. The peak at 17 meV is attributed to the $E_4$ - $E_3$ transition. The dashed line is the calculated radiation from $\text{Al}_{0.27}\text{Ga}_{0.73}\text{As}$ at 100 K	60
5-7	Multichip-integration casting technique. (a) IC chips are positioned and planarized with a custom RTV mold, and then affixed to adhesive. (b) RTV mold is removed leaving chips planarized on adhesive in precise alignment. (c) Glass frame is set on the adhesive to define the substrate, and filled with epoxy. (d) Epoxy with chips embedded is separated from the glass and the adhesive is removed. Circuits are then interconnected with standard photolithography and metallization.	63



## LIST OF ILLUSTRATIONS (Continued)

Figure No.		Page
5-8	(a) Completed multichip optical receiver. (b) Circuit diagram of preliminary test measurement. (c) Measured waveform at the amplifier output in response to a 2-GHz amplitude modulation signal detected by the photodiode.	64
6-1	Inductively coupled plasma source of atomic oxygen.	68
6-2	Measurement of atomic-oxygen flux by microbalance assay of oxygen captured in silver film.	69
6-3	Mass gain of silver film bombarded by atomic oxygen as a function of exposure time.	
6-4	Block diagram of superconductive time-integrating correlator. The prototype chip which was tested contains the elements enclosed by the dashed box.	69
6-5	Oscilloscope waveforms showing test structure operation for (a) 0.5- $\mu$ s integration and (b) 3- $\mu$ s integration. The left-hand side shows the input to the MIP cell (top trace), address-encoder supply current (middle), and current input to Josephson junction peak detector (bottom). The right-hand side shows the address-encoder outputs (expanded time scale) during the presence of the peak-detector ramp.	74
6-6	Photomicrograph of 14-channel superconductive time-integrating correlator.	75

## LIST OF TABLES

Table No.		Page
6-1	Influence of Gas Flow and Composition on Oxygen Atomic Flux	70
6-2	Transmission of Atomic Oxygen Through Tubes of Different Materials	71

# INTRODUCTION

## 1. ELECTROOPTICAL DEVICES

The theoretical performances of impedance-matched lumped-element and traveling-wave integrated-optical phase modulators have been compared. For  $\text{LiNbO}_3$  devices operating at  $1.3\ \mu\text{m}$  with modulation frequencies up to several gigahertz, the theoretical impedance-matched response of lumped-element modulators exceeds that of traveling-wave modulators if the product of the modulation frequency and electrode length is below 20 GHz-mm.

A preliminary comparison has been made between the dopant redistribution behavior in heat-treated semi-insulating  $\text{InP:Fe}$  substrates and that in heat-treated  $\text{InP:Ti:Hg}$  substrates. SIMS analysis indicates that the diffusivity of Ti in InP is much lower than that of Fe, and sheet Hall measurements performed on  $\text{Si}^+$ -implanted substrates show that electrical activation of Si does not degrade in  $\text{InP:Ti:Hg}$  as the annealing temperature is increased.

A special reactor, which exploits the large difference in thermal expansion between quartz and graphite, has been designed and used to strongly compress two InP wafers at high temperatures and fuse them together through mass transport. This fusion technique offers new possibilities for monolithic integration.

Mass transport of GaInP lattice matched to GaAs has been successfully demonstrated in two different double heterostructures. This first reported use of alloy semiconductor mass transport opens the way for applying that powerful fabrication technology to GaAs-based devices, in particular to GaInAsP/GaAs lasers.

Coherent operation of four devices in a 5-element linear array of InGaAsP diode lasers has been achieved in an external cavity. Narrow, multilobe far-field patterns with  $\sim 65$  percent of the energy in the central peak were obtained.

## 2. QUANTUM ELECTRONICS

Single-frequency, gain-switched pulses as short as 120 ps have been obtained with a microchip laser, and much shorter pulses are possible. The short microchip laser cavity allows rapid buildup of the gain-switched pulses.

Laser spiking in a long-pulse, pulse-pumped Nd:YAG laser has been substantially suppressed by intracavity second-harmonic generation. This technique is easy to implement and results in  $<1$  percent loss of laser pulse energy.

A pumping scheme using multiple diode arrays that offers the potential for an order of magnitude power scaling of end-pumped lasers has been experimentally demonstrated. Diffraction-limited output with a power of 520 mW has been obtained from an Nd:YAG laser pumped with three diode laser arrays.

A 0.35-W, single-frequency laser has been demonstrated using a wide-stripe diode in an external cavity. The residual reflectivity of antireflection coatings degrades lateral mode-selectivity, thus imposing limits on the brightness of this laser.

### 3. MATERIALS RESEARCH

The growth rate of epitaxial layers can be accurately determined by measuring the temporal period of reflection high energy electron diffraction (RHEED) oscillations generated during growth by molecular beam epitaxy. A digital signal-processing technique has been developed for extracting this period from RHEED signals obtained under growth conditions that do not yield oscillations sufficiently obvious to permit the period to be obtained directly from plots of intensity vs time.

### 4. SUBMICROMETER TECHNOLOGY

Changes in the optical properties of OH-rich fused silica exposed to pulsed 193-nm radiation from an ArF laser have been studied. Prolonged irradiation results in increased 193-nm absorption, changes in refractive index, and compaction of the fused silica which produces stress-induced birefringence.

In order to study growth of GaAs through the gate fingers of a regrowth field effect transistor, test patterns consisting of 450-nm-period gratings at varying orientations have been fabricated by direct-write electron beam lithography. Optimization of the exposure conditions has yielded satisfactory patterning, and test structures can now be produced routinely.

### 5. MICROELECTRONICS

GaAs resonant-tunneling diodes operating at room temperature have yielded fundamental oscillations up to frequencies of 420 GHz. These oscillations are consistent with a generalized impedance model for the resonant-tunneling diode that accounts for an inductive delay intrinsic to coherent resonant tunneling, and a transit-time delay associated with the relatively long depletion layer on the anode side of the tunnel structure.

Radiative transitions by optically excited carriers between subbands of a quantum-well structure have been observed. Excitation by a CO<sub>2</sub> laser operating at a photon energy of 133 meV produced emission with peak energy at 17 meV and a full width at half-maximum of 3 meV.

A multichip casting process has been demonstrated that allows the precise location and integration of chips fabricated with different materials and technologies. The interconnects for a multichip integrated optical receiver were defined in one standard photolithographic step directly on the epoxy casting and coplanar chip surfaces and then metallized using Au electroplating.

### 6. ANALOG DEVICE TECHNOLOGY

An inductively coupled plasma oxygen source has been fabricated that produces an atomic flux greater than  $5 \times 10^{15}$  atoms cm<sup>-2</sup> s<sup>-1</sup> and has decomposition efficiency higher than 25 percent. This source will be used for the *in-situ* deposition of superconductive Y-Ba-Cu-O thin films.

On-chip integration of wideband (multigigahertz) analog superconductive electronics with superconductive digital electronics has been achieved with the fabrication and testing of an analog correlator coupled to digital readout circuitry. The device, in correlating two 4-GHz tones, showed a readout dynamic range of 37 dB.



# REPORTS ON SOLID STATE RESEARCH

1 February Through 30 April 1989

## PUBLISHED REPORTS

### Journal Articles

#### JA No.

6068	Analysis of Conduction in Fully Depleted SOI MOSFET's	K.K. Young	IEEE Trans. Electron Devices <b>ED-36</b> , 504 (1989)
6129	Reactive Ion Etching of GaAs and AlGaAs in a BCl <sub>3</sub> -Ar Discharge	S.S. Cooperman* H.K. Choi H.H. Sawin* D.F. Kolesar	J. Vac. Sci. Technol. B <b>7</b> , 41 (1989)
6147	Effects of Noble Gases on the Properties of Ion Beam Sputtered Niobium Films	D.J. Lichtenwalner A.C. Anderson D.A. Rudman*	J. Vac. Sci. Technol. A <b>7</b> , 102 (1989)
6176	Transport and Kinetics	H.J. Zeiger D.J. Ehrlich J.Y. Tsao*	In <i>Laser Microfabrication: Thin Film Processes and Lithography</i> , D.J. Ehrlich, Ed. (Academic Press, Cambridge, Massachusetts, 1989), p. 285
6179	Optically Induced Nonresonant Changes in the Refractive Index of Ti:Al <sub>2</sub> O <sub>3</sub>	K.F. Wall R.L. Aggarwal M.D. Sciacca H.J. Zeiger R.E. Fahey A.J. Strauss	Opt. Lett. <b>14</b> , 180 (1989)
6180	Novel Scalloped-Mirror Diffraction-Coupled InGaAsP/InP Buried-Heterostructure Laser Arrays	D. Yap J.N. Walpole Z.L. Liao	Appl. Phys. Lett. <b>54</b> , 687 (1989)

---

\* Author not at Lincoln Laboratory.

# JA No.

- |      |  |   |   |
|------|--|---|---|
| 6183 | Defect-Related Dielectric Break-down, Charge Trapping, and Interface-State Generation of Gate Oxides Grown on Zone-Melting-Recrystallized Silicon-on-Insulator Films | C-T.Lee<br>C.K. Chen  | J. Appl. Phys. <b>65</b> , 646 (1989)             |
| 6185 | Measurement of the Wave Front of a Pulsed Dye Laser Using an Integrated-Optics Sensor with 200-nsec Temporal Resolution  | R.H. Rediker<br>B.G. Zollars<br>T.A. Lind<br>R.E. Hatch<br>B.E. Burke   | Optics Lett. <b>14</b> , 381 (1989)               |
| 6187 | Preparation of Superconducting Bi-Sr-Ca-Cu-O Thin Films by Sequential Electron Beam Evaporation and Oxygen Annealing   | J. Steinbeck*<br>A.C. Anderson<br>B-Y. Tsaur<br>A.J. Strauss  | Appl. Phys. Lett. <b>54</b> , 466 (1989)          |
| 6208 | Effect of Quasibound-State Lifetime on the Oscillation Power of Resonant Tunneling Diodes  | E.R. Brown<br>C.D. Parker<br>T.C.L.G. Sollner   | Appl. Phys. Lett. <b>54</b> , 934 (1989)          |
| 6211 | Picosecond GaAs-Based Photoconductive Optoelectronic Detectors   | F.W. Smith<br>H.Q. Le<br>V. Diadiuk<br>M.A. Hollis<br>A.R. Calawa<br>S. Gupta*<br>M. Frankel*<br>D.R. Dykaar*<br>G.A. Mourou*<br>T.Y. Hsiang* | Appl. Phys. Lett. <b>54</b> , 890 (1989)          |
| 6226 | Selective Area Laser Photo-deposition of Transparent Conductive SnO <sub>2</sub> Films   | R.R. Kunz<br>M. Rothschild<br>D.J. Ehrlich  | Appl. Phys. Lett. <b>54</b> , 1631 (1989)         |
| 6253 | Early Work at Lincoln Laboratory on GaAs Semiconductor Devices   | R.H. Rediker  | Lincoln Laboratory Journal <b>2</b> , 3 (1989)    |
| 6267 | Mass-Transported GaInAsP/InP Lasers  | Z.-L. Liao<br>J.N. Walpole  | Lincoln Laboratory Journal <b>2</b> , 77 (1989)   |
| 6268 | Emerging Composite Semiconductor Materials for the Next Generation of Electronics and Photonics  | J.C.C. Fan*<br>B-Y. Tsaur   | Electron. Eng. Times, Issue No. 530 (1989), p. T4 |

---

\* Author not at Lincoln Laboratory.

## Meeting Speeches

### MS No.

7741A	Integrated-Optical Interferometric 2 × 2 Switches	L.M. Johnson H.V. Roussel	<i>Integrated Optical Circuit Engineering</i> , M.A. Mentzer, Ed., Proc. SPIE <b>993</b> , 76-79 (1989)
7919A	Monolithic Two-Dimensional Surface-Emitting Arrays of GaAs/AlGaAs Diode Lasers	J.P. Donnelly W.D. Goodhue K. Rauschenbach D.A. Seielstad C.A. Wang R.J. Bailey	Proc. IEEE Lasers and Electro-Optics Society, Santa Clara, California, 2-4 November 1988, p. 450
7927A	1 Gb/s Free-Space Optical Interconnection Between Digital Circuits	D.Z. Tsang	Proc. IEEE Lasers and Electro-Optics Society, Santa Clara, California, 2-4 November 1988, p. 11
7927B	Free-Space Optical Interconnects	D.Z. Tsang	<i>Optoelectronic Materials, Devices, Packaging, and Interconnects II</i> , G.M. McWright and H.J. Wojtunik, Eds., Proc. SPIE <b>994</b> , 73-76 (1989)
7947	Superconducting Thin Films of BiSrCaCuO Made by Sequential Electron-Beam Evaporation	J. Steinbeck* A.C. Anderson B-Y. Tsaur A.J. Strauss	IEEE Trans. Magn. <b>MAG-25</b> , 2429 (1989)
7948	Low-Loss Lumped-Element Capacitors for Superconductive Integrated Circuits	M. Bhushan J.B. Green A.C. Anderson	IEEE Trans. Magn. <b>MAG-25</b> , 1143 (1989)
7950	Process Control for the Low- Temperature Deposition of Niobium-Nitride Thin Films	A.C. Anderson D.J. Lichtenwalner W.T. Brogan	IEEE Trans. Magn. <b>MAG-25</b> , 2084 (1989)
7951	Processing of Thick-Film Dielectrics Compatible with Thin- Film Superconductors for Analog Signal Processing Devices	S.C. Wong* A.C. Anderson D.A. Rudman*	IEEE Trans. Magn. <b>MAG-25</b> , 1255 (1989)
7957	High-Sensitivity Bandpass RF Modulator in LiNbO <sub>3</sub>	G.E. Betts L.M. Johnson C.H. Cox	<i>Integrated Optical Circuit Engineering VI</i> , M.A. Mentzer, Ed., Proc. SPIE <b>993</b> , 110-116 (1988)

---

\* Author not at Lincoln Laboratory.



**MS No.**

- |      |   |  |   |
|------|---|--|---|
| 7964 | Dependence of Y-Branch Loss on Waveguide Mode Confinement   | R.H. Rediker<br>L.M. Eriksen<br>T.A. Lind  | <i>Optoelectronic Materials, Devices, Packaging, and Interconnects II</i> , G.M. McWright and H.J. Wojtunik, Eds., Proc. SPIE <b>994</b> , 212-216 (1989) |
| 7998 | Reduction of Intermodulation Distortion in Interferometric Optical Modulators                               | L.M. Johnson<br>H.V. Rousell   | Proc. IEEE Lasers and Electro-Optics Society, Santa Clara, California, 2-4 November 1988, p. 119  |
| 8001 | SAW/FET Programmable Filter with Varistor Taps for Improved Performance                                     | D.E. Oates<br>D.L. Smythe<br>J.B. Green<br>R.S. Withers  | 1988 IEEE Ultrasonics Symposium Proceedings (IEEE, New York, 1988), p. 155  |
| 8008 | Microchannel Heat Sinks and Microlens Arrays for High-Average-Power Diode Laser Arrays                      | J.N. Walpole<br>Z.L. Liao<br>V. Diadiuk<br>L.J. Missaggia  | Proc. IEEE Lasers and Electro-Optics Society, Santa Clara, California, 2-4 November 1988, p. 447  |
| 8017 | A Comparison of Superconductive and Surface-Acoustic-Wave Signal Processing                                 | R.S. Withers   | 1988 IEEE Ultrasonics Symposium Proceedings (IEEE, New York, 1988), p. 185  |
| 8022 | The Effect of Varying the Input Polarization on an External Cavity Controlled Ensemble of Five Diode Lasers | L.Y. Pang<br>C. Corcoran<br>R.H. Rediker   | Proc. IEEE Lasers and Electro-Optics Society, Santa Clara, California, 2-4 November 1988, p. 481  |
| 8036 | Plasma-Activated Ion Beam Reactive Sputtering of NbN Thin Films   | D.J. Lichtenwalner<br>A.C. Anderson<br>D.A. Rudman*  | Materials Research Society Symp. Proc., Vol. 128, 1989, p. 67   |
| 8145 | An Abutable CCD Imager for Visible and X-Ray Focal Plane Arrays   | B.E. Burke<br>R.W. Mountain<br>D.C. Harrison*<br>G.R. Ricker*<br>M.W. Bautz*<br>J. Doty*<br>J.H. Reinold<br>C.L. Doherty | Technical Digest, 1989 Intl. Solid-State Circuits Conf. (IEEE, New York, 1989), p. 94   |

---

\* Author not at Lincoln Laboratory.

**MS No.**

- |      |   |   |   |
|------|---|---|---|
| 8197 | The Effect of Quasibound State Lifetime on the Speed of Resonant-Tunneling Diodes | E.R. Brown<br>C.D. Parker<br>T.C.L.G. Sollner<br>C.I. Huang*<br>C.E. Stutz*   | 4th Topical Mtg. on Pico-second Electronics and Optoelectronics, Salt Lake City, Utah, 8-10 March 1989, Technical Digest, paper WD4, p. 46  |
| 8233 | Picosecond GaAs-Based Photoconductive Optoelectronic Detectors                    | F.W. Smith<br>S. Gupta*<br>H.Q. Le<br>M. Frankel*<br>V. Diadiuk<br>M.A. Hollis<br>D.R. Dykaar*<br>G.A. Mourou*<br>T.Y. Hsiang*<br>A.R. Calawa | 4th Topical Mtg. on Pico-second Electronics and Optoelectronics, Salt Lake City, Utah, 8-10 March 1989, Technical Digest, paper FB1, p. 120 |
| 8250 | The Permeable Base Transistor: An Update  | C.O. Bozler   | 4th Topical Mtg. on Pico-second Electronics and Optoelectronics, Salt Lake City, Utah, 8-10 March 1989, Technical Digest, paper THA3, p. 85 |

**UNPUBLISHED REPORTS****Journal Articles****JA No.**

- |      |   |  |                                       |
|------|---|--|---------------------------------------|
| 6215 | Sum-Frequency Generation of Sodium-Resonance Radiation                            | T.H. Jeys<br>A. Mooradian<br>A.A. Brailove                         | Accepted by Appl. Opt.                |
| 6225 | End-Pumped Nd:LaF <sub>3</sub> and Nd:LaMgAl <sub>11</sub> O <sub>19</sub> Lasers | T.Y. Fan<br>M.R. Kokta*  | Accepted by IEEE J. Quantum Electron. |
| 6232 | A New Approach to Modeling Heteroepitaxy, as Illustrated by GaAs on Si (100)      | E. Kaxiras*<br>O.L. Alerhand*<br>J.D. Joannopoulos*<br>G.W. Turner | Accepted by Phys. Rev. Lett.          |

---

\* Author not at Lincoln Laboratory.

**JA No.**

- |      |   |   |  |
|------|---|---|--|
| 6235 | High-Power, Diffraction-Limited, Narrow-Band, External Cavity Diode Laser                                       | W.F. Sharfin<br>J. Seppala<br>A. Mooradian<br>B.A. Soltz*<br>R.G. Waters*<br>B.J. Vollmer*<br>K.J. Bystrom* | Accepted by Appl. Phys. Lett.  |
| 6249 | Relative Performance of Impedance-Matched Lumped-Element and Traveling-Wave Integrated-Optical Phase Modulators | L.M. Johnson  | Accepted by Photonics Technol. Lett  |
| 6260 | Lamp Shop Hint  | D.L. Hovey<br>J.N. McMillan   | Accepted by Fusion, J. Amer. Scientific Glassblowers Society   |
| 6262 | Superconductive Analog Signal Processing  | R.S. Withers<br>R.W. Ralston  | Accepted by Proc. IEEE   |
| 6263 | 128 × 128-Element IrSi Schottky-Barrier Focal Plane Arrays for Long-Wavelength Infrared Imaging                 | B-Y. Tsaur<br>M.J. McNutt*<br>R.A. Bredthauer*<br>R.B. Mattson*   | Accepted by IEEE Electron Device Lett.   |
| 6265 | Microchannel Heat Sinks for Two-Dimensional High-Power-Density Diode Laser Arrays                               | L.J. Missaggia<br>J.N. Walpole<br>Z.L. Liao<br>R.J. Phillips  | Accepted by IEEE J. Quantum Electron.  |
| 6280 | Microchip Lasers  | J.J. Zayhowski<br>A. Mooradian  | OSA Proceedings of Topical Mtg. on Tunable Solid State Lasers, North Falmouth, Massachusetts, 1-3 May 1989 |

**Meeting Speeches†****MS No.**

- |       |  |                           |  |
|-------|--|---------------------------|--|
| 7762A | Surface-Emitting Diode Lasers, Semiconductor Microlenses and High-Power Two-Dimensional Arrays | Z.L. Liao                 | Seminar, Bellcore Communications Research, Morristown, New Jersey, 24 March 1989                       |
| 8025A | Laser Bilayer Etching of GaAs Surfaces   | P.A. Maki<br>D.J. Ehrlich | Topical Mtg. on Microphysics of Surfaces, Beams, and Adsorbates, Salt Lake City, Utah, 2 February 1989 |

---

\* Author not at Lincoln Laboratory.

† Titles of Meeting Speeches are listed for information only. No copies are available for distribution.

MS No.

8113	The Extinction Ratio in Optical Two-Guide $\Delta\beta$ Couplers	J.P. Donnelly L.A. Molter* G.S. Hopcraft* R.E. Smith* H.A. Haus*	IGWO '89, Houston, Texas, 6-8 February 1989
8118	Reduced Confinement GaAlAs Tapered Waveguide Antennas	D.E. Bossi W.D. Goodhue R.H. Rediker	
8125	Microwave Bandpass Modulators in Lithium Niobate	G.E. Betts	
8121A	High-Power, Diffraction-Limited, Narrow-Band External Cavity Diode Laser	W.F. Sharfin J.P. Seppala A. Mooradian B.A. Soltz* R.G. Waters* B.J. Vollmer* K.J. Bystrom*	CLEO '89, Baltimore, Maryland, 24-28 April 1989
8209A	Femtosecond Pump-Probe Interferometry Studies of Optical Switching in AlGaAs Waveguides	K.K. Anderson M.J. Lagasse* H.A. Haus* C.A. Wang J.G. Fujimoto*	
8218	A Multistage Ti:Al <sub>2</sub> O <sub>3</sub> Amplifier System	K.F. Wall P. Lacovara R.L. Aggarwal P.A. Schulz A. Sanchez	
8219	High-Sensitivity Optical Analog Link Using External Modulator	G.E. Betts L.M. Johnson C.H. Cox III S.D. Lowney	
8220	Tunable Single-Frequency Nd:YAG Microchip Lasers	J.J. Zayhowski A. Mooradian	
8222	N-Type InSb 10- $\mu$ m Faraday Isolator	R.L. Aggarwal R.F. Lucey, Jr. D.P. Ryan-Howard H.J. Jimenez-Gonzales K.H. Yoo*	

\* Author not at Lincoln Laboratory.



MS No.

8229	Sum-Frequency Mixing of Frequency-Modulated Laser Radiation	T.H. Jeys	CLEO '89, Baltimore, Maryland 24-28 April 1989
8235	Wavelength-Independent Faraday Isolator	P.A. Schulz	
8262	Mode-Locked Ti:Al <sub>2</sub> O <sub>3</sub> Laser with a Nonlinear Coupled External Cavity	J. Goodberlet* J. Wang* J.G. Fujimoto* P.A. Schulz S.R. Henion	
8274	III-V Compounds and Optical Computing	R.C. Williamson	
8134	Growth of Ti:YAlO <sub>3</sub> for Tunable Solid State Laser Applications	C.P. Khattak* F. Schmid* K.F. Wall R.L. Aggarwal	SPIE '89 Aerospace Sensing Symp., Orlando, Florida, 27-31 March 1989
8378	Planar Diode-Laser Pump Arrays for Solid-State Laser Radars	R.C. Williamson J.P. Donnelly K. Rauschenbach C.A. Wang H.K. Choi W.D. Goodhue J.N. Walpole R.J. Bailey L.J. Missaggia	
8169	YBa <sub>2</sub> Cu <sub>3</sub> O <sub>x</sub> Thin Films Prepared by Sequential Sputtering of Y <sub>2</sub> O <sub>3</sub> , BaF <sub>2</sub> , and CuO Targets	M. Bhushan A.J. Strauss	
8185A	Progress in Diode Pumped Solid State Lasers	T.Y. Fan	
8185B	Progress in Diode Pumped Solid State Lasers	T.Y. Fan	Seminar, Raytheon Research Division, Lexington, Massachusetts, 8 March 1989

---

\* Author not at Lincoln Laboratory.

# MS No.

8210	Alignment and Performance Tradeoffs for Free-Space Optical Interconnections	D.Z. Tsang	3rd Topical Mtg. on Optical Computing, Salt Lake City, Utah, 27 February-1 March 1989
8227	Electronic vs Optical Implementations of Neural Networks	J.P. Sage B.F. Aull	
8249	Observation of a Spin Density Wave in $\text{La}_2\text{CuO}_4$ by Raman Scattering	H.J. Zeiger A.J. Strauss G. Dresselhaus* Y.C. Liu* P.J. Picone* M.S. Dresselhaus*	American Physical Society Mtg., St. Louis, Missouri, 20-24 March 1989
8251	GaAs-on-Si for Monolithic Microwave Integrated Circuits	G.W. Turner	
8252	High-Speed Resonant Tunneling	E.R. Brown	
8257	The Use of the Integrated Optics Wavefront Measurement Sensor in Passive Ranging Applications	R.H. Rediker	IRIS Passive Sensors Specialty Group, Moffett Field, California, 14-16 March 1989
8299	A Review of Laser-Microchemical Processing	D.J. Ehrlich	Congress on Gases for Electronics, Versailles, France, 28-30 March 1989
8299A	A Review of Laser-Microchemical Processing	D.J. Ehrlich	Beam-Solid Interactions, Ankara, Turkey, 24-27 April 1989
8325	Two-Dimensional Surface-Emitting Diode Laser Arrays	R.C. Williamson	Lincoln Laboratory Technical Seminars Series, Rensselaer Polytechnic Institute, Troy, New York, 23 February 1989
8326	In Situ Etching of GaAs with Monolayer Control	P.A. Maki	Workshop on Compound Semiconductor Material and Devices, Hilton Head, South Carolina, 20 February 1989
8330	Excimer Laser Lithography	D.C. Shaver	Electronic Materials Symp., Santa Clara, California, 27 March 1989

\* Author not at Lincoln Laboratory.

**MS No.**

8331	CCD Correlator Applications	S.C. Munroe D.R. Arsenault K.E. Thompson A. Lattes D. Grieco*	Introduction to Spread Spectrum for Communications and Radar, Lexington, Massachusetts, 11-18 March 1989
8342	Recent Research on External-Cavity Semiconductor Diode Array and on Passive Waveguides in GaAs	R.H. Rediker	Seminar, Lockheed Missiles and Space Corporation, Palo Alto, California, 15 March 1989
8347	Capless Rapid Thermal Annealing of Ion Implanted InP	J.D. Woodhouse M.C. Gaidis	Heatpulse Owners Technical Group, Burlington, Massachusetts, 14 March 1989
8362	Multiple Quantum Well Electrooptic Devices	B.F. Aull	Seminar, AT&T Bell Laboratories, Holmdel, New Jersey, 24 March 1989
8362A	Multiple Quantum Well Electrooptic Devices	B.F. Aull	Seminar, Bellcore, Red Bank, New Jersey, 27 March 1989
8362B	Multiple Quantum Well Electrooptic devices	B.F. Aull	EECS/RLE Technical Seminars Series, MIT, 12 April 1989
8367	Several Technologies Applicable to III-V Optoelectronic Integration	W.D. Goodhue	Workshop on III-V Integrated Optoelectronics, Hilton Head, South Carolina, 28 March 1989
8405	The Device Applications and Characterization of Non-stoichiometric GaAs Grown by Molecular Beam Epitaxy	F.W. Smith A.R. Calawa	IEEE Workshop on Instabilities in III-V Devices, Sedona, Arizona, 24 April 1989

---

\* Author not at Lincoln Laboratory.

## ORGANIZATION

### SOLID STATE DIVISION

A.L. McWhorter, *Head*  
I. Melngailis, *Associate Head*  
E. Stern, *Associate Head*  
J.F. Goodwin, *Assistant*

N.L. DeMeo, Jr., *Associate Staff*

### SUBMICROMETER TECHNOLOGY

D.J. Ehrlich, *Leader*  
D.C. Shaver, *Assistant Leader*

Astolfi, D.K.	Kunz, R.R.
Black, J.G.	Lyszcza, T.M.
Dennis, C.L.	Maki, P.A.
Doran, S.P.	Melngailis, J.†
Efremow, N.N., Jr.	Pang, S.W.
Forte, A.R.	Rooks, M.J.
Gajar, S.A.*	Rothschild, M.
Geis, M.W.	Sedlacek, J.H.C.
Goodman, R.B.	Uttaro, R.S.
Hartney, M.A.	Young, K.K.
Horn, M.W.	

### QUANTUM ELECTRONICS

A. Mooradian, *Leader*  
P.L. Kelley, *Associate Leader*  
A. Sanchez-Rubio, *Assistant Leader*

Aggarwal, R.L.	Lacovara, P.
Barch, W.E.	Le, H.Q.
Belanger, L.J.	Menyuk, N.†
Cook, C.C.	Ochoa, J.R.
Daneu, V.	Schulz, P.A.
DeFeo, W.E.	Seppala, J.P.
Fan, T.Y.	Sharfin, W.F.
Hancock, R.C.	Sullivan, D.J.
Henion, S.R.	Tapper, R.S.
Hotaling, T.C.	Wall, K.F.
Jeys, T.H.	Zayhowski, J.J.
Korn, J.A.	

### ELECTRONIC MATERIALS

A.J. Strauss, *Leader*  
B-Y. Tsaur, *Associate Leader*  
H.J. Zeiger, *Senior Staff*

Anderson, C.H., Jr.	Fahey, R.E.	McGilvary, W.L.
Button, M.J.	Finn, M.C.	Nechay, B.A.
Chen, C.K.	Im, J.S.*	Nitishin, P.M.
Choi, H.K.	Iseler, G.W.	Pantano, J.V.
Clark, H.R., Jr.	Kolesar, D.F.	Tracy, D.M.
Connors, M.K.	Krohn, L., Jr.	Turner, G.W.
Delaney, E.J.	Mastromattei, E.L.	Wang, C.A.
Eglash, S.J.	Mattia, J.P.	

---

\* Research Assistant

† Part Time



## APPLIED PHYSICS

R.C. Williamson, *Leader*  
D.L. Spears, *Assistant Leader*  
R.H. Rediker, *Senior Staff*

Aull, B.F.	Lind, T.A.
Bailey, R.J.	Missaggia, L.J.
Betts, G.E.	Mull, D.E.
Bossi, D.E.*	O'Donnell, F.J.
Corcoran, C.J.*	Palmacci, S.T.
Cox, C.H., III	Palmateer, S.C.
Diadiuk, V.	Rauschenbach, K.
Donnelly, J.P.	Reeder, R.E.
Ferrante, G.A.	Roussell, H.V.
Groves, S.H.	Shiple, S.D.*
Harman, T.C.	Tsang, D.Z.
Hovey, D.L.	Walpole, J.N.
Johnson, L.M.	Woodhouse, J.D.
Lau, K.M.§	Yee, A.C.
Liau, Z.L.	

## ANALOG DEVICE TECHNOLOGY

R.W. Ralston, *Leader*  
R.S. Withers, *Associate Leader*  
R.M. Lerner, *Senior Staff*<sup>†</sup>

Anderson, A.C.	Lichtenwalner, D.J.*
Arsenault, D.R.	Lyons, W.G.
Bhushan, M.	Macedo, E.M., Jr.
Boisvert, R.R.	Munroe, S.C.
Brogan, W.T.	Oates, D.E.
Denneno, A.P.	Sage, J.P.
Fitch, G.L.	Seidel, M.N.*
Green, J.B.	Slattery, R.L.
Hamm, J.M.	Thompson, K.E.
Holtham, J.H.	Yu-Jahnes, L-S.*
Lattes, A.L.	

## MICROELECTRONICS

R.A. Murphy, *Leader*  
E.D. Savoye, *Associate Leader*  
B.B. Kosicki, *Assistant Leader*  
R.W. Chick, *Senior Staff*

Actis, R.	Felton, B.J.	McIntosh, K.A.
Bales, J.W.*	Gladden, D.B.†	Mountain, R.W.
Bennett, P.C.	Goodhue, W.D.	Nichols, K.B.
Bozler, C.O.	Gray, R.V.	Parker, C.D.
Brown, E.R.	Gregory, J.A.	Percival, K.A.
Burke, B.E.	Hollis, M.A.	Pichler, H.H.
Calawa, A.R.	Huang, J.C.M.	Rabe, S.
Chen, C.L.	Johnson, B.W.	Rathman, D.D.
Chiang, A.M.	Johnson, K.F.	Reich, R.K.
Chuang, M.L.*	LaFranchise, J.R.	Reinold, J.H., Jr.
Clifton, B.J.	Lincoln, G.A., Jr.	Smith, F.W.*
Daniels, P.J.	Mahoney, L.J.	Sollner, T.C.L.G.
Doherty, C.L., Jr.	Manfra, M.J.	Vera, A.
Dolat, V.S.	Mathews, R.H.	Wilde, R.E.
Durant, G.L.	McGonagle, W.H.	

---

\* Research Assistant

† Part Time

‡ Staff Associate

§ Visiting Staff

# 1. ELECTROOPTICAL DEVICES

## 1.1 THEORETICAL COMPARISON OF LUMPED-ELEMENT AND TRAVELING-WAVE INTEGRATED-OPTIC PHASE MODULATORS

In this report we compare the theoretical performances of lumped-element and traveling-wave integrated-optical phase modulators. Both device configurations are suitable for modulation frequencies up to several gigahertz.<sup>1-3</sup> The analysis shows that optimum modulator response is obtained when the device is impedance-matched to the RF drive source. While this may be difficult to accomplish for broadband applications, it is often possible to achieve efficient impedance-matching for narrowband applications. For LiNbO<sub>3</sub> devices operating at a wavelength of 1.3  $\mu\text{m}$ , the theoretical impedance-matched response of lumped-element modulators exceeds that of traveling-wave modulators if the product of the modulation frequency and electrode length is below 20 GHz-mm.

The lumped-element electrooptic phase modulator is illustrated in Figure 1-1 and consists of an optical waveguide and coplanar electrodes. An equivalent circuit of a phase modulation system containing an electrical source, matching circuit, and modulator is shown in Figure 1-2. The modulator is modeled as a series RC circuit. The voltage across the capacitor corresponds to the electrode voltage. This lumped-element model is limited by electrical transit time considerations to  $fL$  products less than 20 GHz-mm, where  $f$  is the modulation frequency and  $L$  is the electrode length. It is assumed that the electrode voltage and current vary sinusoidally with amplitudes  $V_m$  and  $I_m$ , respectively. The phase modulation amplitude  $\phi_m$  is proportional to the  $V_m L$  product, and the capacitance  $C$  is proportional to  $L$ . Therefore,  $\phi_m$  is proportional to the electrode charge  $Q_m = CV_m$ . The maximum response is obtained when the current  $I_m$  is maximized. This is

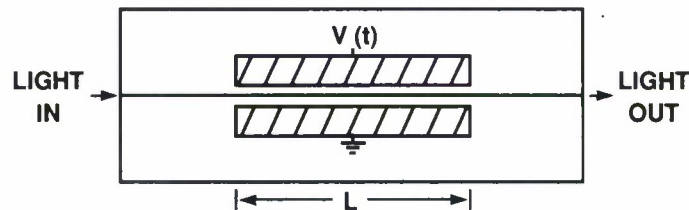


Figure 1-1. Schematic illustration of a lumped-element channel-waveguide electrooptic phase modulator. The phase modulation is proportional to the product of the applied voltage  $V(t)$  and the electrode length  $L$ .

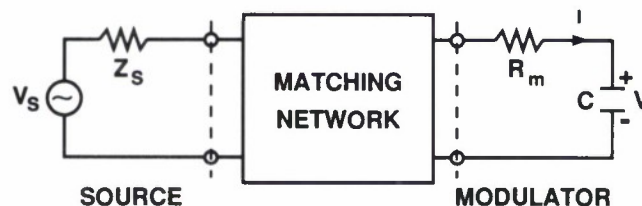


Figure 1-2. Equivalent circuit containing the lumped-element phase modulator, electrical source, and matching circuit.

achieved by impedance matching the source to the modulator and dissipating all of the available power in the series resistance  $R_m$ . A figure of merit,  $K_{LE} \equiv \phi_m^2/P_s$ , where  $P_s$  is the maximum electrical power available from the source, can be written as

$$K_{LE} \equiv \frac{1}{2f^2(C/L)^2 (V_\pi L)^2 R_m}. \quad (1-1)$$

The parameters  $C/L$  and  $V_\pi L$ , where  $V_\pi$  is the voltage change required for a  $\pi$ -radian phase shift, are length independent. Any length dependence of  $R_m$  is ignored in this analysis and is minimized in experimental devices by using multiple electrical feeds along the length of the electrodes. Under this assumption, the impedance-matched modulator response varies inversely with frequency but has no length dependence. For narrowband applications, either baseband or band-pass, it is often possible to achieve efficient matching over the entire modulation bandwidth. A lumped-element interferometric modulator with a transformer impedance match has been demonstrated.<sup>4</sup>

An equivalent circuit of the traveling-wave phase modulator system is shown in Figure 1-3. The traveling-wave electrode impedance is  $Z_m$  and the source impedance is  $Z_s$ . Lossless electrodes are assumed. The maximum modulator response is obtained with the electrode transmission line impedance-matched to the electrical source. In this case all of the available power is dissipated in the electrode termination resistance and the amplitude of the electrode voltage wave is

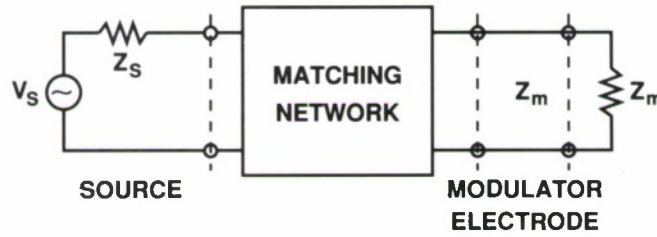


Figure 1-3. Equivalent circuit containing a traveling-wave modulator with electrode impedance  $Z_m$ , matched termination, electrical source, and matching circuit.

maximized. In general, the traveling-wave modulator response depends on both the modulation frequency and electrode length. The figure of merit can be written as

$$K_{TW} \equiv \left. \frac{\phi_m^2}{P_s} \right|_{TW} = \frac{2Z_m}{(V_\pi L)^2 \delta_v^2} \frac{\sin^2(\pi f \delta_v L)}{f^2} \quad (1-2)$$

where  $\delta_v$  accounts for the mismatch between the optical and electrical velocities. For  $\text{LiNbO}_3$  devices,  $\delta_v \approx 2/c$ , where  $c$  is the speed of light. The impedance  $Z_m$  is nearly independent of frequency; therefore, impedance matching should be considerably easier than for the lumped-element device.

The relative performance of impedance-matched lumped-element and traveling-wave modulators as a function of the modulation frequency and electrode length is determined from the ratio

$$\frac{K_{TW}}{K_{LE}} = \frac{4}{\delta_v^2} \left( \frac{C}{L} \right)^2 R_m Z_m \sin^2(\pi f \delta_v L) . \quad (1-3)$$

The responses of the two modulator configurations are equal when  $K_{TW}/K_{LE} = 1$ . This occurs for

$$fL = (fL)_0 = \frac{1}{\pi \delta_v} \sin^{-1} \left[ \frac{\delta_v}{2 \left( \frac{C}{L} \right) \sqrt{R_m Z_m}} \right] . \quad (1-4)$$

For an  $fL$  product less than  $(fL)_0$ , the lumped-element device has higher response than the traveling-wave modulator. Over a range of the  $fL$  product where  $fL$  is greater than  $(fL)_0$ , the traveling-wave design will have better performance. Here,  $\text{LiNbO}_3$  device parameter values  $R_m = 5 \, \Omega$ ,  $C/L = 0.5 \, \text{pF/mm}$ , and  $Z_m = 40 \, \Omega$  will be assumed. For these parameters, the crossover point is  $(fL)_0 \approx 23 \, \text{GHz-mm}$ . This result suggests that for modulation frequencies up to several gigahertz and for all  $fL$  products for which the lumped-element analysis is valid ( $< 20 \, \text{GHz-mm}$ ), the lumped-element response will exceed that which can be obtained with a traveling-wave device. An example of this result is shown in Figure 1-4 where  $K_{LE}$  and  $K_{TW}$  are plotted as a function of  $L$  for 1-GHz modulation. The response of the traveling-wave device exceeds that of the lumped-element device only for electrode lengths longer than 23 mm. Therefore, if impedance-matched operation is obtainable and an electrode length less than 23 mm is desired, a lumped-element device provides the highest response for 1-GHz modulation.

L.M. Johnson

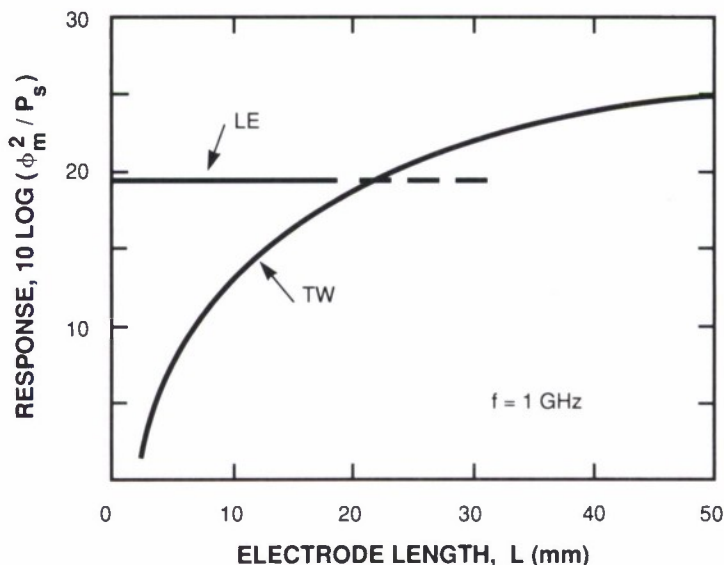


Figure 1-4. Response of a lumped-element (LE) and traveling-wave (TW) modulator as a function of electrode length at a modulation frequency of 1 GHz. Impedance-matched operation is assumed. For  $L > 20 \, \text{mm}$ , approximations employed to calculate lumped-element operation are not valid.



## 1.2 COMPARISON OF THE THERMAL STABILITY OF SEMI-INSULATING InP:Fe AND InP:Ti:Hg

Semi-insulating InP is a very useful substrate material for a variety of high-frequency and high-power electronic and optoelectronic devices. Such devices are fabricated either by direct ion implantation or epitaxial growth of lattice-matched GaInAs, AlInAs or InP, depending on the application. Fe-doped semi-insulating InP has been the substrate material of choice because resistivities in the range of  $10^7$  to  $10^8$   $\Omega$ -cm are routinely achieved. Doping InP with Fe, a deep acceptor located about 0.63 eV below the conduction band,<sup>5</sup> in excess of  $3 \times 10^{16}$   $\text{cm}^{-3}$  introduces a sufficient amount of deep acceptor levels to compensate the residual shallow donors and pin the Fermi level near midgap. It has been reported, however, that severe redistribution of Fe occurs near the surface at temperatures typically encountered during post-implant annealing and epitaxial growth.<sup>6,7</sup> In either case, upon heating, this so-called thermal instability results in an accumulation of Fe within 1000 Å of the surface, below which is a relatively deep ( $\sim 1$   $\mu\text{m}$ ) region substantially depleted of Fe. The deep Fe depletion region is believed to be the cause of surface type conversion (i.e., an n-type surface layer forms in InP:Fe substrates during heat treatment). In addition, since background Fe content has been shown to critically affect the activation efficiency of low-dose Si implants,<sup>8</sup> any surface redistribution of Fe should therefore adversely affect the formation of n-type channel regions typically employed in InP FETs. Although wafer qualification and strict control of process temperature cycles can minimize deleterious effects due to Fe redistribution, a thermally stable semi-insulating InP substrate would permit greater process latitude and be less prone to electrical variations across a wafer. Recently, it has been shown that semi-insulating InP can be grown by co-doping the melt with Ti, a deep donor, and a suitable shallow acceptor such as Zn, Cd, Be or Hg.<sup>9</sup> Resistivities in the range of 1 to  $3.3 \times 10^6$   $\Omega$ -cm have been achieved using this technique. Brandt<sup>10</sup> proposed that semi-insulating substrates prepared by Ti doping should exhibit improved thermal stability because Ti should have a much lower diffusivity in InP than Fe. This reasoning is based on the known diffusivity trend for the 3d transition elements in GaAs.<sup>10</sup> In this report we directly compare the redistribution of Fe with that of Ti and Hg in their respective semi-insulating substrates under identical annealing conditions.

InP:Fe ( $[\text{Fe}] = 6 \times 10^{16}$   $\text{cm}^{-3}$ ) and InP:Ti:Hg ( $[\text{Ti}] = 10^{16}$   $\text{cm}^{-3}$ ,  $[\text{Hg}] = 10^{16}$   $\text{cm}^{-3}$ ) crystals with residual donor concentrations of about  $5 \times 10^{15}$   $\text{cm}^{-3}$  were cut into (100)-oriented wafers. The wafers were subsequently polished and free etched using 3 percent and 0.5 percent Br-methanol solutions, respectively. Slices from each type of wafer were cut into several samples. Some were used as control pieces and others were coated with 1000 Å of plasma-deposited  $\text{Si}_3\text{N}_4$  and annealed at 800°C for 30 min in a graphite strip heater system under a dilute  $\text{PH}_3$  (0.2 percent in  $\text{N}_2$ ) atmosphere. Following annealing, the  $\text{Si}_3\text{N}_4$  encapsulant was stripped in a 50/50  $\text{HF}/\text{H}_2\text{O}$  solution and the atomic concentrations of the dopants were determined as a function of depth from the surface by SIMS analysis. The results are shown in Figures 1-5 and 1-6. Figure 1-5(a) shows that the substrate Fe concentration for an unannealed InP:Fe sample is very uniform to a depth of about 2.5  $\mu\text{m}$  into the wafer. Upon annealing at 800°C, however, Figure 1-5(b) clearly shows a deep ( $\sim 5000$  Å) Fe depletion zone similar to that reported in the

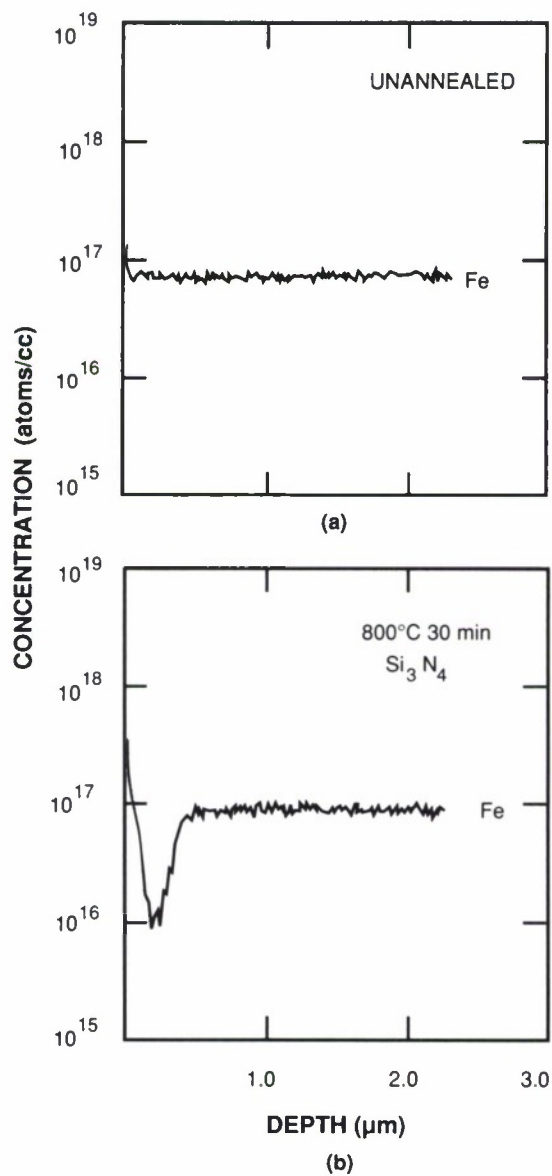


Figure 1-5. SIMS profiles of Fe in semi-insulating InP:Fe for (a) an annealed substrate and (b) a substrate annealed at 800°C for 30 min with a  $\text{Si}_3\text{N}_4$  encapsulant.

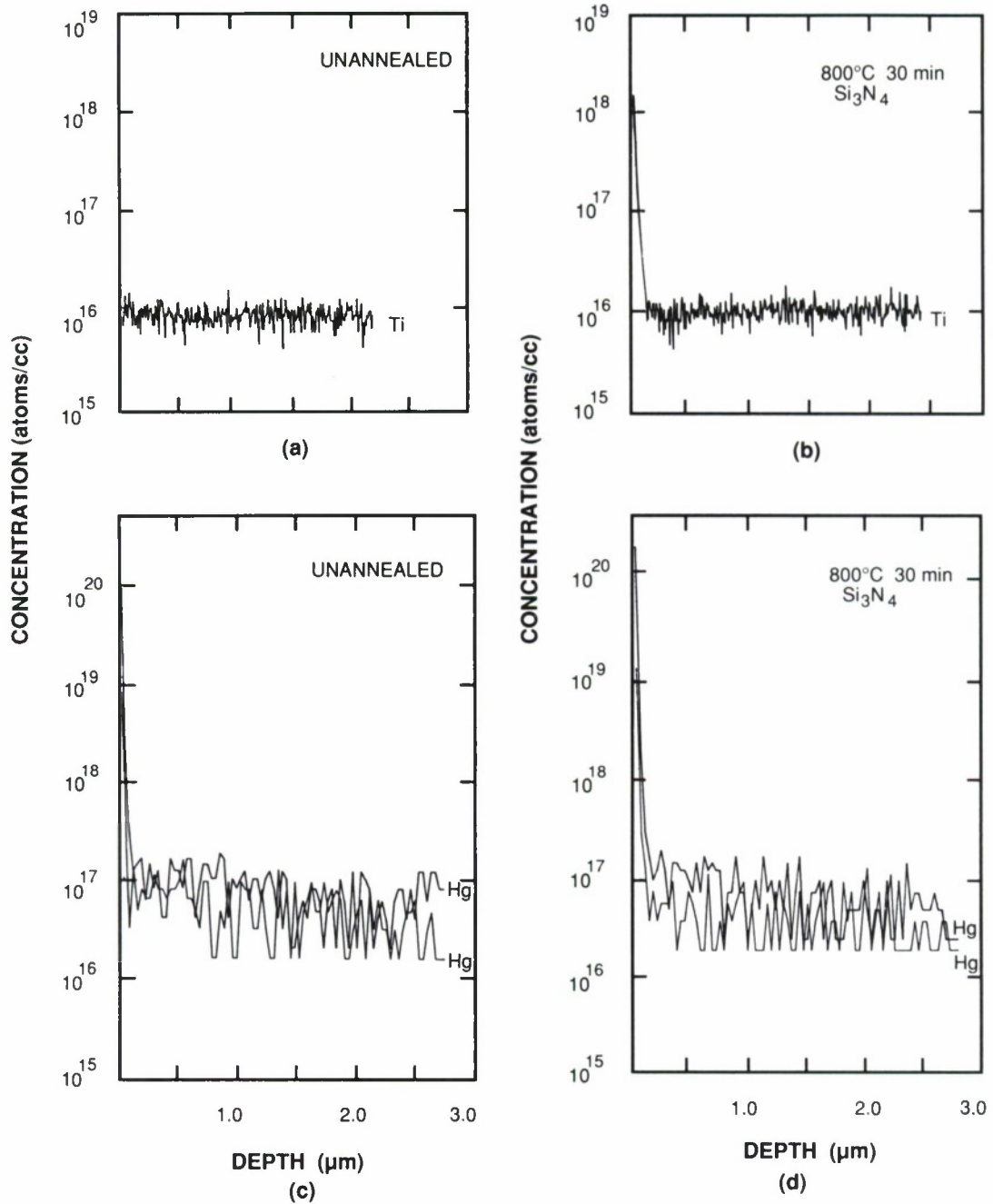


Figure 1-6. SIMS profiles of Ti and Hg in semi-insulating InP:Ti:Hg for (a) and (c), an unannealed substrate, and (b) and (d), a substrate annealed at 800°C for 30 min with a  $\text{Si}_3\text{N}_4$  encapsulant.

literature.<sup>6,7</sup> We do not, however, observe the expected Fe accumulation region at the surface but can only surmise that for this temperature and time, most of the Fe diffused out through the surface and into the  $\text{Si}_3\text{N}_4$  layer. In contrast, Figure 1-6 shows before and after annealing characteristics of the Ti and Hg atomic concentrations in InP:Ti:Hg wafers. It is readily apparent that, except for a slight increase in the near-surface concentrations, there is virtually no change in either the Ti or Hg doping level during high-temperature annealing. These measurements confirm Brandt's<sup>10</sup> proposal that the diffusivity of Ti in InP would be much lower than that of Fe.

Preliminary results on the electrical activation of low-dose ( $6 \times 10^{12} \text{ cm}^{-2}$ ) 400-keV  $\text{Si}^+$  implants performed at room temperature are illustrated in Figure 1-7. These samples were annealed in a tungsten-halogen-lamp rapid-thermal-annealing (RTA) system using a capless enhanced-overpressure proximity (EOP)<sup>11</sup> technique at temperatures between 800 and 900°C for 10 s. The sheet-carrier concentration  $N_s$  and sheet mobility  $\mu_s$  were obtained on specially prepared samples by Hall-effect measurements. For Fe-doped InP, both  $N_s$  and  $\mu_s$  degrade dramatically as the annealing temperature is increased. Possible explanations for this behavior include

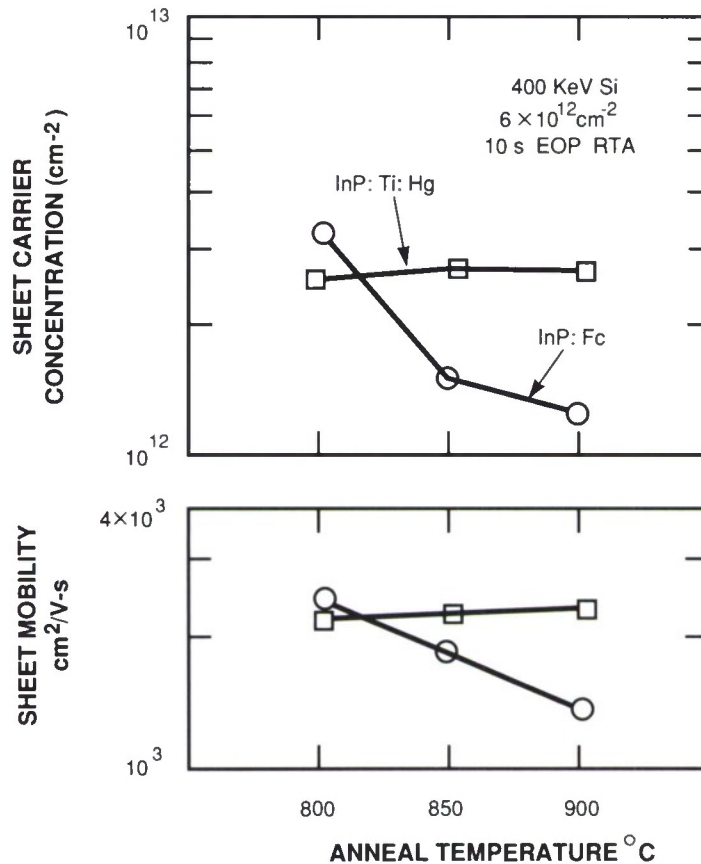


Figure 1-7. Sheet-carrier concentration and mobility vs EOP-RTA anneal temperature for InP:Fe and InP:Ti:Hg samples implanted with  $6 \times 10^{12} \text{ cm}^{-2}$  of 400-keV  $\text{Si}^+$  at room temperature.



the formation of compensating defects due to preferential phosphorus evaporation<sup>12</sup> or surface accumulation of compensating Fe acceptors. In InP:Ti:Hg, however, both  $N_s$  ( $2.5 \times 10^{12} \text{ cm}^{-2}$ ) and  $\mu_s$  ( $2200 \text{ cm}^2/\text{V-s}$ ) remain relatively constant with increasing annealing temperature. This type of behavior is normally expected in good quality substrates.

Although our SIMS measurements did not indicate the formation of an Fe surface accumulation layer for 30-min annealing, it is most probable that a significant amount of Fe remains at the surface after rapid thermal annealing because the Fe does not have time to completely diffuse out through the surface. Also, since all samples were annealed under identical conditions, phosphorus loss alone cannot account for the large discrepancy between the InP:Fe and InP:Ti:Hg electrical data. It is therefore believed that the decrease of  $N_s$  and  $\mu_s$  for Fe-doped substrates is caused by compensation due to the migration of Fe acceptors to the surface during rapid thermal annealing. Conversely, the relative electrical stability of  $N_s$  and  $\mu_s$  observed in InP:Ti:Hg is a direct result of the atomic thermal stability of Ti and Hg. Additional SIMS study and Hall measurements are required to accurately assess the atomic dopant profiles and electrical activation of various doses of  $\text{Si}^+$ -implanted InP:Fe and InP:Ti:Hg substrates which are annealed under capped or capless RTA conditions.

In summary, we have demonstrated that Ti redistribution in semi-insulating InP is significantly less than that of Fe under identical annealing conditions. Additionally, it is proposed that the atomic thermal stability of Ti and Hg is directly responsible for the improved electrical activation of low-dose  $\text{Si}^+$ -implanted InP:Ti:Hg under RTA conditions.

J.D. Woodhouse  
G.W. Iseler  
J.P. Donnelly

### 1.3 WAFER FUSION BY MASS TRANSPORT: A NEW TECHNIQUE FOR MONOLITHIC INTEGRATION

We report promising initial results of an experiment in which mass transport was used to fuse together two InP wafers. This technique can potentially open up entirely new ways for monolithic integration and make possible a new array of optoelectronic devices.

Fusion of compound semiconductor crystals by mass transport was previously observed in buried-heterostructure laser fabrication, in which totally undercut mesas were fused back onto the substrate.<sup>13,14</sup> However, to realize fusion of the entire wafer, very close contact must be maintained between the two mating surfaces over the entire wafer dimension. This is because mass transport relies on surface energy as the driving force and the gap to be filled must be very small for complete fusion to occur at reasonable temperatures and time periods.<sup>13,15</sup> In the present work, a technique has been developed to achieve such close contact. Two InP wafers were fused face-to-face across the entire 9-mm wafer width.

A reactor has been designed which can press the wafers together at elevated temperatures. As illustrated in the transverse cross-sectional view in Figure 1-8, the reactor consists of a graphite container assembly which fits inside a cylindrical quartz container. Thus, when the reactor is

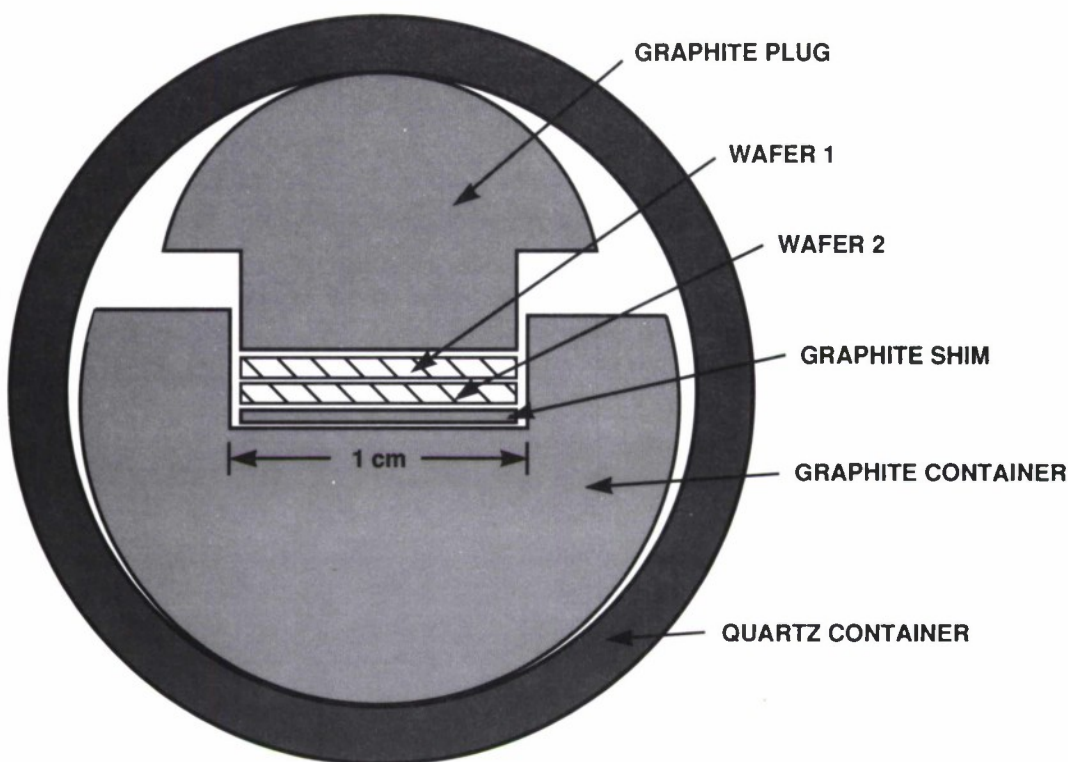
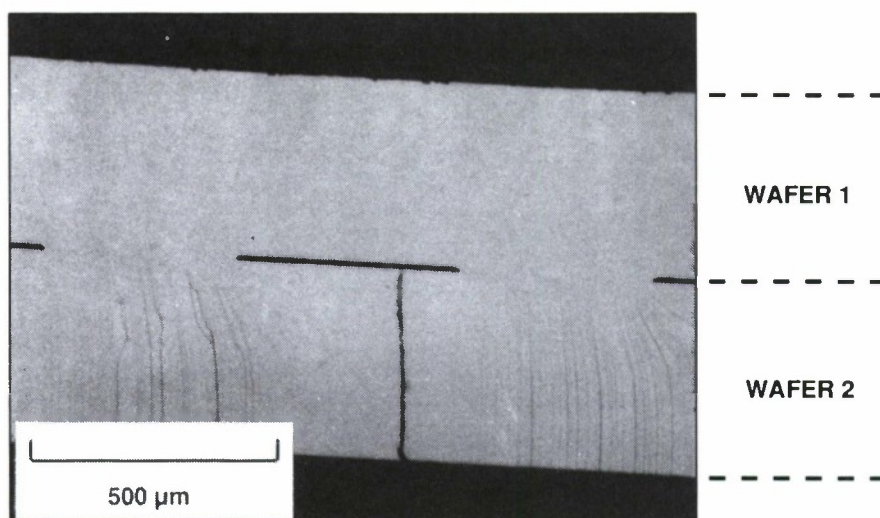


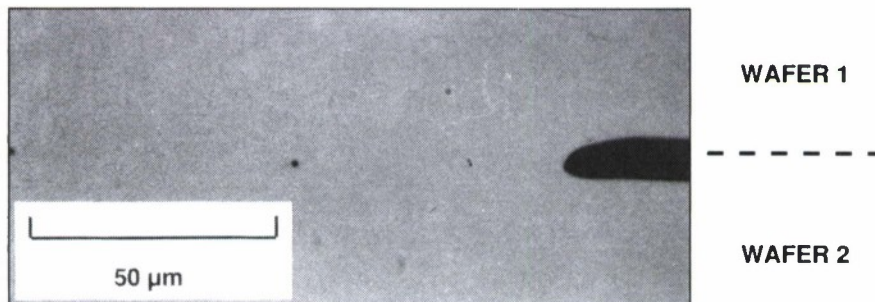
Figure 1-8. Schematic drawing of the transverse cross-sectional view of the wafer-fusion reactor. The actual device has an overall diameter of 2.5 cm and a length (in the direction perpendicular to the page) of 4 cm.

heated to a high temperature, it can result in a strong compression for the wafer pair inside due to the differential thermal expansion of quartz and graphite, whose linear thermal expansion coefficients are  $0.5 \times 10^{-6}$  and  $9 \times 10^{-6} \text{ K}^{-1}$ , respectively.<sup>16</sup> Since the semiconductor wafers become more flexible at elevated temperatures, the compression further forces the two surfaces to conform to each other and produces a very close contact, even if these surfaces were originally slightly curved.

In each experiment, two polished InP wafers of (100) orientation were nearly perfectly cleaved to closely fit the  $9 \times 15$ -mm slot in the graphite container and to enable precise crystallographic alignment. The wafer pair were then test loaded in the graphite container to precisely determine the thickness of the graphite shim in order that the entire assembly could closely fit in the quartz container. The reactor was subsequently baked without the wafers at approximately  $850^\circ\text{C}$  in a purified  $\text{H}_2$  flow. Meanwhile, mesa stripes of approximately  $500\text{-}\mu\text{m}$  width on  $1016\text{-}\mu\text{m}$  centers were etched in one of the two wafers for use as markers. The wafers were then thoroughly cleaned, lightly etched and loaded into the baked reactor with the polished surfaces facing each other. The graphite container was tilted so that the good cleaved edges were gravitationally pulled against the graphite sidewall. After an initial  $\text{N}_2$  and  $\text{H}_2$  purging, mass transport was carried out in a  $\text{PH}_3$  (5 percent) and  $\text{H}_2$  flow at approximately  $850^\circ\text{C}$  for 18 h (overnight).



(a)



(b)

*Figure 1-9. Optical micrographs showing (a) the cleaved cross section of the fused wafer and (b) the magnified view of a fused region. In (a), the long cavities between the fused regions are etched regions in one of the original wafers. In the fused region in (b), two small cavities can be seen (near center and left edge of the photograph).*



After mass transport, the two wafers were fused together and could be cleaved just like one single wafer. Examination of the cleaved cross section using optical and scanning electron microscopes showed fusion across the entire 9-mm wafer width except for the etched regions, as shown in Figure 1-9(a). In the fused regions, no signs of the original interface could be seen, except for some occasional cavities which are approximately spherical with diameters less than  $2\text{ }\mu\text{m}$  and roughly  $50\text{ }\mu\text{m}$  apart [Figure 1-9(b)]. These cavities are probably due to roughness or waviness in the original wafer surfaces and can probably be reduced by using better polished wafers.

A relatively high temperature was used in this initial experiment for an easy observation of the phenomenon. With a good compression mechanism to maintain a very close contact between wafers, fusion can likely be achieved at considerably lower temperatures. In addition, by using a similar reactor design, wafers can probably be fused side by side, along the cleaved facets. More work is needed to refine the fusion techniques and to evaluate the fused wafers.

Z.L. Liao

D.E. Mull

## 1.4 MASS TRANSPORT OF GaInP

We report experiments on the mass transport of  $\text{Ga}_{0.5}\text{In}_{0.5}\text{P}$  lattice matched to GaAs. The successful mass transport of the material reported here has significance for two reasons. First, a route is now open for the application of the mass-transport fabrication technology to GaAs-based devices. The mass transport of InP has led to the development of InGaAsP/InP buried-heterostructure (BH) lasers and surface-emitting laser arrays.<sup>17</sup> Also, microlens arrays of InP and GaP have been fabricated using mass transport of these compounds.<sup>18</sup> Application of this technology to AlGaAs/GaAs has not been achieved because of the reactivity of AlGaAs alloys. Second, this represents the first use of *alloy* semiconductor mass transport as a fabrication tool. It demonstrates that the ratio of column III elements in the alloy can be preserved during the transport, a process which has been explained by surface diffusion of indium and gallium.<sup>19</sup>

A preliminary experiment was first performed on GaInP mesas. A  $3\text{-}\mu\text{m}$ -thick layer of GaInP was grown by liquid phase epitaxy (LPE) on a (001)-oriented GaAs substrate at  $750^\circ\text{C}$ . Mesa stripes  $2\text{ }\mu\text{m}$  high and  $6\text{ }\mu\text{m}$  wide were etched into the GaInP layer. After a heat treatment of 5 h at  $780^\circ\text{C}$  in a  $\text{H}_2/\text{PH}_3$  ambient, it was observed that the sharp mesa edges had rounded and there was considerable smoothing of the chemically etched valleys between mesas. The smooth morphology of the mass-transported material was a strong indication that the alloy composition, lattice matched to GaAs, had been maintained.

Next, an undoped double heterostructure (DH) of GaInP/GaAs/GaInP was grown by organometallic vapor phase epitaxy (OMVPE) at  $650^\circ\text{C}$  on a GaAs substrate, oriented  $2^\circ$  off (001) toward [011]. The GaAs layer and GaInP layers were  $0.1\text{ }\mu\text{m}$  and  $0.8$  to  $0.9\text{ }\mu\text{m}$  thick, respectively. Mesa stripes  $5.5\text{ }\mu\text{m}$  wide were etched to the lower GaInP layer, and then the mesa was partially undercut by selective etching of the GaAs to a  $1.0\text{-}\mu\text{m}$  width. This procedure is similar to that used for InGaAsP/InP BH structures.<sup>20</sup> Mass transport was carried out at  $747^\circ\text{C}$  for 3 h. A cleaved cross section of a BH mesa from this experiment is shown in Figure 1-10. It is clear that the GaInP has transported to partially fill the undercut mesa and has enclosed the GaAs.

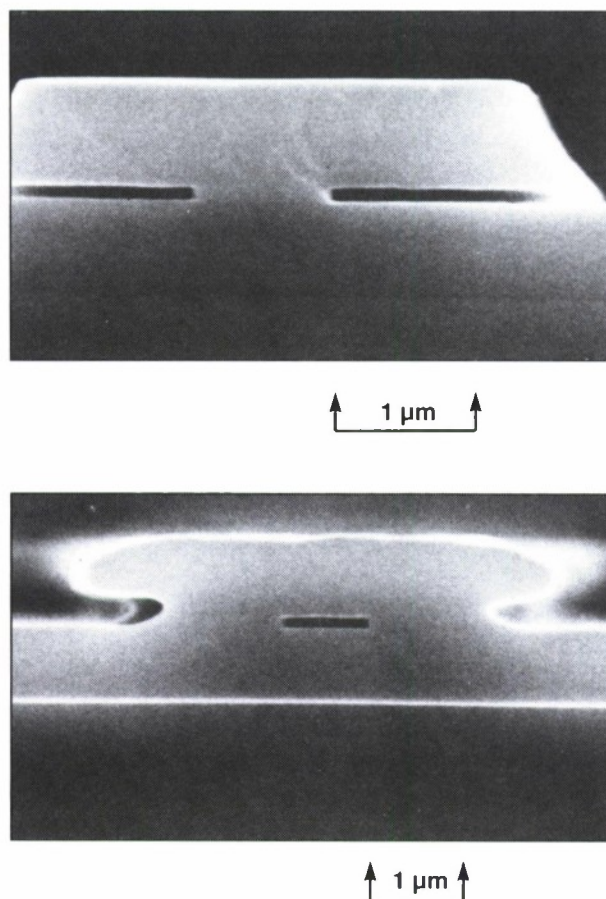


Figure 1-10. Scanning electron micrographs of cleaved GaInP/GaAs DH structure with etched mesas before (top) and after (bottom) mass transport. There is a slight magnification difference between the two pictures.

For the final experiment, a heterostructure was used which differed from that above in two respects. First, the structure had the heavy doping of a typical laser structure, and second, a p-type GaAs contact layer, with an associated GaInP cover, was added. On an n-type GaAs substrate, off orientation as above, in order, a 1- $\mu\text{m}$ -thick n-type GaInP cladding layer, a 0.1- $\mu\text{m}$ -thick undoped GaAs layer, a 1- $\mu\text{m}$ -thick p-type GaInP cladding layer, a 0.2- $\mu\text{m}$ -thick p-type GaAs contacting layer, and a 0.3- $\mu\text{m}$  thick p-type GaInP cap layer were grown by OMVPE. Silicon and Zn were used as dopants in the epilayers and the substrate at concentrations of approximately  $1 \times 10^{18}$  atoms/cm<sup>3</sup>. Two mass-transport steps were used with this structure. First, the contacting GaAs was buried in stripe form, and second, the GaAs active layer was buried as in the earlier experiment. From past experience with exposed InGaAsP layers during InP mass transport, it was expected that an exposed GaAs contact layer would seriously complicate the



surface chemistry and transport. By covering the contact layer this was prevented, and after the second mass-transport step, selective etching was used to expose the GaAs for metallization. The success of this experiment demonstrates the feasibility of applying the mass-transport fabrication technique to GaInP/GaAs lasers.

From studies of the mass-transport phenomenon,<sup>19</sup> it is believed that transport of GaInP involves the dissociation and diffusion of Ga and In. Since rates for these processes are likely to be quite different for each type of atom, it is at first surprising that the ternary alloy can transport and still maintain its stoichiometry. However, because relatively small numbers of free atoms ( $\ll 1$  monolayer) are involved in the process, their populations are easily altered by a slight deviation of the composition of the regrown material from that of the eroded material. This readily offsets the differences in diffusion and dissociation rates and maintains the stoichiometry. However, if the alloy contains more than one column V element, it is unlikely to maintain stoichiometry unless the vapor pressures of these elements can be maintained at the needed ratio.

In conclusion, it is worth noting that if the mass-transport fabrication capabilities, well demonstrated for InP-based lasers, are applied to existing GaInP/GaAs technology, significant improvements in performance of GaAs lasers are expected. For example, with reported threshold current densities<sup>21</sup> and the 1- to 2- $\mu\text{m}$  stripe width capability of mass-transport fabrication, threshold currents less than 100  $\mu\text{A}$  should be possible, which would be a  $5\times$  reduction over existing AlGaAs/GaAs technology. Such diodes would have reduced capacitance with projected modulation frequencies in excess of 25 GHz, more than a  $2\times$  improvement over existing AlGaAs/GaAs laser diodes. Furthermore, GaInP mass transport may also be applicable to short-wavelength (visible) lasers based on the GaInAsP/GaAs system.

S.H. Groves  
Z.L. Liao  
S.C. Palmateer

## 1.5 EXTERNAL CAVITY OPERATION OF InGaAsP DIODE LASER ARRAYS

Interest in coherently combining the output of individual elements of diode laser arrays has been high in recent years because of the potential for producing narrow, high-power beams. Several successful efforts in AlGaAs/GaAs lasers have been reported using both diffraction coupling and external cavity schemes.<sup>22-25</sup> However, in the longer-wavelength InGaAsP/InP system, only on-chip coupling schemes have resulted in coherent operation.<sup>26</sup> Here, we report the first observation of coherent phase locking of an InGaAsP laser array using an external cavity.

The experimental device was a monolithic five-element linear array of edge-emitting, buried-heterostructure InGaAsP lasers fabricated by mass transport.<sup>27</sup> Because the entire array was driven in parallel from a single source (CW or pulsed), the array was chosen on the basis of uniformity of the threshold current values of its elements. (The uniformity requirement might be relaxed if individual contacts to each laser were used.) One facet of the laser chip was antireflection (AR) coated with thermally evaporated SiO (thickness = 1800 Å, refractive index = 1.8) to

eliminate lasing. An array of InP microlenses also fabricated by mass transport was used to collimate the output of the diode lasers. Figure 1-11 shows a photograph of the lenslets and an example of their image-forming capability. Earlier evaluation of similar lenslets using a single diode laser as a point source yielded nearly diffraction-limited performance.<sup>28</sup> The microlens spacing was  $127\text{ }\mu\text{m}$ , designed to match the laser array center-to-center spacing; the diameter of the lenslets was also  $127\text{ }\mu\text{m}$  and the focal length was  $130\text{ }\mu\text{m}$ , yielding  $\sim f/1$ . Because of the small focal spot and depth of focus of these  $f/1$  lenslets, alignment between the laser and microlens arrays required accuracy on the order of a few microns. It was accomplished using a fine-control alignment stage that incorporates mechanical and piezoelectric (PZT) manipulators to achieve the three translational and three angular degrees of freedom required to align two points on two planes. This entire assembly was mounted on PZT gimbals and translation stages that allowed the assembly to be aligned to the optical axis of the external cavity.

#### MASS TRANSPORTED $f/1$ LENSLET ARRAY

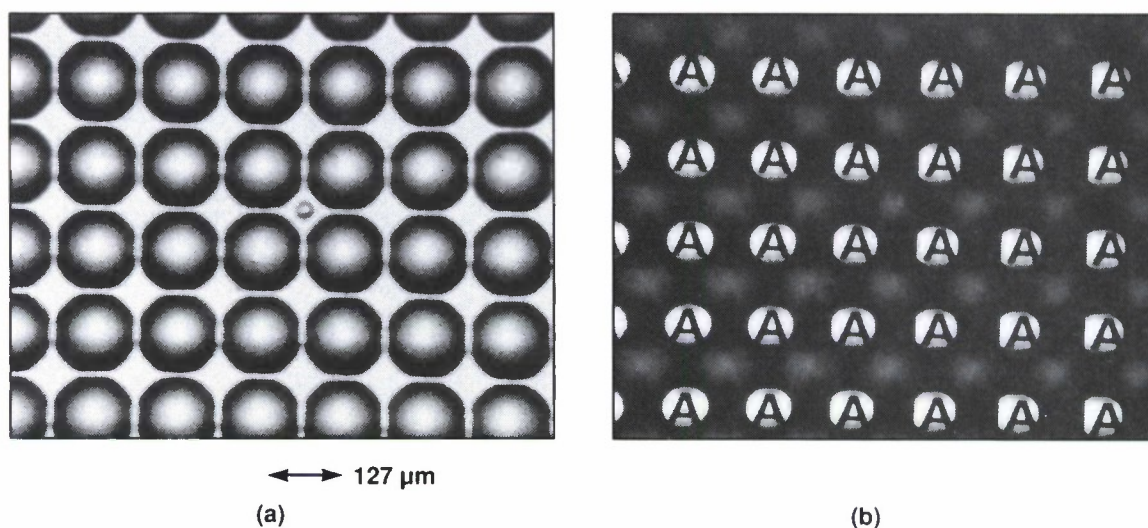


Figure 1-11. (a) Optical micrograph of mass-transported two-dimensional microlens array. (b) Images formed by the microlenses.

A schematic block diagram of the elements in the external cavity, as well as the diagnostic optics, is shown in Figure 1-12. Initial alignment of the cavity elements was carried out by means of an external He-Ne laser and pinholes placed in front of the cavity objectives and mirror. Reflection of the He-Ne beam from the laser chip facet, which was made coincident with the incoming beam by proper positioning of the laser-lenslet assembly, was then used to align the external optics and spectrometer. A near-field image of the collimated laser array was used to obtain coarse alignment with the lenslets, while recovery of the original lasing threshold current

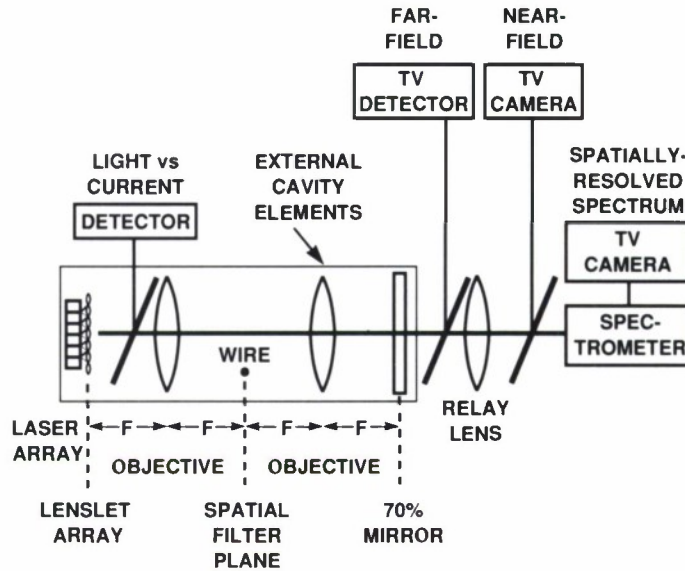


Figure 1-12. Schematic of external-cavity elements and diagnostic optics.

by adjustment of the location and angle of the external mirror also indicated that fine alignment of laser and lenslet arrays had been obtained.

To monitor the operation of the lasers in the external cavity, a portion of the main beam was split off, away from the optical axis, and sampled with a detector. With this setup, the effect on the array output of blocking the external mirror could be observed. Figure 1-13 shows the light vs current (LI) characteristics with the external mirror blocked and unblocked. This measurement indicates that at least one element is operating above laser threshold due to feedback

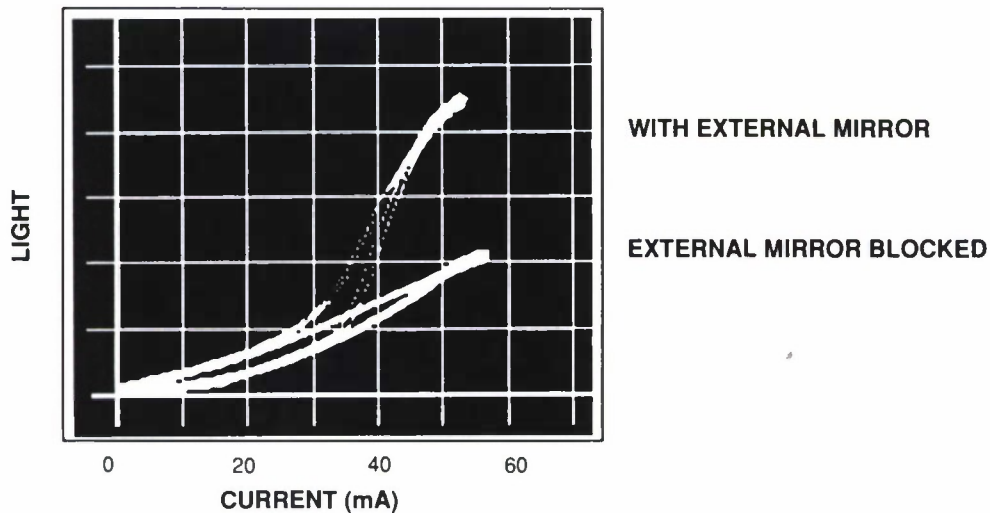


Figure 1-13. Light-current characteristics of laser array with and without feedback from the external mirror.



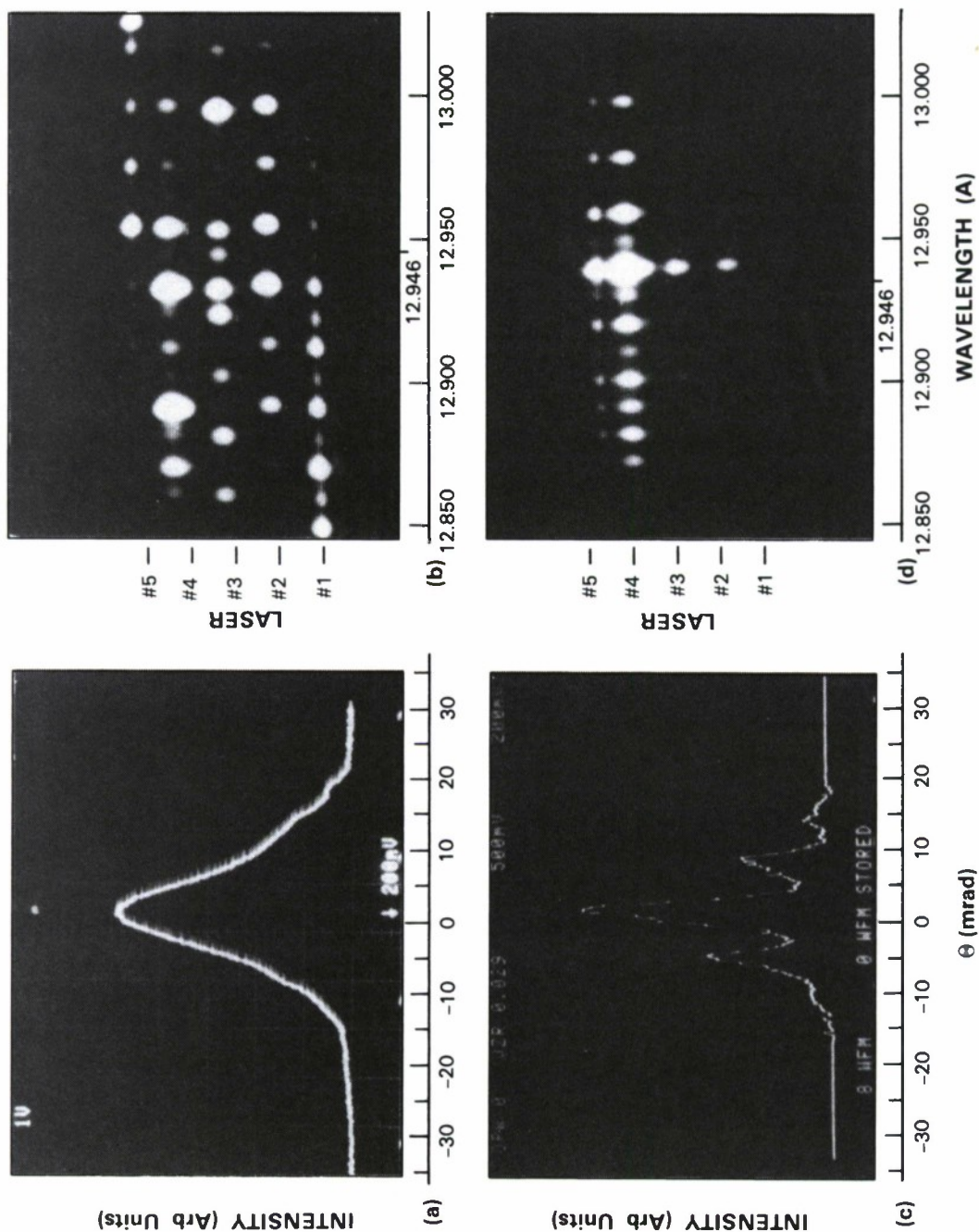


Figure 1-14. Far-field patterns (a) and (c) and spatially resolved spectra (b) and (d) of the external cavity output. (a) and (b) incoherent operation, (c) and (d) coherent operation of four elements with spatial filter in cavity.



from the external mirror. It is necessary to observe the near-field image to determine which devices are actually lasing. By optimizing the external mirror and lenslet alignments, all the elements in the array could be made to exhibit external-cavity operation.

The far-field pattern and spatially resolved spectrum of the output beam with the cavity in this configuration is shown in Figures 1-14(a) and 1-14(b). The width of the peak in the far-field pattern is 13 mrad and corresponds to a 122- $\mu\text{m}$  aperture, which is close to the effective diameter of a single lenslet. This width and the different mode patterns evident in the spectrum indicate that the devices are lasing independently from each other. It is also clear from the spectrum that four of the five devices have similar sets of modes, while the fifth element is quite different. This is consistent with the near-field image which shows a weaker output from the fifth device. Coherent operation can be achieved by inserting a spatial filter in the middle of the two cavity objectives. A suitable spatial filter is one that allows the energy in the central lobe to pass through and be reflected by the external mirror while blocking light that will not contribute to that mode. In this case, a single vertical wire, placed between the two cavity objectives but displaced from the optical axis of the cavity, was used. Its effect on the far-field pattern and spatially resolved spectrum is shown in Figures 1-14(c) and 1-14(d). The far-field pattern now exhibits clearly defined lobes, the width of which is 3.2 mrad and corresponds to an aperture of 490  $\mu\text{m}$ , which is equivalent to  $\sim 4$  devices. It can be seen that the single-element far-field pattern [Figure 1-14(a)] is the envelope function of the multilobed pattern [Figure 1-14(c)]. Since the fill-factor of the lenslet array is less than 100 percent, the presence of more than one lobe is to be expected. In fact, by calculating the effective lens area of the lenslet wafer, including the less-than-ideal edges of the lenslets, a 71 percent fill-factor is obtained. This is in moderately good agreement with the value of 65 percent obtained from measuring the area under the central lobe in the far-field pattern. The energy in the sidelobes can be incorporated into the main lobe by demonstrated binary-optics techniques.<sup>29</sup> With the spatial filter in place, the spatially resolved spectrum shows only one predominant mode for the four lasers. The dim modes still present, especially in the spectrum of the strongest element, are below threshold. These results indicate that the four lasers are phase-locked and operating coherently in the external cavity. As expected, both the far-field pattern and spatially resolved spectrum are very sensitive to the position of the wire; better depth of modulation in the far-field and a single-mode spectrum might be obtained by using a slit rather than a wire as the spatial filter.

In summary, coherent operation of an InGaAsP laser array operating at  $\lambda = 1.3 \mu\text{m}$  has been observed for the first time using a collimating InP lenslet array and a spatial filter in an external cavity. A multilobed, but narrow, far-field pattern corresponding to four locked elements was obtained. The central peak contained 65 percent of the energy, in agreement with the fill-factor of the mass-transported lenslet array. These results also demonstrate the high optical quality of the refractive InP microlens arrays. Work is under way to optimize the spatial filter and uniformity of the laser threshold currents, as well as to extend this technique to monolithic two-dimensional laser arrays to take advantage of the two-dimensional microlens arrays.

V. Diadiuk

J.W. Caunt

Z.L. Liao

R.C. Williamson

J.N. Walpole

## REFERENCES

1. R.A. Becker, IEEE J. Quantum Electron. **QE-20**, 723 (1984).
2. C.M. Gee, G.D. Thurmond, and H.W. Yen, Appl. Phys. Lett. **43**, 998 (1983).
3. R.A. Becker, Appl. Phys. Lett. **45**, 1168 (1984).
4. Solid State Research Report, Lincoln Laboratory, MIT, 1989:1, p. 1.
5. G.W. Iseler, Inst. Phys. Conf. Ser. No. 45, Chap. 2, p. 144 (1979).
6. J.D. Oberstar, B.G. Streetman, J.E. Baker, and P. Williams, J. Electrochem. Soc. **128**, 1814 (1981).
7. H. Kamada, S. Shinoyama, and A. Katsui, J. Appl. Phys. **55**, 2881 (1984).
8. B. Molnar, P.G. Siebenmann, W.D. Wilsey, H.B. Dietrich, and J.D. Oberstar, Naval Research Laboratory, Washington, D.C. (unpublished paper, 1984).
9. G.W. Iseler and B.S. Ahern, Appl. Phys. Lett. **48**, 1656 (1986).
10. C.D. Brandt, Ph.D. thesis, MIT, 1987.
11. J.D. Woodhouse, M.C. Gaidis, J.P. Donnelly, and C.A. Armiento, Appl. Phys. Lett. **51**, 186 (1987).
12. C.W. Farley and B.G. Streetman, J. Electrochem. Soc. **134**, 498 (1987).
13. Z.L. Liao, J.N. Walpole, and D.Z. Tsang, IEEE J. Quantum Electron. **QE-20**, 855 (1984).
14. B. Broberg, S. Koentjoro, K. Furuya, and Y. Suematsu, Appl. Phys. Lett. **47**, 4 (1985).
15. Solid State Research Report, Lincoln Laboratory, MIT, 1988:4, p. 4, DTIC AD-A209969.
16. *American Institute of Physics Handbook*, 3rd edition, D.E. Gray, Ed. (McGraw-Hill, New York, 1972), Section 4.
17. Z.L. Liao and J.N. Walpole, Appl. Phys. Lett. **50**, 528 (1987).
18. Z.L. Liao, V. Diadiuk, J.N. Walpole, and D.E. Mull, Appl. Phys. Lett. **52**, 1859 (1988).
19. Solid State Research Report, Lincoln Laboratory, MIT, 1988:4, p. 4, DTIC AD-A209969.
20. Z.L. Liao, J.N. Walpole, and D.Z. Tsang, IEEE J. Quantum Electron. **QE20**, 855 (1984).

21. Zh. I. Alferov , N.Yu. Antonishkis, I.N. Arsent'ev, D.Z. Garbuzov, V.I. Kolyshkin, T.A. Nalet, N.A. Strugov, and A.V. Tikunov, *Sov. Phys. Semicond.* **22**, 650 (1988).
22. J.R. Leger, M.L. Scott, and W.B. Veldkamp, *Appl. Phys. Lett.* **52**, 1771 (1988).
23. S. Wang, J.C. Wilcox, M. Jansen, and J.J. Yang, *Appl. Phys. Lett.* **48**, 1770 (1986).
24. J.Z. Wilcox, W.W. Simmons, D. Botez, M. Jansen, L.J. Mawst, G. Peterson, T.J. Wilcox, and J.J. Yang, *Appl. Phys. Lett.* **54**, 1848 (1989).
25. F.X. D'Amato, E.T. Siebert, and C. Roychoudhuri in *Proceedings CLEO '89*, Baltimore, Md., 24-28 April 1989, paper FL-3.
26. D. Yap, J.N. Walpole, and Z.L. Liao, *Appl. Phys. Lett.* **54**, 687 (1989).
27. Z.L. Liao and J.N. Walpole, *Appl. Phys. Lett.* **46**, 115 (1985).
28. Z.L. Liao, V. Diadiuk, J.N. Walpole, and D.E. Mull, *Appl. Phys. Lett.* **52**, 1859 (1988).
29. J.R. Leger, G.J. Swanson, and M. Holz, *Appl. Phys. Lett.* **50**, 1044 (1987).

## 2. QUANTUM ELECTRONICS

### 2.1 GAIN-SWITCHED PULSED OPERATION OF MICROCHIP LASERS

Microchip lasers are small solid state lasers with typical cavity lengths of less than 1 mm.<sup>1,2</sup> The small cavity lengths lead to very short cavity lifetimes, even for cavities with high-reflectivity mirrors. As a result, microchip lasers are capable of shorter pulse operation than is possible with larger-cavity-length solid state lasers.

Gain-switched pulses have been obtained from three different microchip lasers. Two of the microchip lasers were constructed from Nd:YAG ( $\text{Nd}_x\text{Y}_{3-x}\text{Al}_5\text{O}_{12}$ ), cut and polished to a thickness of 750  $\mu\text{m}$ . One had a 0.3 percent output coupler; the other had a 1.3 percent output coupler. The opposite mirror of both lasers had a reflectivity of 99.9 percent at 1.064  $\mu\text{m}$ , and transmitted the pump. The third gain-switched microchip laser used LNP ( $\text{LiNdP}_4\text{O}_{12}$ ) and had a 140- $\mu\text{m}$  cavity length and a 1.3 percent output coupler. Again, the other mirror had a reflectivity of 99.9 percent at the lasing wavelength (1.048  $\mu\text{m}$ ) and transmitted the pump.

The microchip lasers were pumped with a pulsed Ti:Al<sub>2</sub>O<sub>3</sub> laser. The output of the Ti:Al<sub>2</sub>O<sub>3</sub> laser was a train of 40-ns pulses at a 5-kHz repetition rate, with a time-averaged power of 180 mW. When the Ti:Al<sub>2</sub>O<sub>3</sub> laser was tightly focused onto the microchip lasers, the microchip lasers produced a train of short pulses. The pump was then defocused until each pump pulse produced one output pulse. At that point the temporal and spectral profile of the microchip pulse was measured.

The output of the microchip lasers was observed with a fast photodetector connected to an oscilloscope and with a linear diode array at the output of a 3/4-m spectrometer. The response of the photodetector system was calibrated with a standard large-cavity mode-locked Nd:YAG laser. The mode-locked pulses had a duration (full width at half-maximum) of  $100 \pm 20$  ps and resulted in a detector response with an 800-ps duration. The spectrometer system had a 0.05-nm resolution.

Under the experimental conditions described above, the output pulse from the Nd:YAG microchip laser with the 0.3 percent output coupler had a typical duration of 2.5 ns. This value is very close to the calculated cavity lifetime of 2.3 ns, which assumes that the only sources of loss in the microchip cavity are the two mirrors. The spectral measurements were instrument limited, showing that only one longitudinal mode of the microchip laser was oscillating. Visual inspection of the far-field pattern indicated that the laser was operating in the TEM<sub>00</sub> mode.

The output pulse from the Nd:YAG microchip laser with the 1.3 percent output coupler produced a 1.2-ns photodetector response. Numerical deconvolution of the response to the mode-locked laser from this response resulted in the pulse shown in Figure 2-1, with a duration of 800 ps. This output pulse is again comparable to the calculated microchip cavity lifetime of 650 ps. This microchip laser also operated in a single longitudinal and transverse (TEM<sub>00</sub>) mode.



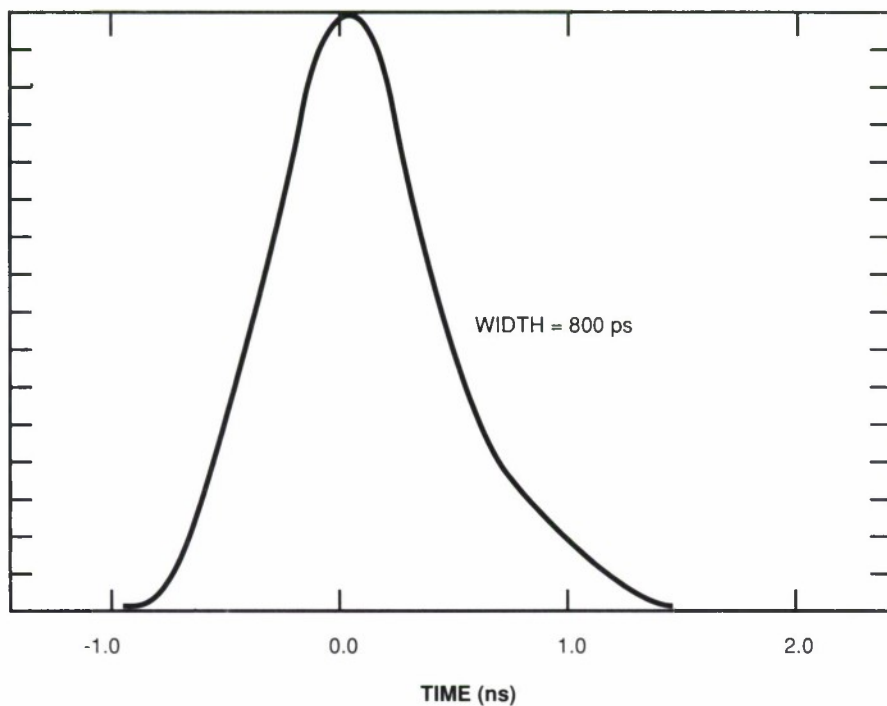


Figure 2-1. Deconvolved output pulse of a Nd:YAG microchip laser when pumped with a 40-ns Ti:Al<sub>2</sub>O<sub>3</sub> pulse. The microchip laser cavity is 750  $\mu$ m long, with a 1.3 percent output coupler.

It was difficult to adjust the Ti:Al<sub>2</sub>O<sub>3</sub> laser so that each of the pump pulses consistently resulted in only one output pulse from the LNP microchip laser. It was easy, however, to obtain trains of 4 or 5 output pulses due to relaxation oscillation spiking from the microchip laser, with the pulses separated by 3 to 4 ns. When this was done, the photodetector response to each of the pulses was shorter than the response to the mode-locked Nd:YAG pulses, setting an upper limit to the pulse duration of 120 ps. This is to be compared with the calculated cavity lifetime which is also 120 ps. With a shorter pump pulse it should be possible to obtain single pulses of this duration from the microchip laser. As in the case of the Nd:YAG microchip lasers, the LNP microchip laser operated in the TEM<sub>00</sub> mode and in a single longitudinal mode.

Unlike mode-locked pulses, single gain-switched pulses can be generated. The experiments described above demonstrate that it is possible to obtain very short, single-frequency, gain-switched pulses from microchip lasers. The duration of the output pulse is limited by the microchip cavity lifetime. By decreasing the cavity lifetime, through the use of lower reflectivity output mirrors or shorter cavities, it should be possible to produce microchip lasers with output pulses of much less than 100 ps. The pulsed capabilities of the microchip laser, coupled with its small size, simple fabrication, and compatibility with commercially available laser diode pumps,<sup>1</sup> should make it a useful device for a large range of applications, including optical communications.

J.J. Zayhowski  
A. Mooradian  
J. Ochoa

## 2.2 SUPPRESSION OF LASER SPIKING BY INTRACAVITY SECOND-HARMONIC GENERATION

Many pulsed laser systems exhibit pronounced laser spiking, or relaxation oscillations, when operated with a long pulse length. This spiking is detrimental to several applications, including medicine where fiber-optic delivery of high-energy, low-power, pulsed laser radiation is required, and sum-frequency mixing where the independent spiking of two laser pulses results in low mixing efficiency. The efficient suppression of laser spiking, by intracavity second-harmonic generation, in long-pulse, pulse-pumped 1.06- and 1.32- $\mu\text{m}$  Nd:YAG lasers is reported here.\*

Laser spiking is caused by the development of laser gain which is much greater than the steady-state, or threshold, gain. The absence of appreciable stimulated emission at the start of laser pumping allows the laser gain to rise substantially beyond the threshold gain. This initial high gain leads to the rapid buildup of a high radiation intensity. The high intensity then depletes the gain, which results in a greatly reduced radiation intensity. The low radiation intensity and continued laser pumping allow the redevelopment of high laser gain. This cycle of low intensity, high gain followed by high intensity, low gain continues through the rest of the laser pulse, with a damping rate depending on several factors including the laser pumping rate and the laser cavity losses. The spiking behavior of a 1.06- $\mu\text{m}$  Nd:YAG laser is illustrated in Figure 2-2(a). In addition to the initial spiking, the laser spiking behavior is often reexcited during the pulse by various cavity perturbations such as acoustic noise.

Laser spiking has been of interest since the development of the ruby laser and has previously been suppressed in ruby laser systems by the insertion of both active and passive elements into the laser cavity. Active suppression has been accomplished by high-voltage, high-speed negative feedback to an intracavity Pockel's cell,<sup>3</sup> while passive suppression has been accomplished via stimulated Rayleigh wing scattering in an intracavity benzene cell.<sup>4</sup> Laser spiking has also been passively suppressed in neodymium laser systems through mutually coupled Nd:glass lasers<sup>5</sup> and notably through intracavity second-harmonic generation in continuously pumped, cavity-dumped or mode-locked 1.06- $\mu\text{m}$  Nd:YAG lasers.<sup>6</sup>

Here the suppression of laser spiking by intracavity second-harmonic generation is extended to pulse-pumped lasers where the spiking behavior is typically much more severe than in continuously pumped lasers. The laser spiking is suppressed by an intracavity nonlinear crystal which more efficiently converts high-intensity laser spikes into second-harmonic radiation. Since the peak intensity of the initial laser spike is substantially reduced, it does not drive the laser gain as far below threshold. As a result the laser spiking behavior damps out at a much higher rate than in the absence of intracavity doubling and the redevelopment of spiking is suppressed. The suppression of laser spiking is shown in Figure 2-2(b).

---

\* In a private communication, Peter Moulton of Schwartz Electro-Optics disclosed that he has also suppressed laser spiking in long-pulse 1.064- $\mu\text{m}$  Nd:YAG and 1.047- $\mu\text{m}$  Nd:YLF lasers by intracavity second-harmonic generation.

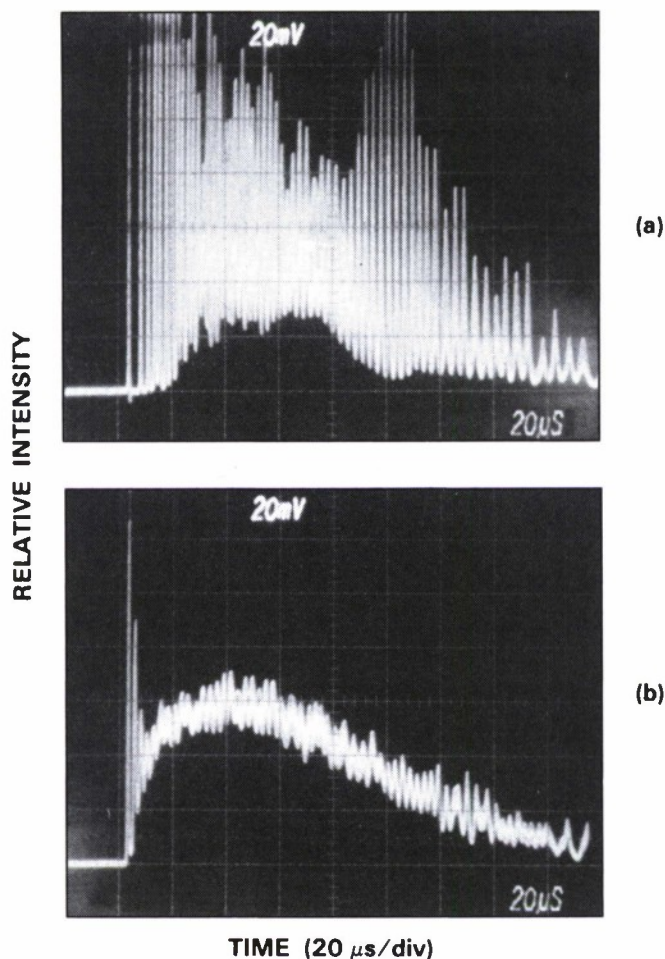


Figure 2-2. Temporal profiles of 160-mJ,  $TEM_{00}$ , 1.06- $\mu\text{m}$  laser pulses (a) without intracavity second-harmonic generation and (b) with intracavity second-harmonic generation.

Spiking was suppressed in a 1.5-m-long, 1.06- $\mu\text{m}$  laser cavity, which consisted of a 40 percent output coupler, a flash-lamp-pumped Nd:YAG rod, a beam-expanding telescope (for greater mode filling of the Nd:YAG rod), a dielectric polarizer, a 1-cm-long antireflection-coated lithium iodate crystal, and a high reflector with a 7-m radius of curvature. An intracavity aperture restricted laser oscillation to the  $TEM_{00}$  cavity mode. The laser emitted 160 mJ per pulse at 10 Hz. When phase matched the lithium iodate crystal generated about 0.8 mJ of second-harmonic radiation per pulse. Thus, laser spiking was substantially suppressed with less than 1 percent loss of the 1.06- $\mu\text{m}$  radiation. Figure 2-3 shows the leading edge of the 1.06- $\mu\text{m}$  laser pulse both with and without intracavity second-harmonic generation. Second-harmonic generation resulted in a reduction of the first laser spike by a factor of 3 and in nearly complete damping after the first several oscillations. In addition, harmonic generation nearly doubled the pulse length of the

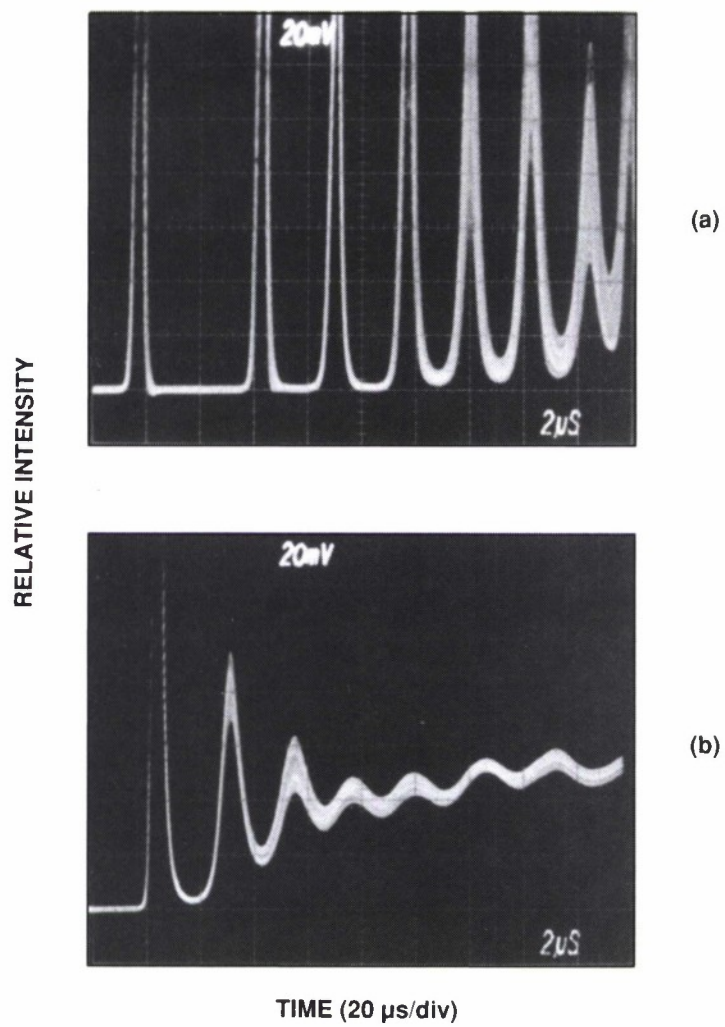


Figure 2-3. Leading edges of 1.06- $\mu$ m laser pulses (a) without intracavity second-harmonic generation and (b) with intracavity second-harmonic generation.



initial laser spike.<sup>7</sup> If needed, these first oscillations may be “clipped” off of the pulse by an external Pockel’s cell. The temporal profile of such a clipped pulse is shown in Figure 2-4. This pulse left the Pockel’s cell with an energy of 150 mJ and was then amplified in a single-pass amplifier to an energy of 1.1 J.

The rate of damping of laser spiking may be increased by increasing the second-harmonic conversion efficiency. This may be done in several ways, including increasing the intracavity radiation fluence through decreased output coupling, using a nonlinear crystal with a high nonlinear coefficient, and positioning the nonlinear crystal at an intracavity beam waist. Increased second-harmonic generation may also be obtained through mode-locking. When mode-locked, the peak power of the laser radiation is increased and second-harmonic radiation is generated with greater

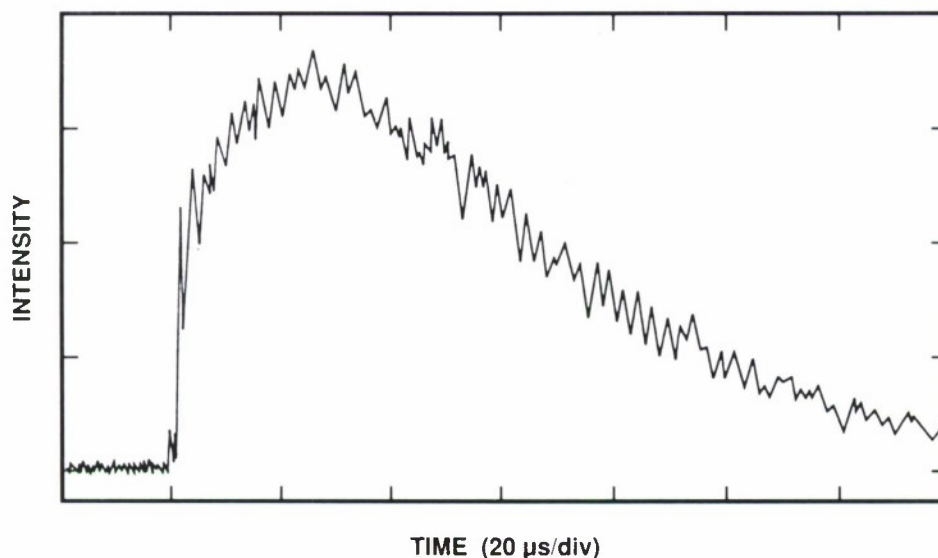


Figure 2-4. Temporal profile of 1.06- $\mu\text{m}$  spike-suppressed pulse after the leading spikes were “clipped” off by an external Pockel’s cell and the resulting 150-mJ pulse was amplified in a single-pass amplifier to 1.1 J.

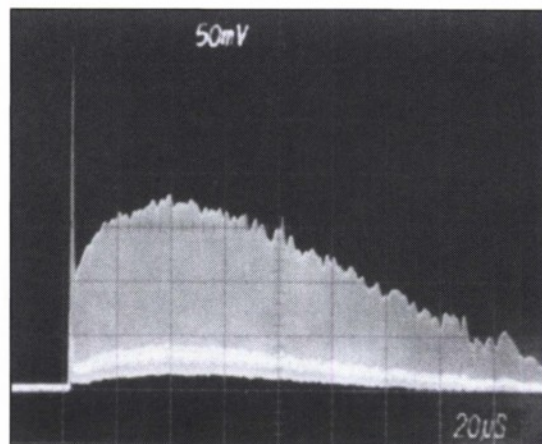
efficiency. Near critical damping has been achieved as shown in Figure 2-5. In this case, second-harmonic generation results in a 6 percent loss in 1.06- $\mu\text{m}$  pulse energy. In addition, the second-harmonic generation stretches the mode-locked micropulse length.

Similar spiking suppression has been obtained in a 1.32- $\mu\text{m}$  Nd:YAG laser and is illustrated in Figure 2-6. Again this suppression resulted in less than 1 percent loss of laser pulse energy.

In conclusion, intracavity second-harmonic generation results in substantial suppression of laser spiking behavior with little loss in pulse energy. In addition, it is easy to implement and requires only minor mirror adjustment in order to reestablish optimum laser power output, after installation of the nonlinear crystal.

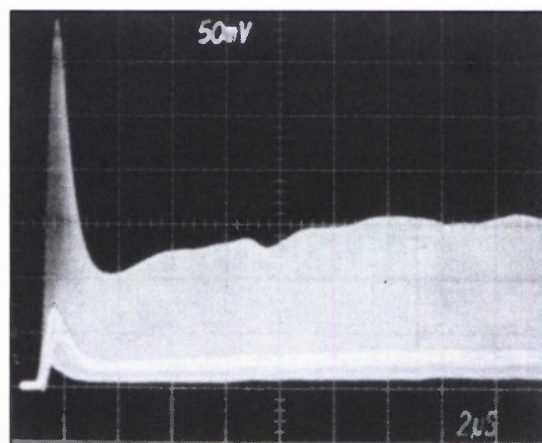
T.H. Jeys

RELATIVE INTENSITY



(a)

TIME (20  $\mu$ s/div)



(b)

TIME (2  $\mu$ s/div)

Figure 2-5. Temporal profiles of mode-locked 1.06- $\mu$ m laser pulse with intracavity second-harmonic generation.

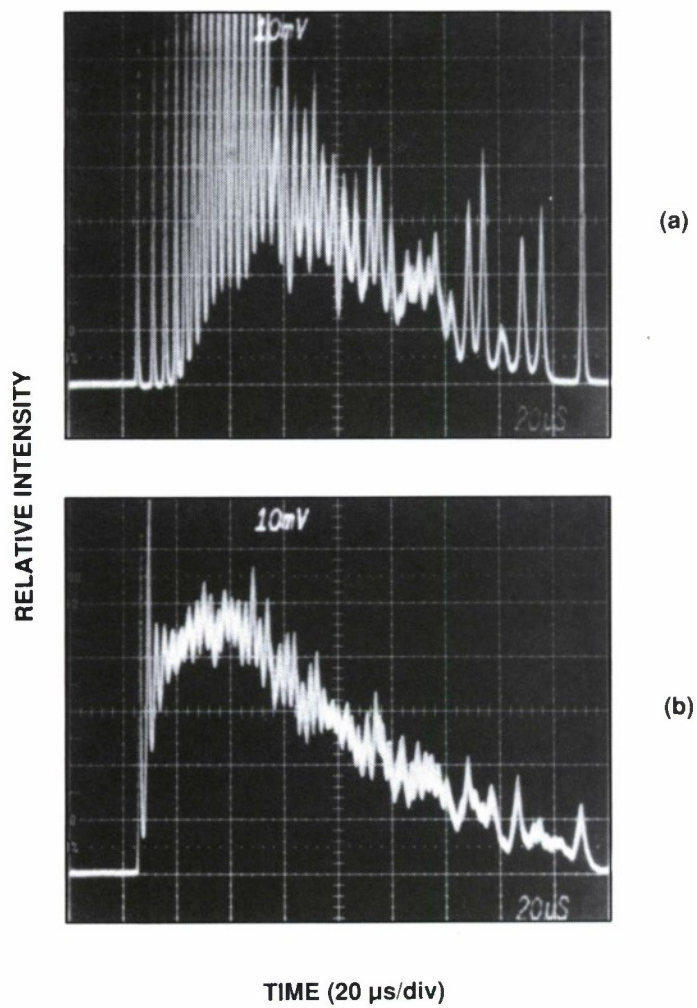


Figure 2-6. Temporal profiles of 70-mJ,  $TEM_{00}$ , 1.32- $\mu$ m laser pulses (a) without intracavity second-harmonic generation and (b) with intracavity second-harmonic generation.

## 2.3 SCALABLE END-PUMPED Nd:YAG LASER

A pumping scheme that offers the potential for an order of magnitude power scaling of end-pumped lasers has been experimentally demonstrated. Diffraction-limited output with a power of 520 mW has been obtained from an Nd:YAG laser pumped with three diode laser arrays.

The highest efficiency diode-laser-pumped lasers with good beam quality have been demonstrated using an end-pumped geometry. However, end-pumped lasers have been limited to low power because of difficulties in scaling. Typically only one or two pump sources are simultaneously used to excite the laser. Some techniques used to scale end-pumped lasers include polarization coupling, higher power pump sources,<sup>8</sup> multiple pump sources using fiber coupling,<sup>9</sup> and providing multiple "ends" by using many gain elements.<sup>10</sup> All of these have their disadvantages. Polarization coupling allows only a factor of 2 increase in pump power. Using higher power pump sources depends on the development of these sources. Fiber coupling is inefficient because of coupling losses, and using multiple gain elements adds complexity. Our technique is simple and takes advantage of the difference in beam quality from the diode laser in the planes perpendicular and parallel to the junction.

Figure 2-7 shows a schematic of our experiment in the planes parallel and perpendicular to the junction of the diode arrays. These diode arrays are from Spectra Diode Laboratories, SDL-2430-C, and have an output power of 500 mW. Their output beams are diffraction limited in the plane perpendicular to the junction. Each of these outputs is collimated by a 0.4-cm focal length lens. The arrays are spaced 1 cm apart in the plane perpendicular to the junction. Focusing of the pump radiation into the fundamental mode volume of an end-pumped laser is limited by the beam quality of the pump beam. If only a single one of these arrays is used for pumping, then the 25 times diffraction limited beam quality in the plane of the junction limits how small a volume can be pumped in the gain medium. Thus, as long as the beam quality in the orthogonal plane is less than 25 times diffraction limited, the pump volume need not increase. Calculations show that the output of the three-array pump source shown in Figure 2-7 is less than 25 times diffraction limited in the plane perpendicular to the junction. After collimation the beam from a single array is nominally 0.4 cm wide in the plane perpendicular to the junction. The pump beam as a whole in this plane has the far-field diffraction angle of a single collimated array but out of an aperture that is now about 2.4 cm. Thus, the pump beam quality in this plane is nominally six times diffraction limited.

The pump beam was focused into a Nd:YAG rod using cylindrical optics since the beam in the two orthogonal planes is different. The Nd:YAG rod was coated with a high reflector at  $1.06\ \mu\text{m}$  on one face and an antireflection coating on the other. The output mirror has 97.5 percent reflectivity at  $1.06\ \mu\text{m}$ . Preliminary results are shown in Figure 2-8. Laser operation was obtained with each diode array operating separately. In each case the output was in a  $\text{TEM}_{00}$  mode and as the pump source was switched from one array operating separately to another, neither the laser cavity nor the focusing optics were realigned. With all three arrays operating, the output was still  $\text{TEM}_{00}$  and we were able to obtain nearly four times the output power compared with pumping with a single array.



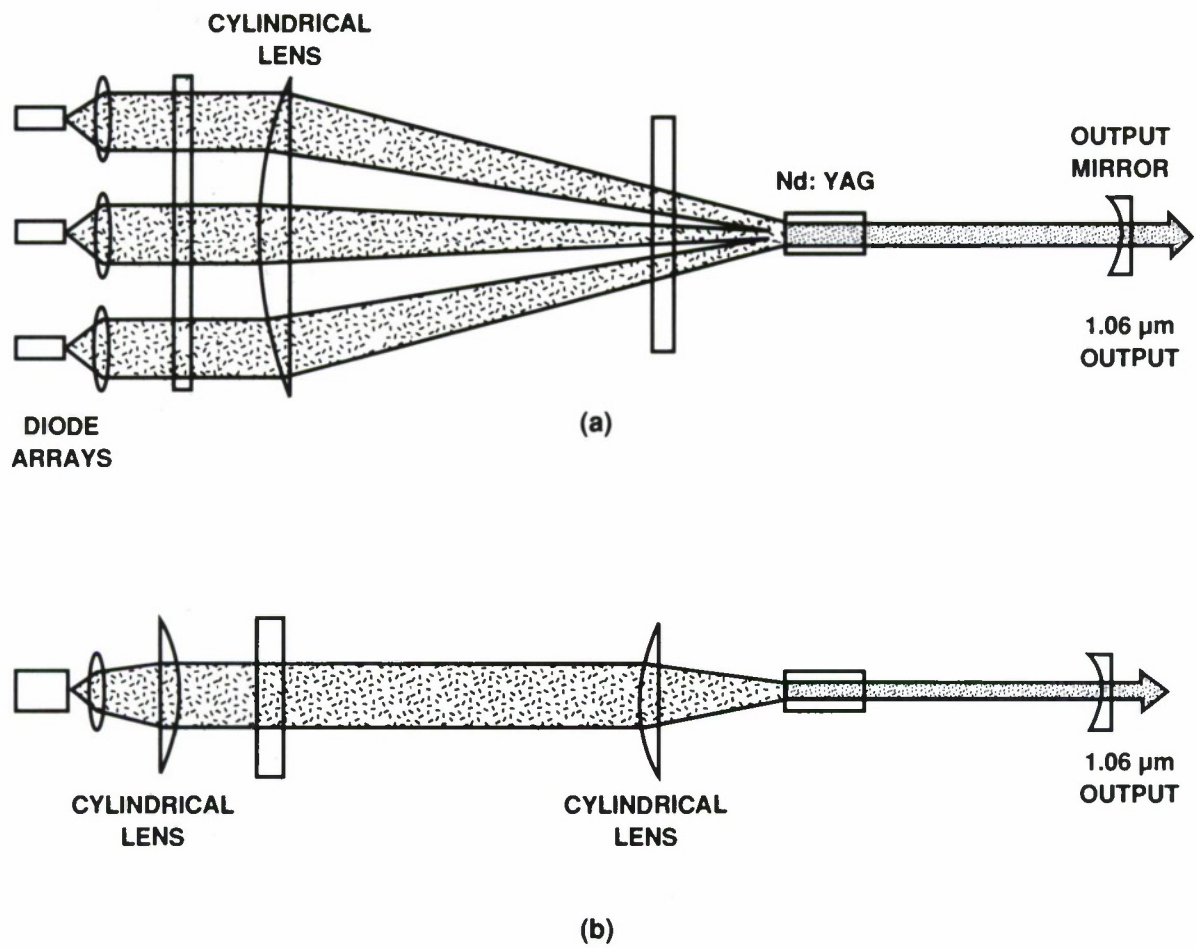


Figure 2-7. Schematic of the scalable end-pumped laser experiment. (a) Plane perpendicular to the junction. (b) Plane parallel to the junction.

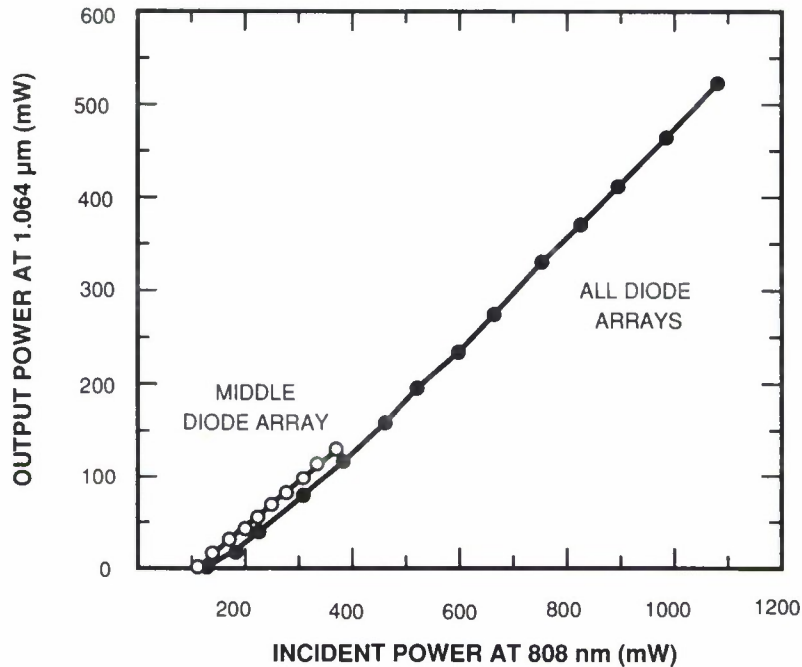


Figure 2-8. Continuous wave output power as a function of input power for the middle array and all three arrays. The output for the other two arrays operating individually are not shown for reasons of clarity, but their output powers are slightly less than the middle array.

Simple scaling arguments indicate that over an order of magnitude pump power increase in the same mode volume can be obtained using the pumping scheme of Figure 2-7 compared with using a single array. This technique thus allows higher pump intensity at the gain medium, which is desirable for low-gain, tunable, and quasi-three-level lasers.<sup>11</sup>

T.Y. Fan  
A. Sanchez  
W.E. DeFeo

## 2.4 LATERAL-MODE STRUCTURE OF EXTERNAL-CAVITY DIODE LASERS WITH RESIDUAL FACET REFLECTIVITY

This work is aimed at developing an efficient laser source with high brightness by using a simple, versatile external resonator of the type shown in Figure 2-9 to provide spatial (lateral) mode selection in broad-stripe, high-power laser diodes. In order to ensure that the lateral modes of the laser are controlled by the external cavity, a good antireflection (AR) coating is required on the front diode facet which faces the output coupler. In this report, some of the effects of the residual front-facet reflectivity on the lateral coherence of external-cavity diode lasers are demonstrated. Henceforth, the modes of the composite external-cavity laser will be referred to as "cavity modes," and the modes of the solitary diode as "diode modes." The term "monolithic modes" refers to the diode modes in the presence of weak feedback in the external cavity.

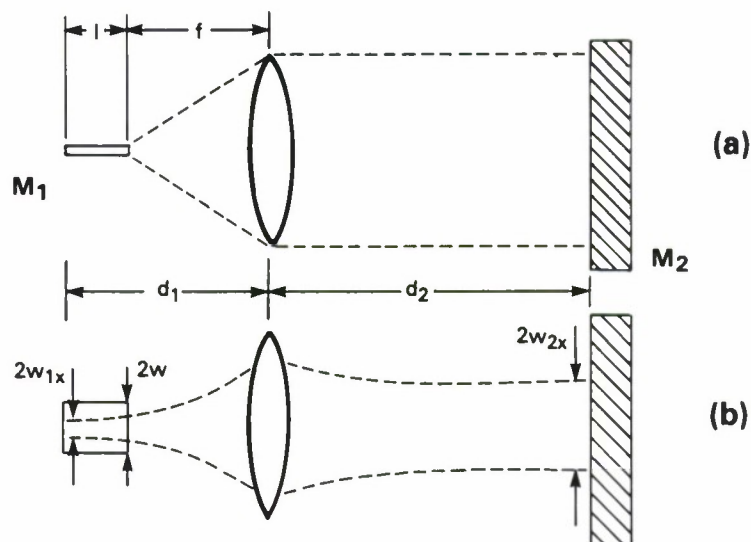


Figure 2-9. Schematic of the external-cavity laser.

The relatively large internal loss that is characteristic of a laser diode requires that the residual front-facet reflectivity be of the order of  $10^{-2}$ , for example, to double the lasing threshold of the solitary device when only this facet has been coated. The lasers used in this work have high-reflection, rear-facet coatings and AR-coated front facets so that their lasing thresholds are typically less than twice their thresholds prior to coating. When high-power, external-cavity operation is desired, as in this work, either lower facet reflectivity, or AR coating of both facets is necessary to avoid parasitic oscillation of the monolithic diode in the external cavity. If the oscillation of high-order cavity modes is suppressed such that the lateral dimension of the external-cavity mode is smaller than the width of the active region of the diode, then the gain will not be saturated across the entire width by the external-cavity mode. Upon reaching the threshold of the coated, solitary diode, the laser will oscillate simultaneously in the monolithic and cavity modes. A result of this condition is illustrated in Figure 2-10 in which the power vs current relationship is shown for an external-cavity laser with an intracavity aperture. The aperture (slit) was used to select the fundamental lateral mode of the external resonator, filling the central part of the active region. A sharp decrease in the slope efficiency of the apertured laser is observed as the current passes through the threshold of the solitary diode (0.8 A). The change occurs because the tails of the intensity profiles of the diode and cavity modes overlap in a region of unsaturated gain where both can simultaneously oscillate. The diode modes and cavity mode compete for gain in the laser, thus depleting the available single-frequency power of the latter.

The overlap between the fundamental cavity mode profile and the gain profile is generally insufficient to ensure the desired single-mode operation without an aperture, when the external-mirror feedback is centered in the active region of the diode. However, if the feedback is displaced to one side of the active region, the laser operates in a single-frequency, diffraction-limited

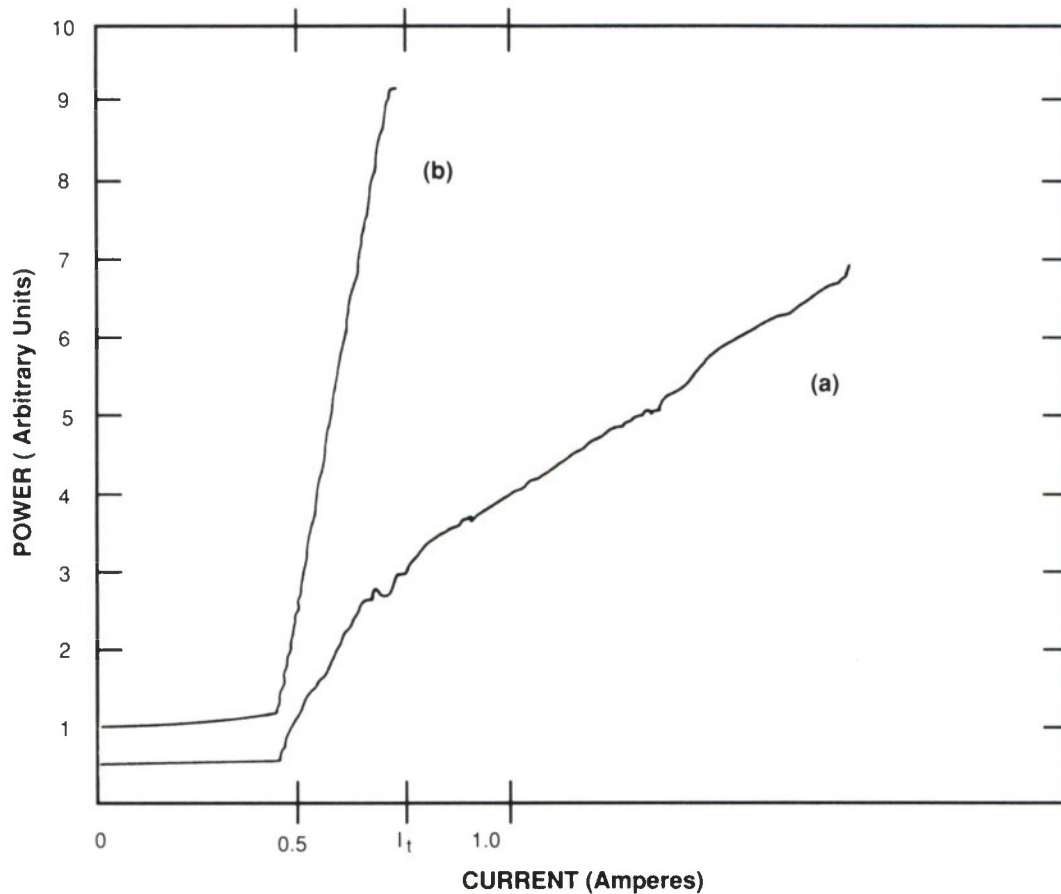


Figure 2-10. (a) Power vs current for apertured external-cavity laser. The aperture permits single-frequency operation at currents up to the threshold,  $I_t$ , of a solitary diode indicated in the figure. (b) Power vs current for same laser without aperture.

mode when biased below the threshold of the monolithic diode. We propose that this alignment configuration favors the fundamental mode by increasing the relative losses of the higher-order modes by absorption in the outermost part of the mode profile which penetrates the unpumped regions of the diode surrounding the active region. The output spectrum of the laser at 0.6 W of total power (1.8 A of injected current) continues to be dominated by the single-frequency spectrum of the low-power laser, as shown in Figure 2-11(a). The full spectrum, shown in Figure 2-11(b) with less resolution, reveals an apparent superposition of a single-frequency signal and a broad hump characteristic of the solitary device. Figure 2-12 shows a spatially resolved spectrum of the near-field of the diode in the displaced-feedback cavity configuration. The picture is obtained by imaging the front facet of the diode on the entrance slit of a monochromator from which the exit slit has been removed. The dispersed spectrum in the exit plane is reimaged and recorded using a video camera and monitor. The figure clearly shows that the strong single-frequency component and the hump of Figure 2-11(b) originate from distinct regions of the diode. A single-frequency source producing about 0.35 W could be made by using an aperture outside the cavity to mask part of the magnified image of the diode facet.



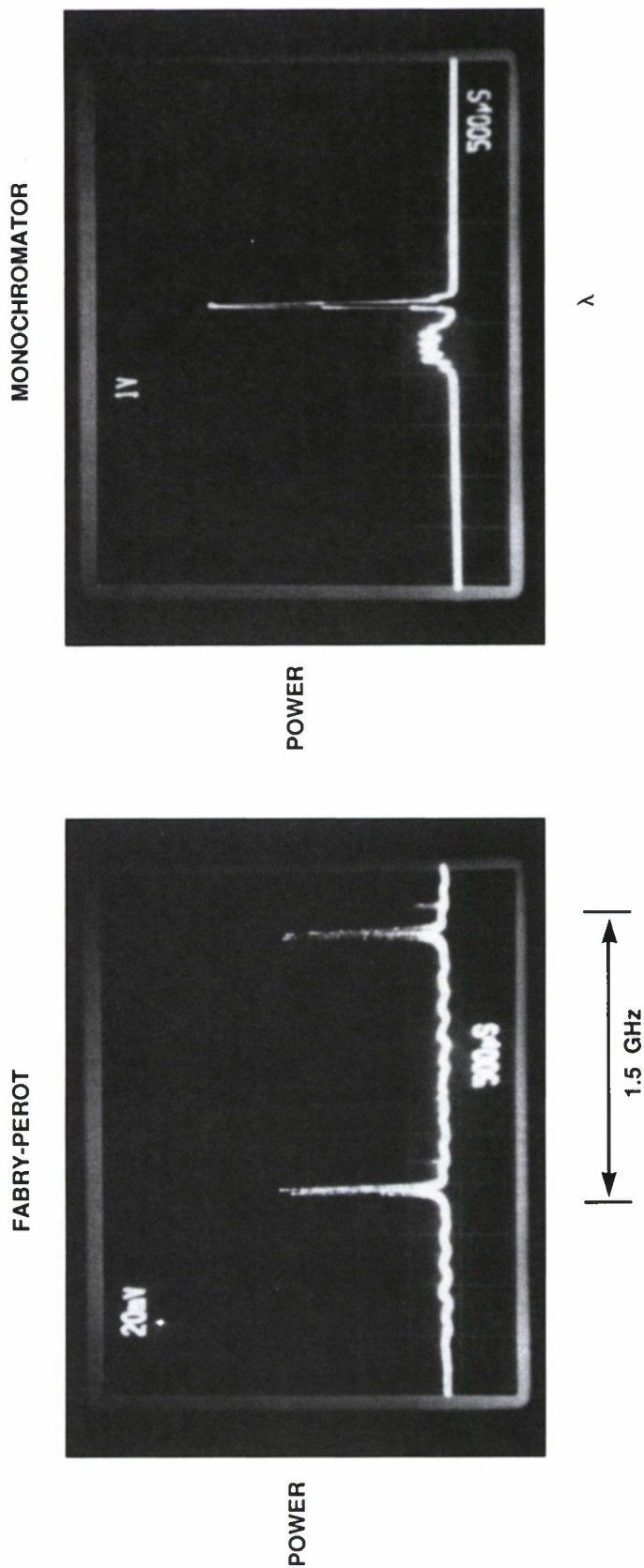


Figure 2-11. (a) Fabry-Perot spectrum of output from a 0.6-W external-cavity laser with displaced feedback, showing predominant single-frequency component of spectrum. (b) Monochromator (low-resolution) spectrum of laser output showing strong single-frequency signal from the region of the diode with strong feedback, and broad hump originating from the region of the diode with weak optical feedback.

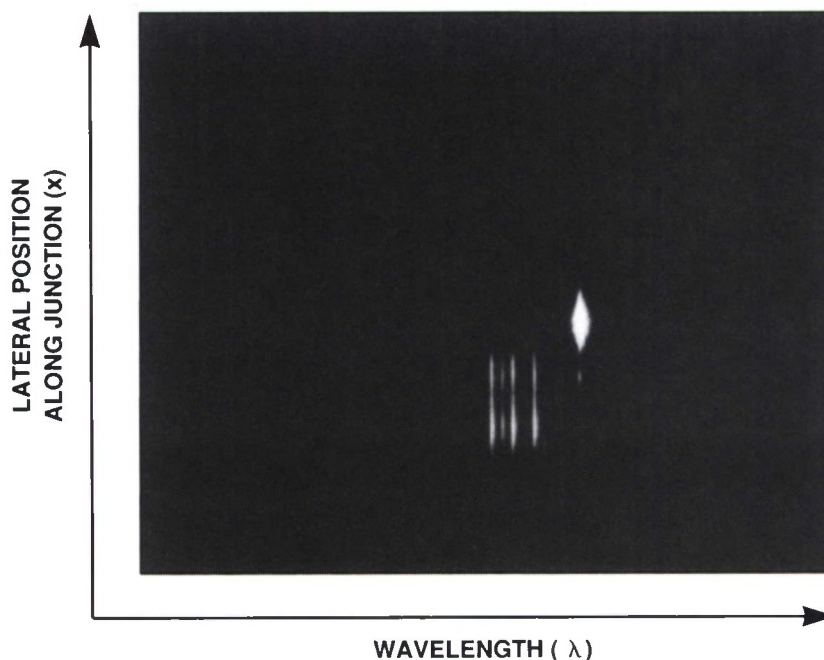
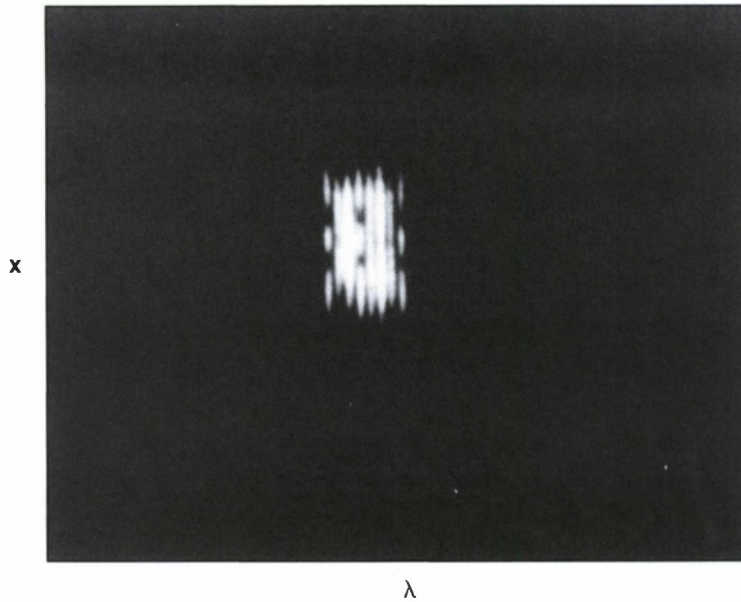


Figure 2-12. Spatially resolved nearfield spectrum of diode in external cavity with displaced feedback. The bright, single-frequency spot and the broad, weaker spectrum originate from distinct spatial regions of the diode.

In most cavities the lateral gain distribution across the diode stripe (i.e., the carrier density profile) is generally flat relative to the intensity profile of the fundamental cavity mode across the same spatial region. The incomplete spatial overlap of the gain profile and the fundamental mode profile permits oscillation of higher-order lateral modes at high powers. However, it is possible for these modes to oscillate even at low powers if there is sufficient modulation of the gain spectrum arising from the residual Fabry-Perot effects of the monolithic cavity. Although a coupled-mode analysis is required for a proper description of the laser, we consider the simpler problem of simultaneously satisfying the boundary conditions for the short (diode) and long (external) cavity. The axial mode-spacing of the former is about 20 times that of the latter, for the 600- $\mu\text{m}$ -long diode in a 4.5-cm-long cavity used to obtain the data in Figure 2-13. The coincidence of the diode- and cavity-mode frequencies at wavelengths near the maximum of the gain spectrum is not generally assured in the fundamental lateral mode of the cavity, but is allowed by the lateral-mode dispersion of the cavity. The lateral-mode spacing of the cavity is about half that of the axial modes. When the laser oscillates in more than one lateral mode and at multiple wavelengths separated by the axial mode spacing of the monolithic diode, Figure 2-13 shows that each lateral mode is repeated at approximately regular intervals corresponding to four to five axial diode-mode spacings. There is one lateral mode associated with each longitudinal diode mode. The regular repetition of each lateral mode is consistent with the simultaneous occurrence of two resonant-mode spacings (i.e., that of the diode and that of the external cavity), resulting in a low-“frequency” (large-interval) beat with a period of four longitudinal diode-mode spacings.



126266-17

*Figure 2-13. Spatially resolved nearfield spectrum of diode in external cavity with insufficient mode selectivity resulting from residual Fabry-Perot effects. Each lateral mode repeats at regular intervals corresponding to about four axial diode-mode spacings. Many lateral modes have similar net gain.*

We have shown some of the limitations imposed by the residual reflectivity of antireflection coatings on the performance of high-power, wide-stripe, external-cavity diode lasers. We have also demonstrated a 0.35-W, single-frequency source, even with these limitations. Laser brightness is limited by parasitic oscillation of the monolithic diode in the external cavity and modulation of the gain spectrum of the laser from residual Fabry-Perot effects of the diode. The latter may cause many high-order lateral modes to have the same net gain, that is, larger than that of the desired fundamental mode.

W.F. Sharfin  
A. Mooradian

## REFERENCES

1. J.J. Zayhowski and A. Mooradian, Opt. Lett. **14**, 24 (1989).
2. J.J. Zayhowski and A. Mooradian, Opt. Lett. **14**, to be published.
3. R.F. Marshall and D.L. Roberts, Proc. IRE **50**, 2108 (1962); H. Statz, G.A. DeMars, D.T. Wilson, and C.L. Tang, J. Appl. Phys. **36**, 1510 (1965); D.V. Keller and B.I. Davis, IEEE J. Quantum Electron. **QE-2**, 179 (1966).
4. R.H. Pantell and J. Warszawski, Appl. Phys. Lett. **11**, 213 (1967).
5. A.M. Bonch-Bruevich, S.E. Patonov, and Ya. A. Imas, Sov. Phys. Tech. Phys. **13**, 44 (1968).
6. C.J. Kennedy and J.D. Barry, IEEE J. Quantum Electron. **QE-10**, 596 (1974); C.J. Kennedy, IEEE J. Quantum Electron. **QE-12**, 256 (1976); C.J. Kennedy, J.D. Barry, and R.R. Rice, J. Appl. Phys. **47**, 2447 (1976).
7. J.E. Murray and S.E. Harris, J. Appl. Phys. **41**, 609 (1970); J.F. Young, J.E. Murray, R.B. Miles, and S.E. Harris, Appl. Phys. Lett. **18**, 129 (1971); V.G. Dmitriev and E.A. Shalaev, Sov. J. Quantum Electron. **9**, 123 (1979).
8. D.L. Sipes, Appl. Phys. Lett. **47**, 74 (1985).
9. K. Kubodera and J. Noda, Appl. Opt. **21**, 3466 (1982).
10. J. Frauchiger, P. Albers, and H.P. Weber, *Technical Digest of Tunable Solid State Lasers* (Optical Society of America, Washington, D.C., 1989), paper TuC2.
11. T.Y. Fan and R.L. Byer, IEEE J. Quantum Electron. **QE-23**, 605 (1987).



### 3. MATERIALS RESEARCH

#### 3.1 DETERMINATION OF MBE GROWTH RATE BY DIGITAL SIGNAL PROCESSING OF TIME-DEPENDENT RHEED INTENSITY DATA

The examination of images formed by *in situ* reflection high energy electron diffraction (RHEED) is one of the most useful tools for the analysis of growth by molecular beam epitaxy (MBE).<sup>1</sup> Static RHEED images, obtained when growth is interrupted, yield detailed information on surface reconstruction. Analysis of dynamic RHEED images, obtained as growth is taking place, can be employed to determine epitaxial growth rates. This method is applicable because epitaxial growth causes a variation in surface roughness on the atomic scale that under favorable conditions produces well-defined oscillations in the RHEED intensity whose period is the time required for the growth of one complete monolayer.<sup>2</sup> Frequently, however, the conditions required for optimum epitaxial growth do not yield oscillations that are sufficiently obvious to permit the period to be obtained directly from plots of intensity vs time. We are developing a technique that uses digital signal processing methods to extract the period from RHEED data obtained under such conditions.

The new technique has been used to analyze data obtained during the growth of GaAs epilayers in a Varian Gen II MBE system equipped with a standard 10-keV electron gun and diametrically opposite phosphor RHEED screen. A TV camera transfers the RHEED image to a Colorado Video Model 321 video analyzer and a TV monitor. Any pixel of the video image can be selected for analysis. A voltage signal proportional to the intensity of this pixel is transmitted from the analyzer to an X-Y recorder with a time base and also to a digital voltmeter. The voltmeter samples the incoming signal at rates between 30 and 70 samples/s and produces a digital output that is transferred via an IEEE-488 bus to a desktop computer for processing. A commercial software package was used in developing the data acquisition and analysis routines.

In this study, the following conventional procedure has generally been employed in obtaining the RHEED oscillation data. A thin epitaxial GaAs layer is first grown on a (100) GaAs substrate. Growth is then interrupted momentarily by closing the shutter on the Ga source while keeping the As shutter open to maintain an As-stabilized surface. A pixel is selected on one of the streaks of the pattern generated by RHEED diffraction in a fixed azimuthal direction, and collection of intensity data is initiated. Growth is resumed by reopening the Ga shutter, continued for a predetermined interval, and again interrupted by closing the Ga shutter. Data collection is terminated at some later time while only the As shutter is open.

Figure 3-1 is a recorder trace of voltage vs time that was obtained for a run in which the growth conditions were optimized for obtaining well-defined RHEED oscillations. (The voltage plotted is not linearly related to the pixel intensity, since the video-analyzer signal has been offset by a dc bias supplied by the recorder.) Opening the Ga shutter produces an abrupt change in intensity, which is followed by a large number of distinct oscillations that decay in amplitude with time. When the Ga shutter is closed, the intensity again changes rapidly to

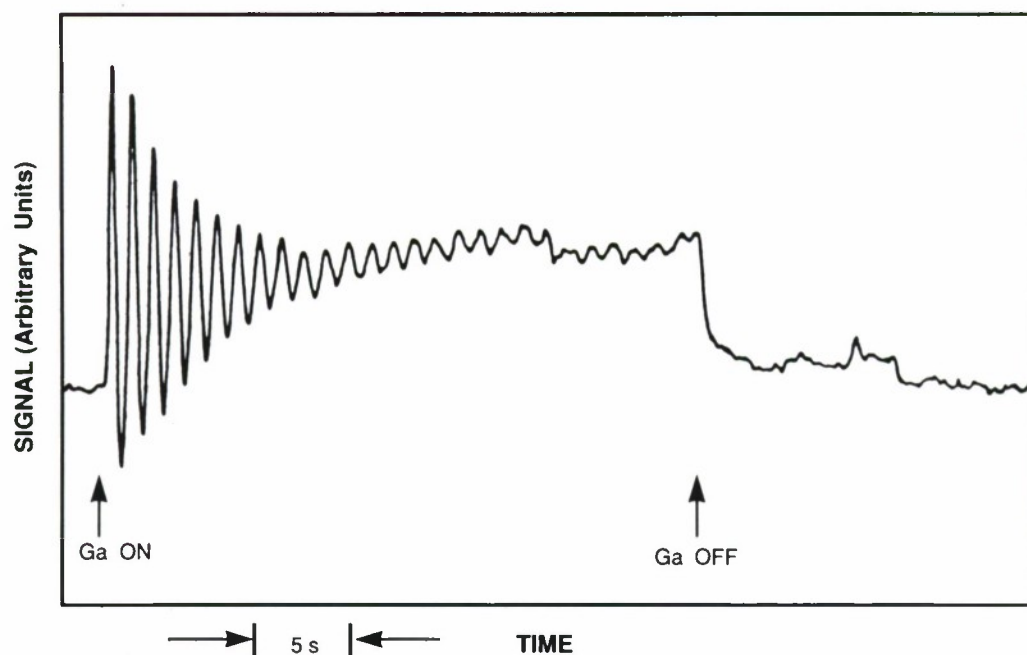


Figure 3-1 RHEED signal vs time for growth of GaAs on (100) GaAs substrate.

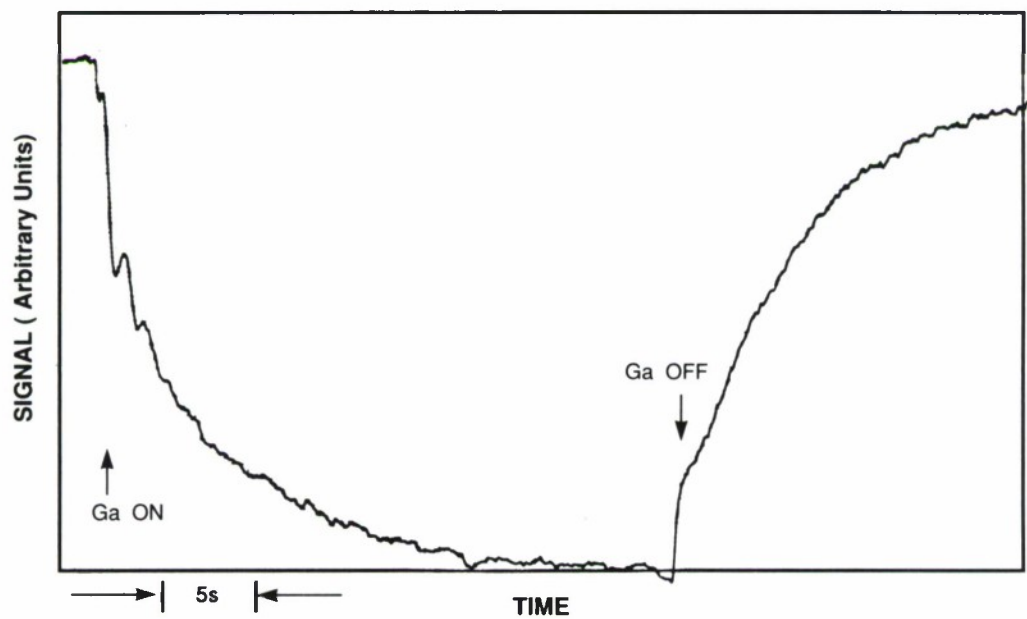


Figure 3-2 RHEED signal vs time for growth of GaAs on inferior (100) GaAs substrate.

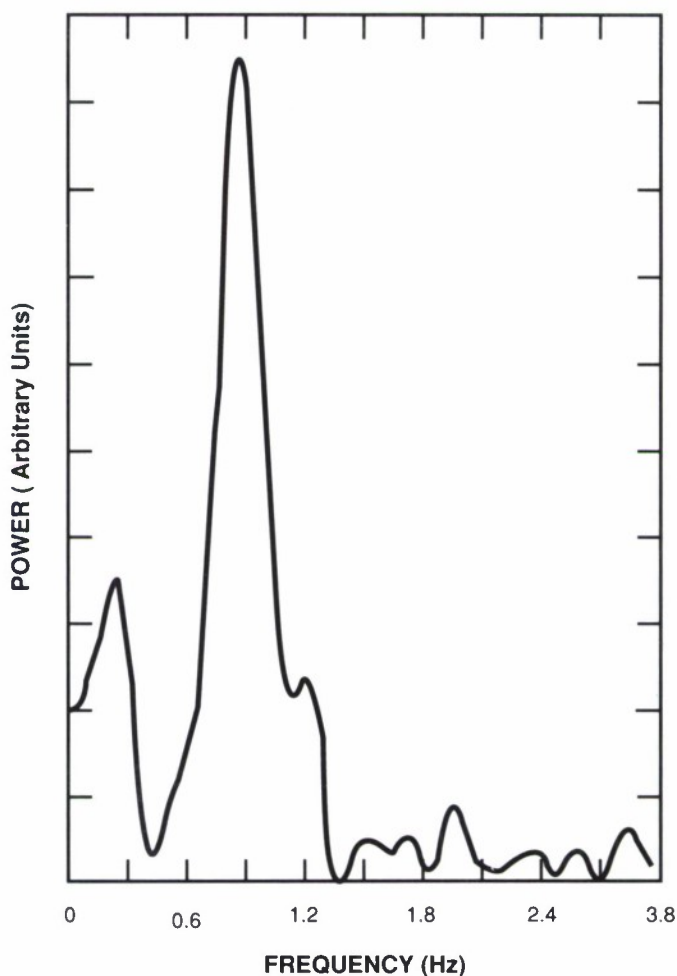


Figure 3-3 Power spectrum obtained by digital signal processing of RHEED data for experiment of Figure 3-2.

approximately the initial value, and no further oscillations are observed. The average frequency determined from the time required for the first 17 oscillations is 0.879 Hz, which corresponds to a growth rate of 0.894  $\mu\text{m/h}$ , since the height of a (100) GaAs monolayer is half the lattice constant ( $a_0 = 0.56533 \text{ nm}$ ).

Figure 3-2 is a recorder trace obtained on another day for growth under similar conditions but on a GaAs substrate of inferior quality. In this case the oscillations are so weak and indistinct that the frequency cannot be determined by inspection of the recorder trace. However, we have been able to extract the frequency by applying our signal processing technique to the digital voltmeter data stored in the computer. The voltmeter sampling rate was first determined by dividing the total measurement time by the number of samples. Next a baseline correction was performed to compensate for the long-term nonperiodic variation in the signal. Finally a power

spectrum was obtained by fast Fourier transform analysis. This spectrum, which is shown in Figure 3-3, contains a dominant peak at 0.860 Hz, corresponding to a growth rate of 0.875  $\mu\text{m/h}$ . The good agreement between this value and the growth rate determined from Figure 3-1 is evidence for the validity of the signal processing technique, since the growth rate of GaAs under the conditions employed in the two experiments is primarily determined by the Ga flux, which was nominally the same in both cases. As further evidence for the validity of the signal processing technique, excellent agreement is obtained when both this technique and the inspection method can be applied to the results of the same growth experiment. For example, the growth rate determined by the signal processing technique for the experiment of Figure 3-1 is 0.887  $\mu\text{m/h}$ , which agrees to within 1 percent of the value obtained by inspection.

G.W. Turner

B.A. Nechay

S.J. Eglash

## REFERENCES

1. R. Ludeke, R.M. King, and E.H.C. Parker, in *The Technology and Physics of Molecular Beam Epitaxy*, E.H.C. Parker, Ed. (Plenum, New York, 1985), p. 555.
2. J.H. Neave, B.A. Joyce, P.J. Dobson, and N. Norton, *Appl. Phys. A* **31**, 1 (1983).



## 4. SUBMICROMETER TECHNOLOGY

### 4.1 OPTICAL PROPERTIES OF FUSED SILICA EXPOSED TO 193-nm RADIATION FROM AN EXCIMER LASER

High-purity, synthetic fused silica is the material of choice for varied optical applications in the UV, ranging from lens components for photolithography<sup>1</sup> to beam delivery systems in medical instrumentation.<sup>2</sup> It is important to understand the radiolytic processes which lead to long-term alteration of the optical characteristics of this material. Several recent studies<sup>3-7</sup> have shown that the high peak power of pulsed UV lasers is frequently sufficient to induce various changes in the atomic arrangement of  $\alpha$ -SiO<sub>2</sub> by nonlinear optical processes. In particular, it has been found that point defects (as evidenced by color centers), similar to those created by ionizing radiation,<sup>8</sup> can be formed by excimer lasers operating at 193 and 248 nm.<sup>3,5-7</sup> The mechanism for formation of these color centers by low-quantum-energy radiation remains poorly understood. Here we report studies of the formation of color centers in bulk fused silica following prolonged irradiation at 193 nm. In addition we have found a stress-induced birefringence effect traced to radiolytic compaction of the solid.

Our study has emphasized high-water-content synthetic fused silica. Our own studies at 193 nm and previous studies<sup>5</sup> at 248 nm have shown these to be the least damage prone of the commercially available fused silicas. Commercially available samples ( $\sim 1000$  ppm OH) were irradiated with an ArF-excimer laser. The laser was typically operated with a collimated 0.8-cm-diam. beam at a pulse repetition rate of 100 Hz. The pulse duration was 23 ns. The samples were 2.5-cm-diam., 1.3-cm-thick polished discs. During irradiation the fused silica samples were kept in an enclosure which was continuously purged with dry N<sub>2</sub> in order to prevent surface reaction caused by organic contaminants and by the ozone generated in air. The absence of measurable surface effects was also confirmed by post-irradiation etchback of the surfaces of several samples.

The transmission of the samples at 193 nm, as well as any visible fluorescence, was monitored *in situ*. Following exposure, a UV transmission spectrum of the irradiated volume was recorded and corrected for reflective and absorptive losses using the unexposed areas of the same sample.

Two different permanent optical effects are observed. One is the appearance of absorption in the UV (see Figure 4-1) in the form of two bands, the more intense centered around 215 nm, and the weaker at  $\sim 260$  nm. The 215-nm band has been previously correlated with the E' defect which is a positively charged oxygen vacancy.<sup>9</sup> In addition to these absorptions, 193-nm irradiation creates a birefringent annular zone observed using 632.8-nm light, which extends from the edge of the laser spot several millimeters outward (see inset in Figure 4-1). As discussed below, this birefringence is attributed to mechanical stress<sup>10</sup> caused by irradiation-induced macroscopic volume changes. In agreement with theory<sup>11</sup> the transmitted light intensity when the sample is viewed between crossed polarizers is proportional to  $\sin^2(2\theta)$  where  $\theta$  is the angle between the in-plane projection of the optic axis and the direction of polarization of either polarizer. The magnitudes of the absorption and birefringence effects are strongly correlated. Both the 215-nm

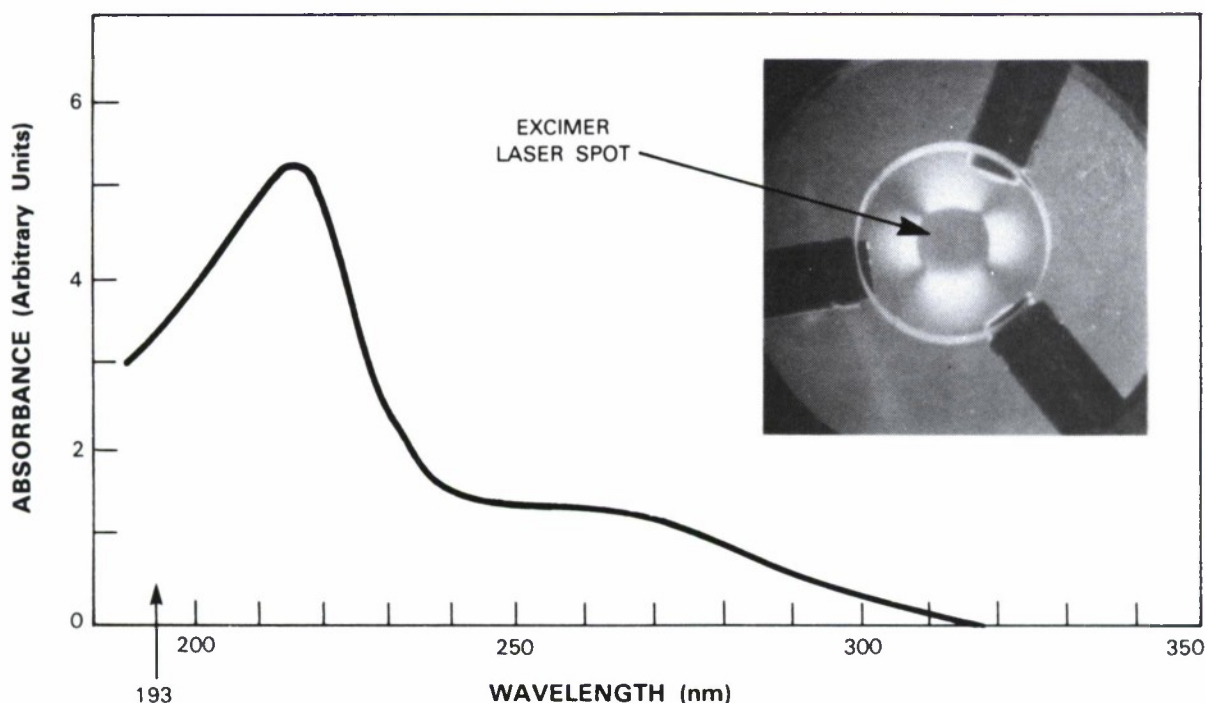


Figure 4-1. Absorption spectrum of high-OH fused silica, induced by pulsed irradiation at 193 nm. The spectrum has been corrected for reflective and absorptive losses in unexposed areas of the same sample. The inset shows the spatial distribution of transmitted 632.8-nm light when the fused silica sample was placed between two crossed linear polarizers. The nonzero transmission is caused by stress birefringence in an annular area surrounding the excimer laser spot.

absorption coefficient and the stress (which is proportional to the square root of the 633-nm transmission through crossed polarizers) increase quadratically with increasing fluence. For a fixed fluence, they increase linearly with the number of pulses (at least initially, see below). In addition, as shown in Figure 4-2, both show a qualitatively similar strong dependence on the sample temperature during irradiation (up to  $\sim 100^\circ\text{C}$ ).

Above  $\sim 100^\circ\text{C}$  the two curves in Figure 4-2 start diverging. The 215-nm peak is partially annealed at temperatures above  $100^\circ\text{C}$  and (not shown) is reduced to a level within  $\sim 2$  percent of its initial value at  $\sim 350^\circ\text{C}$ . On the other hand, the irradiation-induced birefringence shows no appreciable annealing to temperatures of  $\sim 150^\circ\text{C}$  and, in fact, retains more than 10 percent of its initial value even at temperatures above  $600^\circ\text{C}$ .

Furthermore, the two effects are additionally distinguished in their responses during post-formation photobleaching experiments. A typical result is illustrated in Figure 4-3. Here, a previously unirradiated sample was exposed to relatively high fluences ( $50 \text{ mJ cm}^{-2}/\text{pulse}$ ). Initially, the birefringence and the color center absorption increase linearly with the number of pulses, as mentioned above, and after  $\sim 10^6$  pulses they increase sublinearly, at approximately similar rates. The sample was then irradiated at lower fluence ( $12 \text{ mJ cm}^{-2}/\text{pulse}$ ). The birefringence remains unchanged, or increases slightly, whereas the 215-nm absorption is substantially bleached.

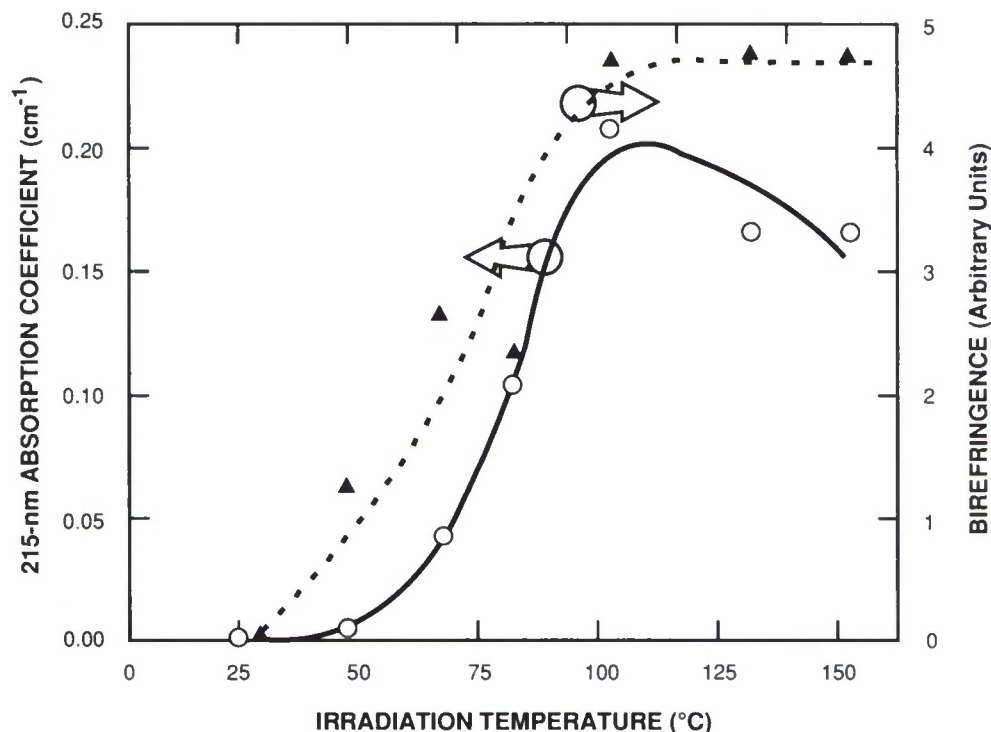


Figure 4-2. Variation of absorption coefficient at 215 nm ( $E'$  centers) and the stress birefringence (square root of induced 633-nm transmission) with sample temperature during 193-nm irradiation. The measurements were performed at room temperature. Exposure conditions were  $17 \text{ mJ cm}^{-2}/\text{pulse}$  and  $1.4 \times 10^6$  pulses at 100 Hz.

The nature of the birefringence-causing stress was determined by applying radially an external compressive stress to the sample. With this compensating external stress the irradiation-induced birefringence can be completely eliminated. We conclude that the unexposed areas are under tensile stress, apparently caused by radiation-induced compaction of the exposed volume.

Furthermore, the increase in the density of the exposed area is accompanied by a change in the index of refraction. This was shown when a fused silica prism was irradiated at 193 nm along its axis, while its index of refraction at 633 nm was continuously monitored at right angles to the excimer beam. A permanent increase in index of up to  $\sim 5 \times 10^{-5}$  was measured. This increase is related to the compaction and not to the color centers, as it remains unchanged even after partial ( $\sim 40$  percent) bleaching of the color centers. Note the behavior of the birefringence in Figure 4-3 which also remains unchanged upon bleaching. We conclude that there are two separate effects, both stemming from the same radiolytic process but ultimately represented by separate physical changes in the solid. The first resides as  $E'$ -center absorbers; the second is an unidentified matrix alteration leading to compaction and the index change.

The band gap of  $\text{a-SiO}_2$  is  $\sim 9 \text{ eV}$ , while the photon energy at 193 nm is 6.4 eV. Nevertheless, our work and several other recent studies,<sup>3,5-7</sup> clearly indicate that subband gap radiation can couple energy into fused silica and cause formation of point defects. The coupling mechanism



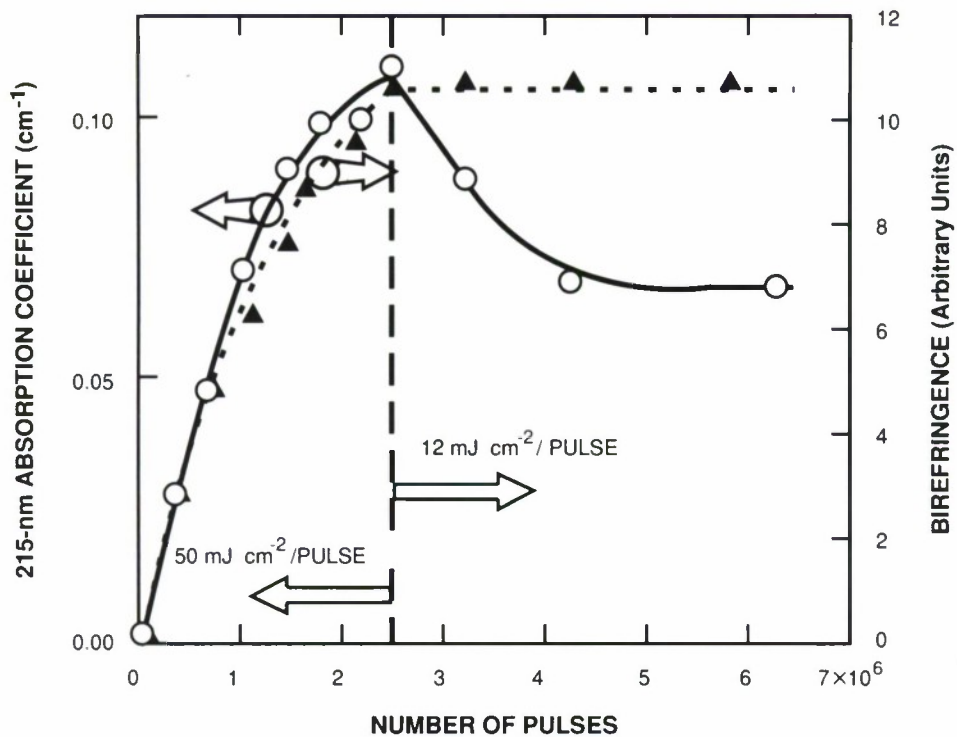


Figure 4-3. Effect of irradiation history on the 215-nm absorption coefficient and the 633-nm stress birefringence. Three regimes are noted: (i) a linear increase at high (50 mJ cm<sup>-2</sup>/pulse) fluence, up to  $\sim 10^6$  pulses; (ii) a sublinear increase at the high fluence for the next  $\sim 1.5 \times 10^6$  pulses; and (iii) partial bleaching but no change in birefringence upon reducing the fluence to 12 mJ cm<sup>-2</sup>/pulse.

is apparently a two-photon absorption process, as evidenced by the quadratic dependence on laser fluence. It has been suggested that the E' centers can be created by a radiolytic process involving nonradiative relaxation following two-photon creation of excitons.<sup>9</sup> Since the efficiency of nonradiative relaxation is expected to increase with increasing temperature, this model is also consistent with the temperature dependence of E' center formation in Figure 4-2. The fact that the degree of compaction increases in proportion with the density of E' centers indicates that the rate-limiting step for both is the nonradiative relaxation of excitons. A possible model was suggested in Reference 4 according to which compaction is related to rearrangement of strands of SiO<sub>4</sub> tetrahedra.

The two-photon absorption coefficient at 193 nm is (Reference 12)  $\sim 2 \times 10^{-3}$  cm/MW. Thus, the density of E' centers generated in one 23-ns pulse is  $\delta\rho_{E'} \approx 4 \times 10^{16} \eta \Phi^2$  cm<sup>-3</sup>, where  $\Phi$  is the fluence (J cm<sup>-2</sup>/pulse) and  $\eta$  is the efficiency of E'-center formation per pair of absorbed photons. Our optical data do not yield absolute values of  $\rho_{E'}$ , but rather with the aid of Smakula's formula,<sup>13</sup> the product  $(\delta\rho_{E'})\phi$  can be calculated where  $\phi$  is the oscillator strength of the 215-nm absorption band:  $(\delta\rho_{E'})\phi \approx 3 \times 10^{11} \Phi^2$  cm<sup>-3</sup>. Therefore, we deduce  $\eta\phi \approx 7.5 \times 10^{-6}$ . Comparison of our absorbance data with values of  $\rho_{E'}$  generated under similar experimental



conditions and measured with electron spin resonance techniques<sup>6</sup> yields  $\phi \approx 0.01$ . Hence  $\eta \approx 7.5 \times 10^{-4}$  for our stoichiometric, high-OH material. This value is considerably ( $\sim 3$  times) smaller than the value of  $\eta$  measured for oxygen-deficient, low-OH silica.<sup>7</sup> The degree of compaction, defined as the fractional change  $\delta\rho/\rho$  in the bulk density of fused silica, was also determined. Assuming accepted values for Young's modulus and the coefficient of birefringence at 633 nm,<sup>10</sup> we find that  $\delta\rho/\rho \approx 9 \times 10^{-23} \rho_{E'}$ . Since in our studies  $\rho_{E'}$  is as high as  $5 \times 10^{17} \text{ cm}^{-3}$ ,  $\delta\rho/\rho$  may exceed  $4 \times 10^{-5}$ . This value is also consistent with the observed changes in index of refraction.\* Note that the above relationship between  $\delta\rho$  and  $\rho_{E'}$  holds only as long as no thermal or photobleaching of the  $E'$  centers occurs. In the more general case  $\delta\rho/\rho$  can be expected to be higher than the value implied by  $\rho_{E'}$ , because it persists even when  $\rho_{E'}$  is reduced, as demonstrated in Figures 4-2 and 4-3.

The  $E'$  centers are apparently formed in a radiolytic process as mentioned above, and they are also removed in a photoinduced process. The removal step manifests itself as the sublinear behavior and the bleaching in Figure 4-3. The data in Figure 4-3 suggest that the removal is caused by one-photon absorption at 193 nm, and that its rate is proportional to the density  $\rho_{E'}$ . The rate of bleaching and, independently, the asymptotic value of the 215-nm absorbance, can be used to determine an efficiency of bleaching,  $\eta'$ , per absorbed photon. From our data we find  $\eta' \approx 10^{-6}$ . The fact that bleaching is at all possible suggests that the upper state of the electronic transition of the  $E'$  center is embedded in the continuum of conduction states. The low value of  $\eta'$ , on the other hand, indicates that the matrix elements coupling this upper state with the continuum are small.<sup>14</sup> The exact nature of the bleaching effect is still unclear. In particular, it remains to be determined whether bleaching transforms  $E'$  centers into another defect or whether it restores the original perfect network arrangement.

In conclusion, 193-nm irradiation of high-OH fused silica causes formation of  $E'$  centers and macroscopic volume changes (compaction) via two-photon absorption and exciton relaxation. Neither effect anneals at room temperature for over a year. The compaction is accompanied by birefringence and changes in index of refraction, and the  $E'$  center formation by absorption in the UV. We have shown, by varying substrate temperature during irradiation, that the efficiency of formation of  $E'$  centers can be controlled, apparently by controlling the lifetime of the excitons. Photobleaching at 193 nm was also demonstrated. These results have direct implications on the design and mode of operation of optical components intended to be used in the deep UV.

M. Rothschild  
T.J. Pack  
D.J. Ehrlich  
L.J. Belanger

---

\* The index of refraction of fused silica depends on the total volume change as well as on the change in the partial volume occupied by the oxygen ions. The relative contributions of the two causes vary with the nature of the process that induces the changes (see Reference 10). Our results indicate that in laser-induced compaction the major contribution is that of an overall volume change.

## 4.2 FABRICATION OF REGROWTH FIELD EFFECT TRANSISTOR TEST STRUCTURES BY ELECTRON BEAM LITHOGRAPHY

The critical process step during the fabrication of regrowth field effect transistors (RFETs) is the growth of high-quality GaAs through a pattern of submicrometer lines that act as the gates of the transistor. The crystal quality of the overgrown layer depends on the orientation of the lines relative to the crystalline orientation of the GaAs substrate. Normally, the grating for the gate is exposed using x-ray lithography. The holographically produced x-ray mask has a large area grating with a single orientation and line-space ratio. We have designed a "fan" test structure which allows characterization of overgrowth for many different line orientations in a single growth step. Because of its ability to pattern submicrometer features at any angle, a JEOL JBX-5DII electron beam lithography system was used as the patterning tool, and patterns were formed by writing directly on the substrate, bypassing the x-ray lithography step.

Figure 4-4 shows a schematic of the "fan" structure, which consists of sets of five lines spaced 450 nm apart, arrayed at 3 deg intervals. To simulate currently used RFET gratings as closely as possible, the exposed lines of the gratings were designed to be  $270 \pm 20$  nm wide after development. The structures are large ( $3 \times 6$  mm) to allow cleaving after overgrowth.

The grating fabrication is shown in Figure 4-5. A multilayer structure [Figure 4-5(a)] is formed on a p-type GaAs substrate by first CVD depositing a 280-nm-thick  $\text{SiO}_2$  layer, then electron beam evaporating 70 nm of tungsten, followed by CVD deposition of an additional 230 nm of  $\text{SiO}_2$ . After being patterned, the three layers will form the gate structure which will then be overgrown with GaAs. A 200 nm polymethyl methacrylate (PMMA) layer is spun on as the electron beam resist. The pattern was written in the PMMA layer with a 25 kV electron beam and wet-developed in a mixture of 40 percent methylisobutylketone and 60 percent isopropanol. As shown in Figure 4-5(b), a 50-nm layer of pure nickel is then e-beam evaporated over the entire surface. A liftoff with an acetone solvent is performed [Figure 4-5(c)], leaving behind a nickel pattern which acts as a reactive ion etch mask. After the sample is cleaned in organic solvents and in a helium-oxygen plasma, it is etched at 250 W in a  $\text{CF}_4$  plasma [Figure 4-5(d)], which etches away the unprotected layers in just over 95 min. Clear channels to the substrate (which acts as the seed crystal) through which GaAs can be grown are the result.

The electron beam patterning was the most difficult step to perfect. Initial attempts to pattern the PMMA used single passes of a 250-nm electron beam within a  $1500\text{-}\mu\text{m}$ -square writing field. Because the pattern was larger than  $1500\text{ }\mu\text{m}$ , eight separate writing fields were stitched together by moving the stage after each field was written. This introduced discontinuities in the pattern, but since all the lines have unbroken stretches at least  $1500\text{ }\mu\text{m}$  long such imperfections were not considered significant. Unfortunately, astigmatism in the electron beam could not be entirely eliminated, and an approximately ellipsoidal spot was the result. Figure 4-6 shows how an astigmatic beam produces lines of different widths at different angles. The design goal of  $270 \pm 20$  nm could not be met, and in some cases lines at certain angles were not clearly resolved.

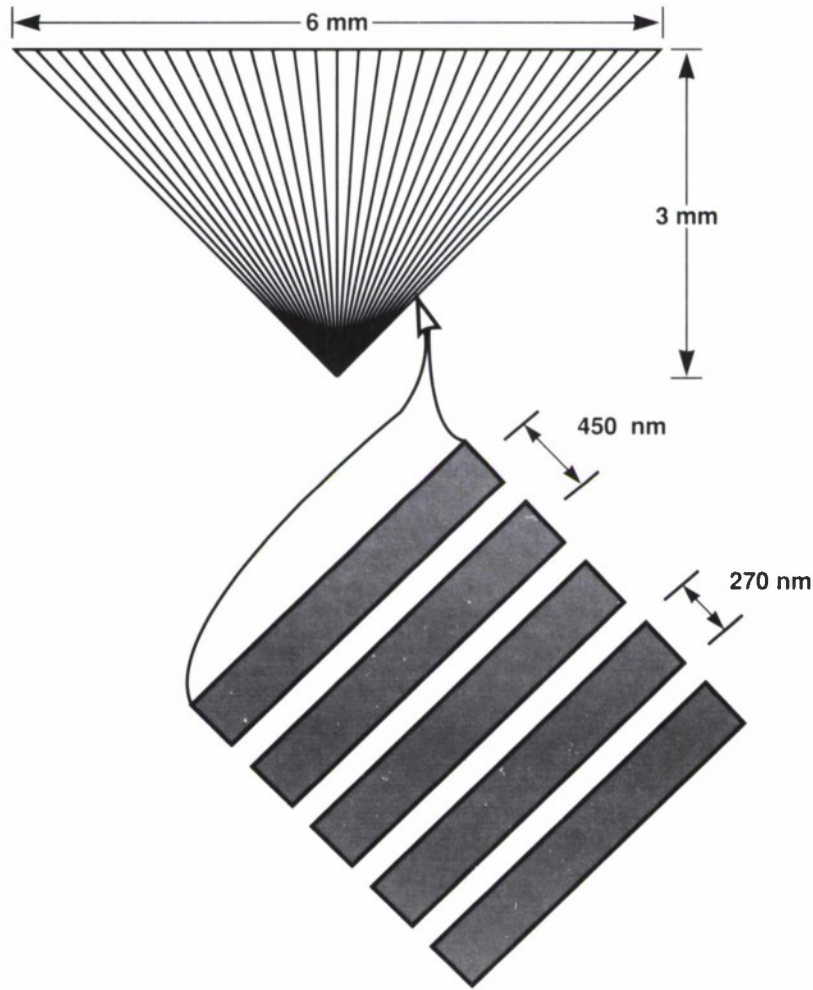


Figure 4-4. Layout of the "fan" test pattern. The details of each radial line cluster are shown in the inset.

The importance of beam stigmatism was reduced by using a 40-nm spot in place of the 250-nm spot and by tracing the features with multiple passes of the beam. Linewidth control improved dramatically, as did the resist profiles which are critical for successful liftoff. Unfortunately, electron beam size and the size of the writing field are connected. While the original 250-nm beam could be used in a 1500- $\mu\text{m}$ -square field, the 40-nm beam could only be used with a 150- $\mu\text{m}$ -square field. As a result, the number of stage steps, and therefore the number of discontinuities in the pattern rose by a factor of 100.

With the potential for breaks every 150  $\mu\text{m}$ , the magnitude of such breaks had to be minimized. Figure 4-7(a) shows a field-stitching discontinuity obtained with the 40-nm spot and a 150- $\mu\text{m}$  field of view. The lines at the top of the micrograph are separated from those in the bottom by 70 nm, and they are misaligned by 50 nm. Note the poor quality of the resist pattern in



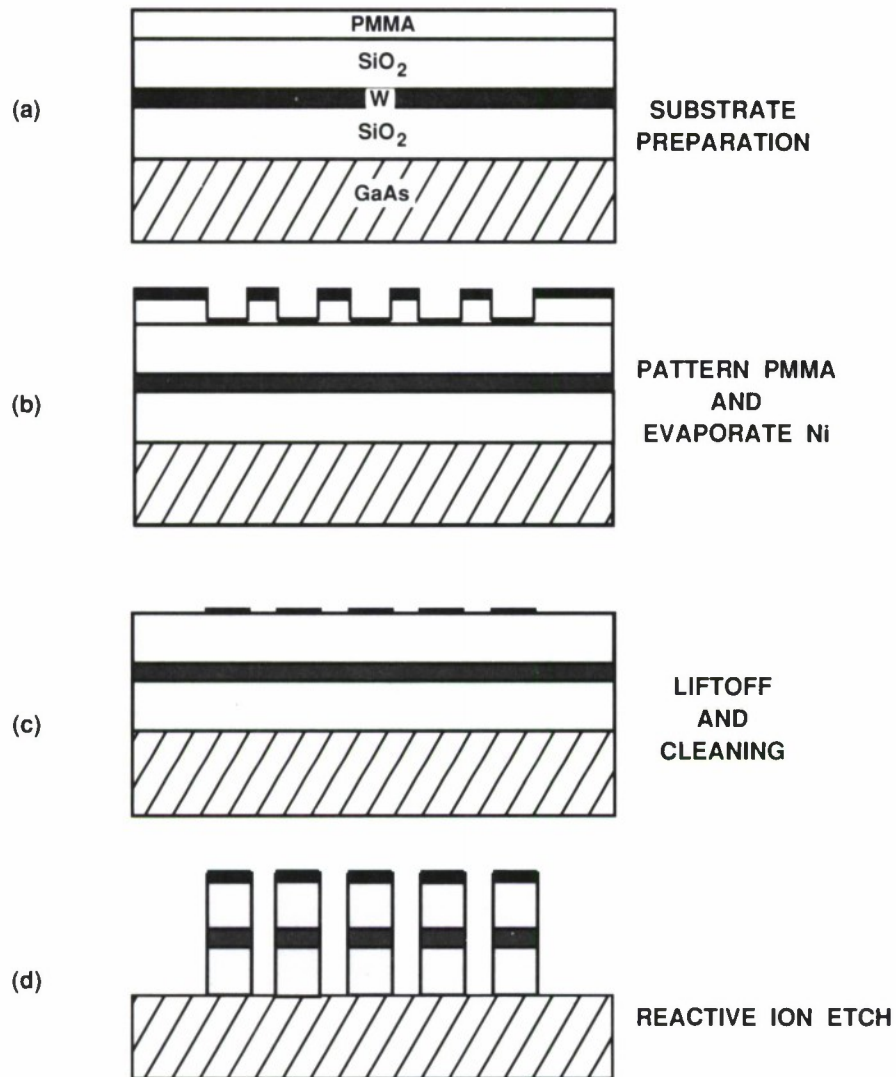


Figure 4-5. Cross-sectional views illustrating the process for making RFET gratings: (a) initial multilayer stack, (b) after e-beam patterning and nickel evaporation, (c) after liftoff, and (d) after reactive-ion etching.



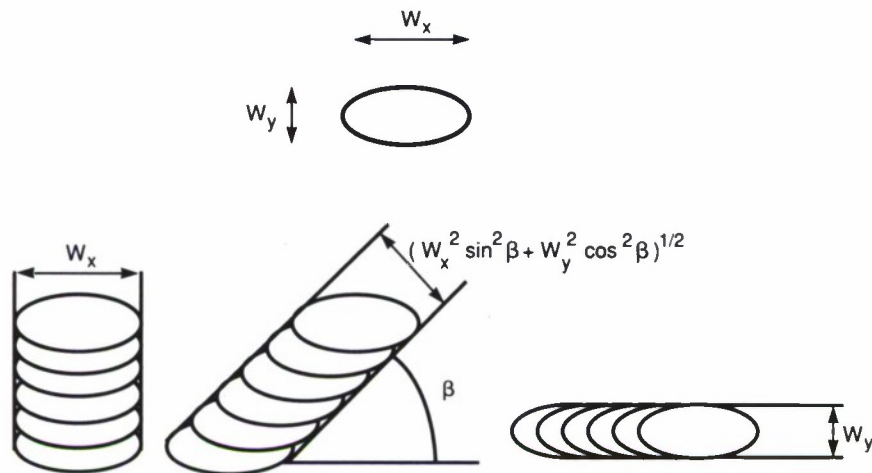


Figure 4-6. Effect of an astigmatic (ellipsoidal) spot on the linewidth produced when an electron beam is scanned at different angles. In addition to the purely geometric effect illustrated here, the dose per unit area is changed, affecting the developed width of the line.

the lower half of the photo, indicating that the beam was defocused at its maximum deflection. To improve on these results, the writing field was further reduced from 150  $\mu\text{m}$  to 100  $\mu\text{m}$ . Figure 4-7(b) shows the marked improvement, both in positioning and in image quality. The overlap error is reduced to about 40 nm while the line placement errors are under 25 nm.

Additional improvements were made by using different electron doses for each of the five lines. Figure 4-8 shows the resulting fully optimized structure after the nickel liftoff step. Note that the over/underlap error has been eliminated and that the stitching errors are all less than 10 nm. These structures are now being used in overgrowth experiments and are proving helpful in optimizing growth parameters.

C.L. Dennis  
T.M. Lyszczarz  
K.B. Nichols

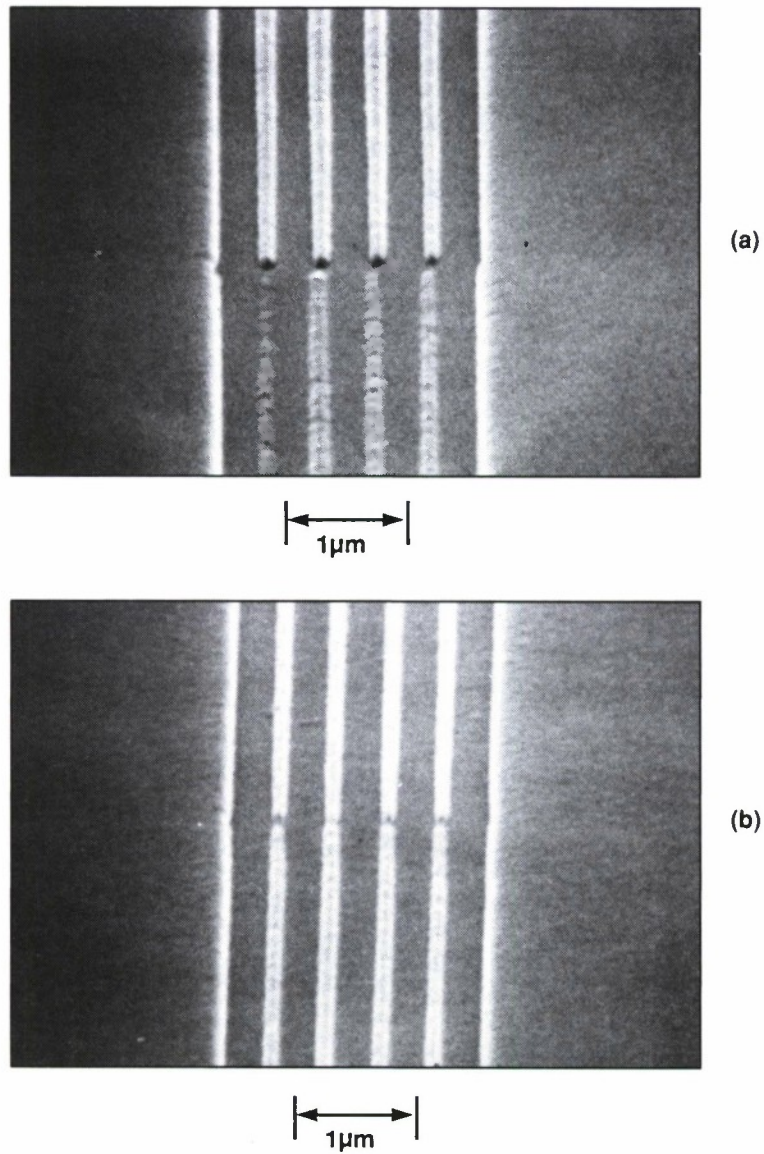
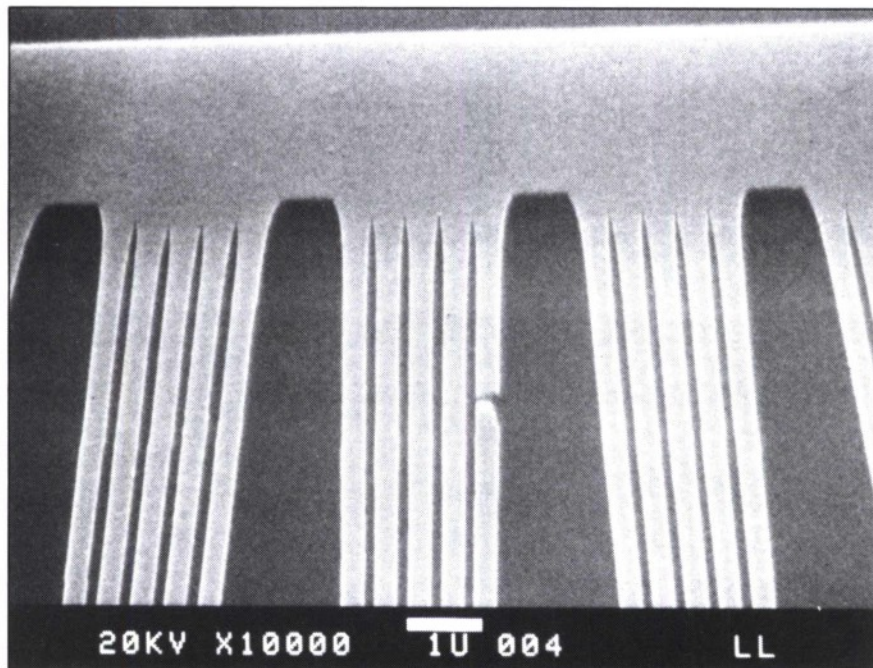


Figure 4-7. Effect of field size on the stitching accuracy and lithographic quality of exposed features: (a) 150-μm field and (b) 100-μm field.



*Figure 4-8. Nickel pattern produced by liftoff after electron beam exposure, showing the quality of stitching at a field boundary.*

## REFERENCES

1. M. Rothschild and D.J. Ehrlich, J. Vac. Sci. Technol. B **6**, 1 (1988).
2. R.S. Taylor, K.E. Leopold, R.K. Brimacombe, and S. Mihailov, Appl. Opt. **27**, 3124 (1988).
3. R.A.B. Devine, C. Fiori, and J. Robertson, in *Materials Research Society Symposia Proceedings, Vol. 61* (Materials Research Society, Pittsburgh, Pennsylvania, 1986), p. 177.
4. C. Fiori and R.A.B. Devine, Phys. Rev. B **33**, 2972 (1986).
5. G.C. Escher, Proc. SPIE **998**, 30 (1988).
6. T.E. Tsai, D.L. Griscom, and E.J. Friebele, Phys. Rev. Lett. **61**, 444 (1988).
7. K. Arai, H. Imai, H. Hosono, Y. Abe, and H. Imagawa, Appl. Phys. Lett. **53**, 1891 (1988).
8. D.L. Griscom, Nucl. Instrum. Methods Phys. Res. B **1**, 481 (1984).
9. D.L. Griscom, Proc. SPIE **541**, 38 (1985).
10. W. Primak and D. Post, J. Appl. Phys. **30**, 779 (1959).
11. See, for example, H.T. Jessop and F.C. Harris, *Photoelasticity* (Dover, New York, 1960).
12. R.S. Taylor, K.E. Leopold, and R.K. Brimacombe, in *Lasers and Electro-Optics Society Annual Meeting Conference Proceedings, 2-4 November 1988* (IEEE, New York, NY, 1988), p. 228.
13. D.L. Dexter, Solid State Phys. **6**, 353 (1958).
14. See also A.H. Edwards, in *Materials Research Society Symposia Proceedings, Vol. 61* (Materials Research Society, Pittsburgh, Pennsylvania, 1986), p. 3.



## 5. MICROELECTRONICS

### 5.1 RESONANT-TUNNELING OSCILLATORS UP TO 420 GHz

We have recently obtained the highest oscillation frequencies to date in resonant-tunneling diodes, and have found the results to be consistent with a new impedance model of the device. The experimental results shown in Figure 5-1 were obtained with a diode consisting of two 1.1-nm-thick undoped AlAs barriers separated by a 4.5-nm-thick undoped GaAs quantum well. The doping profile outside of the double-barrier region is given in Figure 5-2. The profile on the cathode side is intended to achieve as high an electron concentration as possible without contaminating the tunneling region with ionized donors. Previous experience has shown that donor concentrations exceeding  $N_D \cong 1 \times 10^{18} \text{ cm}^{-3}$  degrade the peak-to-valley ratio significantly when deposited adjacent to the first heterojunction. A donor concentration of  $N_D = 2 \times 10^{17} \text{ cm}^{-3}$  is used over the first 100 nm on the anode side of the structure. Most of this region is depleted at the bias voltage for peak resonant-tunneling current.

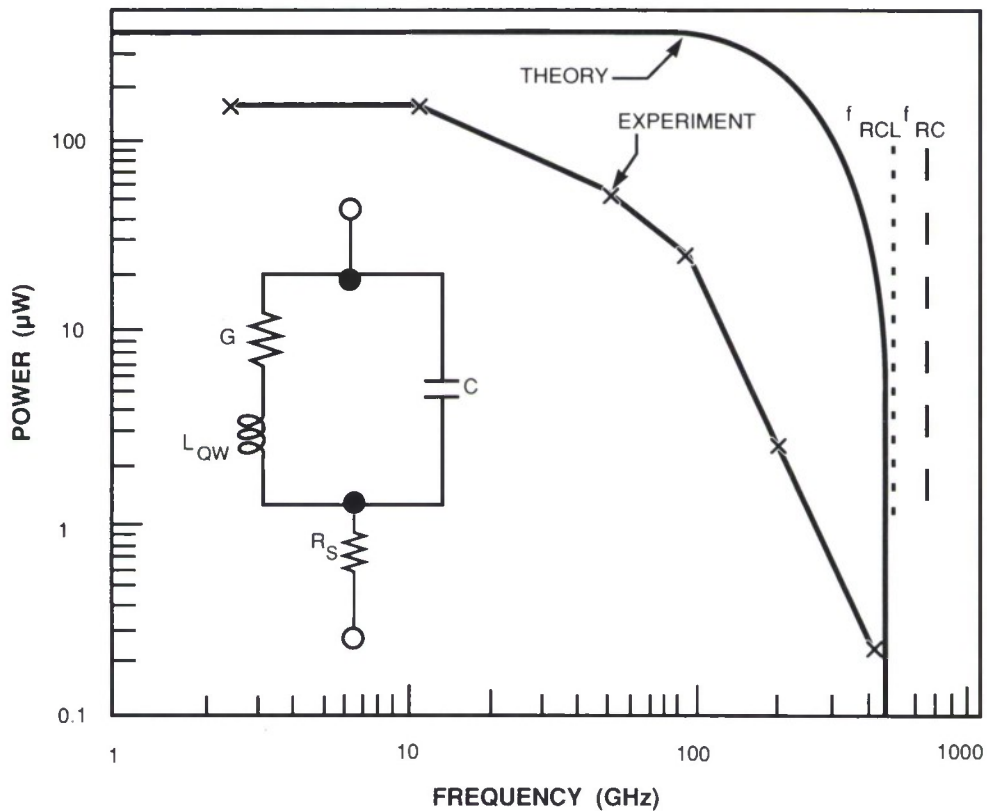


Figure 5-1. Experimental and theoretical power for a 4- $\mu\text{m}$ -diameter diode. The quantities  $f_{RCL}$  and  $f_{RC}$  are maximum oscillation frequencies calculated from the equivalent circuit shown in the inset. This circuit includes the differential conductance  $G$ , the diode capacitance  $C$ , the quantum-well inductance  $L_{QW}$ , and the series resistance  $R_S$ .

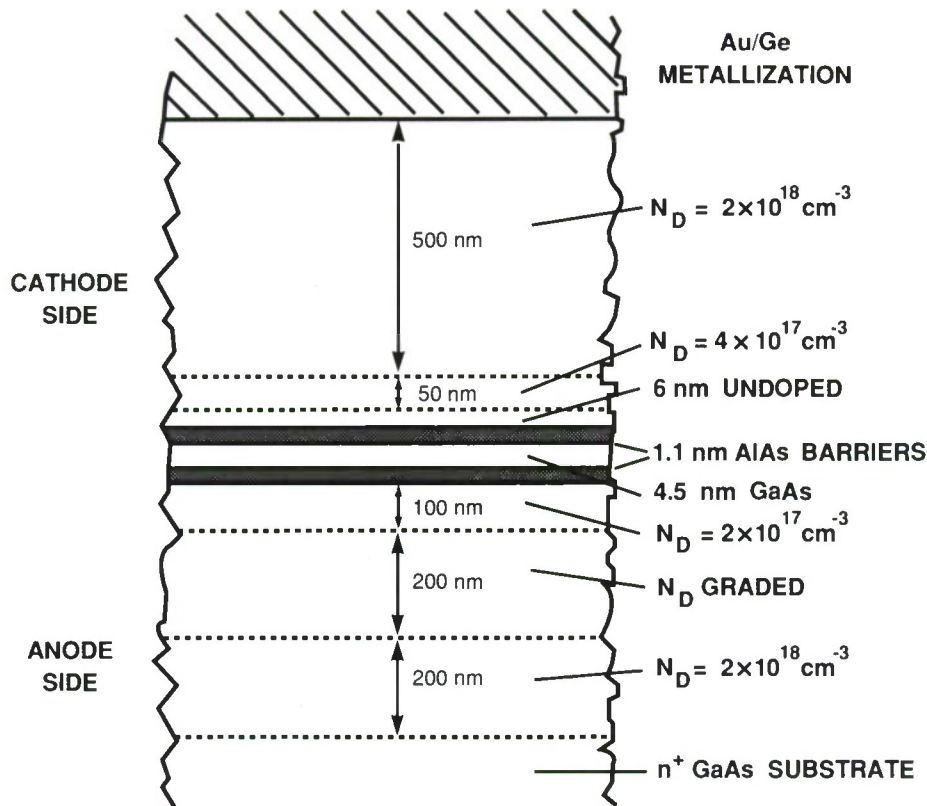


Figure 5-2. Cross-sectional schematic view of the GaAs/AlAs wafer used to fabricate diodes that oscillated up to 420 GHz.

The I-V curve for a 4- $\mu\text{m}$ -diam. device is shown in Figure 5-3. The peak current density of this device,  $J_p = 1.5 \times 10^5 \text{ A cm}^{-2}$ , is much greater than that of a previous device<sup>1</sup> which oscillated up to 200 GHz,  $J_p = 4 \times 10^4 \text{ A cm}^{-2}$ . However, the peak-to-valley ratio is lower for reasons that are not yet understood. The wafer was diced into very small ( $\sim 100 \times 100 \mu\text{m}$ ) chips that were mounted into a series of resonators covering the frequency range from about 2 GHz to over 400 GHz. Both the power and frequency of the oscillations from the highest frequency (WR-2 waveguide) resonator were determined by feeding the radiation out of the waveguide into free space, and then transmitting the radiation through a Fabry-Perot cavity and into a liquid-helium-cooled composite bolometer. The highest observed frequency of oscillation was 420 GHz, and the power at this frequency was about 0.2  $\mu\text{W}$ . It should be mentioned that this was an exceptional result. All of the other devices tested in the WR-2 cavity either oscillated in the range 310 to 370 GHz or did not oscillate at all. We attribute the 420 GHz result to an unusually low ohmic contact resistance, which can occur in highly localized spots for alloyed Ni/Ge/Au contacts.

The theoretical oscillation power shown in Figure 5-1 was derived by a large-signal analysis of the equivalent circuit shown in the inset. This circuit includes the differential conductance  $G$ ,

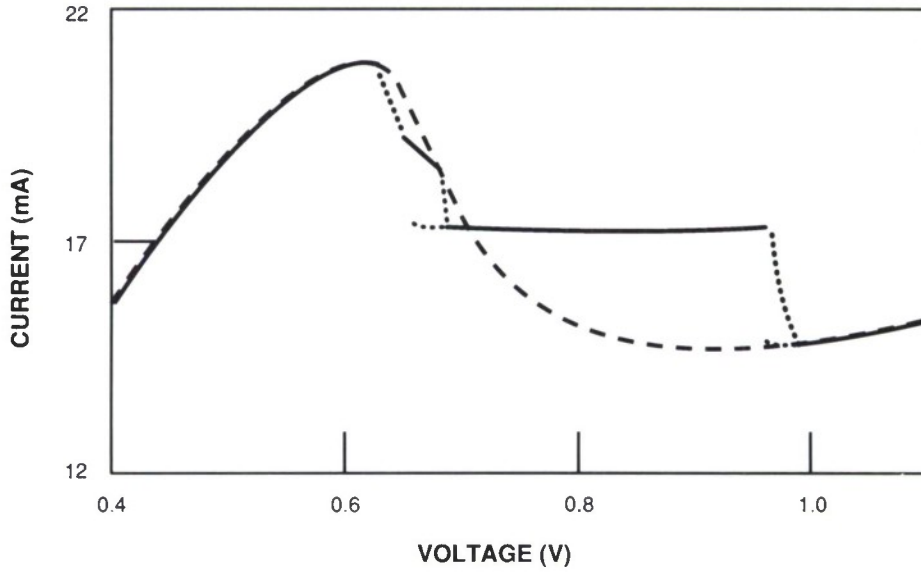


Figure 5-3. Experimental current-voltage curve (solid and dotted) and the theoretical curve (dashed) for a representative 4- $\mu\text{m}$ -diam. diode at room temperature. The chair-like structure of the experimental curve is caused by self-detection of oscillations.

the diode capacitance  $C$ , the frequency-dependent series resistance  $R_S$ , and a new element  $L_{QW}$  called the “quantum-well inductance.” Physically, this inductance represents a temporal delay of conduction current with respect to ac voltage, an effect that is intrinsic to coherent resonant-tunneling. Near the center of the negative differential conductance region, it can be shown that  $L_{QW} \cong \tau_1/G$  where  $\tau_1$  is the quasibound ground-state lifetime.<sup>2</sup> Using this circuit, we find the theoretical oscillation power for the present device approaches zero at the frequency  $f_{RCL} = 476$  GHz. For comparison we also show the corresponding frequency  $f_{RC} = 670$  GHz that would apply in the absence of quantum-well inductance (i.e., in the limit  $\tau_1 = 0$ ). These two frequencies are maxima with respect to all values of  $G$  that occur in the negative differential conductance region of the stable (i.e., not oscillating) I-V curve in Figure 5-3. In the present structure both frequency maxima occur at the most negative value of  $G$ , which is  $-58$  mS at a bias voltage of 0.67 V. The capacitance used in this calculation was obtained from the numerical solution to the Poisson equation. The result at 0.7 V is  $C = 18.5$  fF.  $L_{QW}$  is calculated using a  $G$  obtained from the stable I-V curve and a  $\tau_1$  obtained from  $\tau_1 = \hbar/\Gamma_1$ , where  $\Gamma_1$  is full width at half-maximum of the transmission probability  $T^*T$  function. The result for the 1.1-nm-thick AlAs barriers is  $\tau_1 = 0.11$  ps. Finally,  $R_S$  was calculated to be  $4 \Omega$  at dc and about  $6 \Omega$  at 600 GHz. This assumes an ohmic contact resistance of  $R_C = 1 \times 10^{-7} \Omega \text{ cm}^2$ , a low value that is consistent with measurements of the best ohmic contacts using our current technology.

A change in the present device structure that would definitely increase the speed is a reduction in the series resistance. For example, a frequency-independent  $R_S$  of  $2 \Omega$  would increase  $f_{RCL}$  to about 1.1 THz for  $G = G_{MAX} = -58$  mS. This value of resistance is obtained by including

only ohmic-contact and undepleted-epilayer contributions, and neglecting all spreading resistance effects. It might be realized in the GaAs material system with a planar, interdigitated-contact geometry that separates the cathode and anode ohmic contacts by a few micrometers at most. Another possible way to enhance the speed would be to decrease  $\tau_1$  by thinning the barriers. Of course, this enhancement can occur only if the peak-to-valley ratio remains high enough so that the I-V curve provides the required magnitude of negative conductance. To quantify this, we have calculated  $f_{\text{RCL}}$  as a function of  $G$  assuming  $\tau_1 = 0.05$  ps, which is the theoretical value for 0.85-nm-thick (3 atomic layers) AlAs barriers. The result is  $f_{\text{RCL}} \cong 1.4$  THz for  $G = -98$  mS. Obviously, such a high magnitude of conductance is not realizable in the present structure, and would probably not ensue from a thinning of the AlAs barriers. However, it would be quite possible in the  $\text{In}_{0.53}\text{Ga}_{0.47}\text{As}/\text{AlAs}$  material system which has recently yielded a room-temperature peak-to-valley ratio of 23:1 and peak-current density of  $3.2 \times 10^4$  A cm<sup>-2</sup> for 2.5-nm-thick AlAs barriers.<sup>3</sup> The  $\Gamma$ -point conduction band offset between AlAs and  $\text{In}_{0.53}\text{Ga}_{0.47}\text{As}$ , including the effect of lattice mismatch, is only about 20 percent higher than the offset between AlAs and GaAs. Thus, identical atomic-layer-values of the barrier and well thickness should yield roughly the same  $\tau_1$  in the two material systems. Furthermore, it is expected that the InGaAs system should facilitate the proposed decrease in  $R_S$  because it promises much lower values of specific-contact resistance and undepleted-epilayer resistivity than presently exist in GaAs.

E.R. Brown	W.D. Goodhue
T.C.L.G. Sollner	C.L. Chen
C.D. Parker	

## 5.2 OBSERVATION OF OPTICALLY PUMPED INTERSUBBAND EMISSION FROM QUANTUM WELLS

There is growing interest in new devices based on confined states in quantum wells. Optical transitions between subbands are of special interest because they can be tuned over most of the far- and mid-infrared spectrum. Spontaneous emission from transitions between subbands in isolated quantum wells has been observed by Helm et al.<sup>4</sup> by electrically heating the electrons. We report here the first observation of radiative intersubband transitions by optically excited carriers in a quantum-well structure.

Our work utilizes the subband splitting inherent in coupled quantum wells (CQW). In a symmetric coupled-well system, each state of the uncoupled well is split into two subbands, a symmetric subband and an antisymmetric subband, the latter with slightly higher energy. Intersubband transitions only occur between subbands of opposite parity and only for light polarized with the electric field parallel to the direction of confinement.

Our n-type GaAs/AlGaAs CQW structure is similar to that presented previously.<sup>5</sup> The GaAs quantum wells are approximately 8.5 nm thick, and the center AlGaAs coupling barriers are approximately 2.2 nm thick. Barriers of 30-nm thickness separate the 30 CQWs. These dimensions have been confirmed by transmission electron microscopy. From Auger analysis, the aluminum fraction of all barriers is about 50 percent. The major change from the previous structure



is that the doping is limited to a sheet of Si in each confining barrier 2.0 nm from the interface with the quantum well. Hall measurements at 77 K show an electron sheet density of  $1.1 \times 10^{12} \text{ cm}^{-2}$  in each coupled well and a mobility of  $2.7 \times 10^4 \text{ cm}^2/\text{V-s}$ .

We have calculated energy levels, wave functions, and transition probabilities for this structure. There are four conduction subbands, which we will designate (in order of increasing energy)  $E_1$ ,  $E_2$ ,  $E_3$ , and  $E_4$ . Calculated energies for the  $E_1$ - $E_4$  and  $E_2$ - $E_3$  transitions are 128 and 11 meV, respectively. The  $E_4$ - $E_3$  transition is predicted to occur at 14 meV.

To obtain information on the relative positions of the energy levels, the intersubband transitions in the conduction band of this CQW sample have been studied in the mid-infrared (2 to 25  $\mu\text{m}$ ) using a Fourier-transform spectrometer. The transmittance spectrum of Figure 5-4 was taken with the sample cooled to about 25 K. The spectrum shows two absorptions, one at 132 meV, the other at 119 meV. These absorptions are identified with the allowed transitions,  $E_1$ - $E_4$  and  $E_2$ - $E_3$ , respectively. Each absorption is approximately 10 meV wide. These linewidths are believed to be dominated by fluctuations in the quantum well widths and the width of the

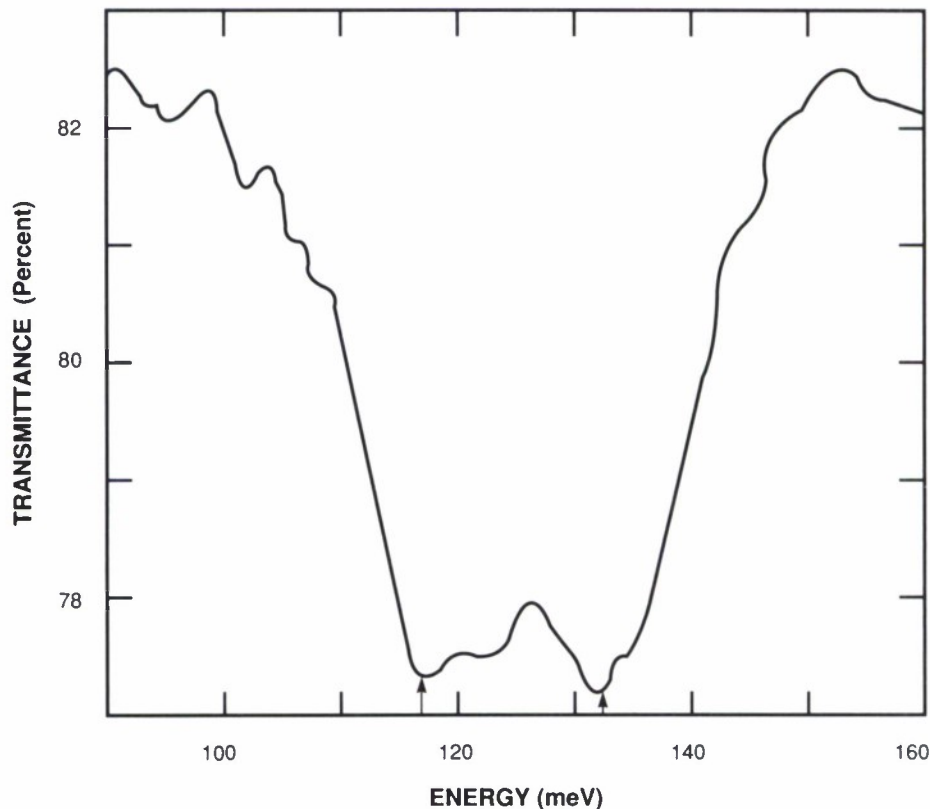


Figure 5-4. Transmission spectrum for coupled quantum wells at 25 K. Measurement was made with p-polarized light incident at Brewster's angle. The higher energy absorption is identified as the  $E_1$ - $E_4$  transition, the lower as the  $E_2$ - $E_3$  transition. The arrows mark the two energies used to pump the sample for far-infrared emission.

thin coupling barrier. The discrepancies between theory and experiment can be attributed to band-bending due to charge in the structure. Since there is a net negative charge in the quantum wells (due to modulation doping), the Coulomb interaction is expected to shift the energy levels and, to a lesser degree, the transition energies. We are presently modifying our model to include these effects.

Far-infrared emission measurements were made with the sample attached to a copper cold finger by indium solder. The cold finger was cooled to 20 K by a closed-cycle helium refrigerator, but the sample temperature is expected to be somewhat higher when optically excited. The geometry of Figure 5-5 allowed us to illuminate the sample with radiation polarized parallel to the direction of confinement. We pumped electrons from the  $E_1$  subband into the  $E_4$  subband with a CW  $\text{CO}_2$  laser focused to a  $100\text{-}\mu\text{m}$ -diam. spot on one cleaved face at a corner of the sample. The far-infrared radiation emitted from the other cleaved face of that corner of the sample was collected and analyzed with a Fourier-transform spectrometer. The radiation was detected with a gallium-doped germanium photoconductor cooled to 4.2 K. The spectral wavelength range of the system is 50 to  $120\text{ }\mu\text{m}$  (photon energy 25 to 10 meV). The pump laser was chopped at approximately 200 Hz and the signal measured with a lock-in amplifier.

The emission spectrum shown in Figure 5-6 was obtained while the sample was illuminated with a power of approximately 6 W from the  $\text{CO}_2$  laser operated at a wavelength of  $9.34\text{ }\mu\text{m}$  (133 meV photon energy), near the peak of the  $E_1$ - $E_4$  transition. The data were taken with a spectral resolution of 0.3 meV. The 3-meV-wide peak at 17 meV is attributed to spontaneous

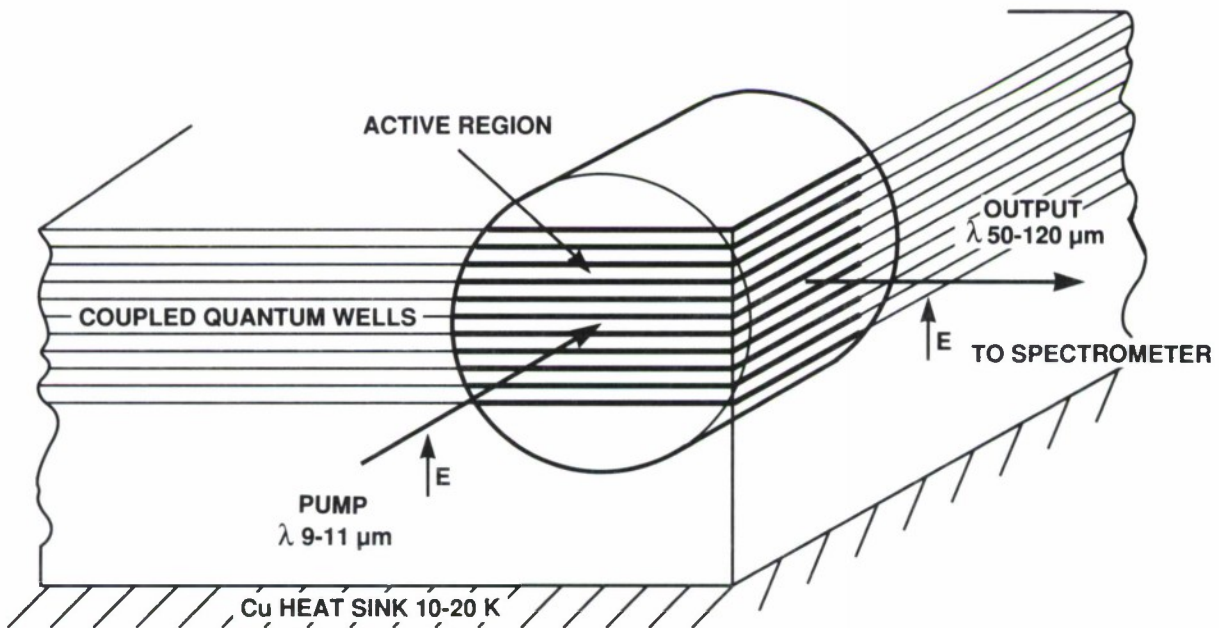


Figure 5-5. Pump and emission geometry for measuring far-infrared emission.

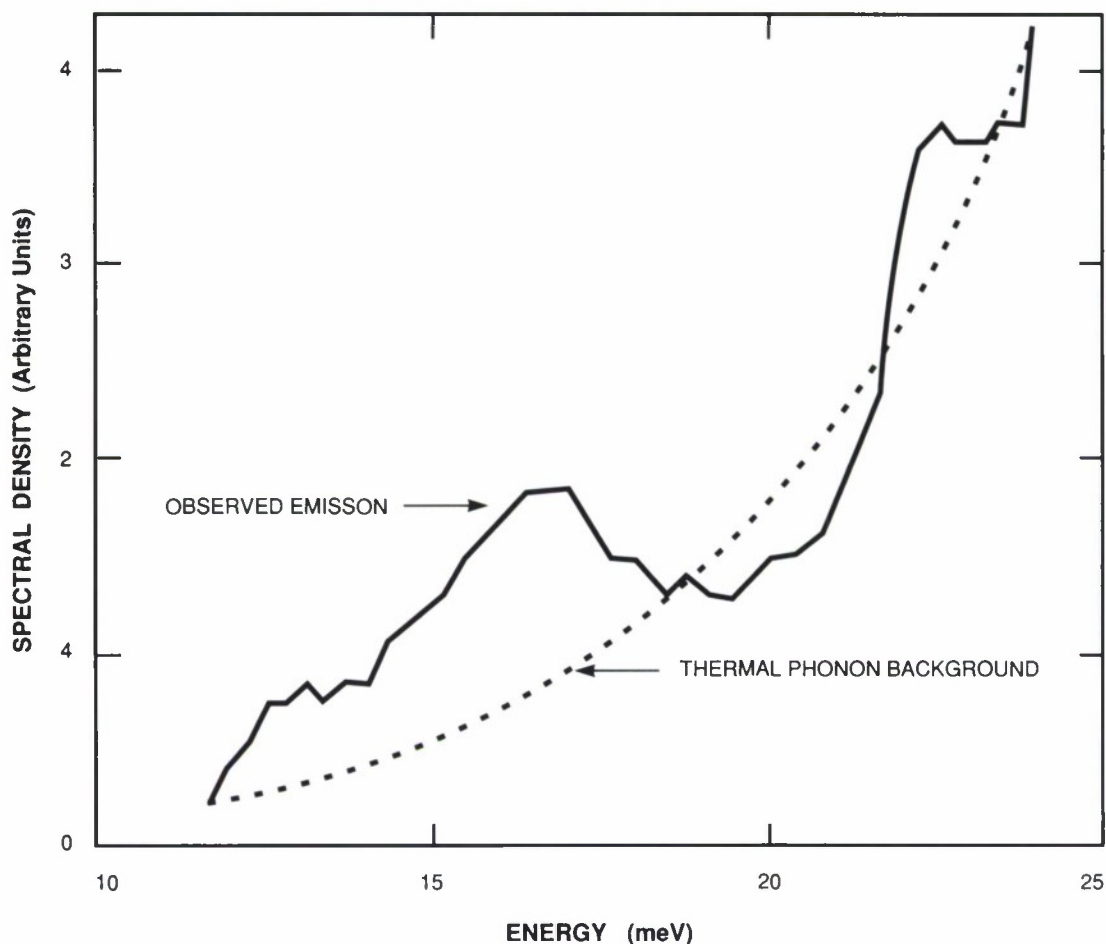


Figure 5-6. Far-infrared emission by coupled quantum wells. The peak at 17 meV is attributed to the  $E_4$ - $E_3$  transition. The dashed line is the calculated radiation from  $Al_{0.27}Ga_{0.73}As$  at 100 K.

emission by electron transitions from the  $E_4$  subband to the  $E_3$  subband, which was calculated to occur at 20 meV. Calculations indicate that the low energy shoulder at 12.5 meV may be radiation from a region of the sample where the coupling barrier is one monolayer thicker. There is also a sharply rising feature at higher energy that we attribute to hot phonon emission as discussed below. As expected, no peak at 17 meV was observed when the pump wavelength was changed to  $10.6 \mu m$  (117 meV photon energy), corresponding to the  $E_2$ - $E_3$  transition, but the higher energy component of the spectrum remained.

The emissivity of GaAs and AlGaAs increases sharply for photon energies approaching the TO phonon modes. The dashed curve on Figure 5-6 is the computed spectral density emitted by a  $100\text{-}\mu m$ -thick slab of  $Al_{0.27}Ga_{0.73}As$  at 100 K (TO phonon energy 33.33 meV). Given the high pump power and the strength of the intersubband absorption, it is reasonable to expect that the active region of the sample would be heated to this degree. The close agreement with the spectrum leads us to believe that the high energy feature is due to radiation from GaAs and

$\text{Al}_{0.27}\text{Ga}_{0.73}\text{As}$  layers in the active region heated by nonradiative relaxation of excited carriers in the quantum wells.

In summary, we have reported the first observation of radiative transitions by optically excited carriers between subbands of a quantum-well structure. The source of excitation was a CW  $\text{CO}_2$  laser operated at a photon energy of 133 meV. The emission has an energy of 17 meV and a full width at half-maximum of 3 meV.

J.W. Bales	W.D. Goodhue
K.A. McIntosh	E.R. Brown
T.C.L.G. Sollner	

### 5.3 CASTING PROCESS FOR MULTICHIP INTERCONNECTS

Multichip integration is an advanced hybrid technology that is being developed to combine the advantages of conventional hybrid and monolithic circuits. The technique can be used to integrate VLSI circuits with optoelectronic devices that are fabricated of different materials and, because thin-film interconnection is used between chips without wire bonds, there is a promise of performance previously achievable only in a monolithic chip technology

The individual chips are embedded in an epoxy casting, which is cured at room temperature. The resulting assembly can be processed through device interconnect or circuit metallization levels as a monolithic wafer. The accurate location and planarization of these chips in the epoxy is accomplished with the technique shown in Figure 5-7. The chips are placed face up in a custom-formed, reusable RTV rubber mold as shown in Figure 5-7(a). The loaded mold is pressed against an adhesive film, then peeled away leaving all the chips in the correct position for photolithography as in Figure 5-7(b). A glass or rubber frame is positioned around the set chips to define the required outside perimeter of the multichip assembly. The epoxy is then poured into the mold as indicated in Figure 5-7(c). When the epoxy is fully cured the frame is removed and adhesive is peeled from the assembly. Next, either a liftoff or a plating technique is used to produce the interconnects on the multichip assembly as indicated in Figure 5-7(d).

An optoelectronic receiver which consists of a photodiode and an FET amplifier has been fabricated using this multichip technique. As seen in Figure 5-8(a), an InGaAs PIN diode chip and a GaAs MESFET chip are cast in the epoxy. The diode and MESFET are connected by the metallized circuit which includes impedance-matching and bias networks. No bond wire is needed to connect the two semiconductor chips and the entire assembly is treated like a single monolithic circuit substrate.

In preliminary experiments the PIN diode has been illuminated by a laser amplitude-modulated at 2 GHz, as diagramed in Figure 5-8(b). The measured waveform at the output of the MESFET amplifier is indicated by the trace in Figure 5-8(c).

Further experiments are under way to develop front-to-back via holes through the epoxy substrate and to provide heat-sinking to circuit components where it is necessary.

L.J. Mahoney	D.Z. Tsang
C.L. Chen	K.M. Molvar



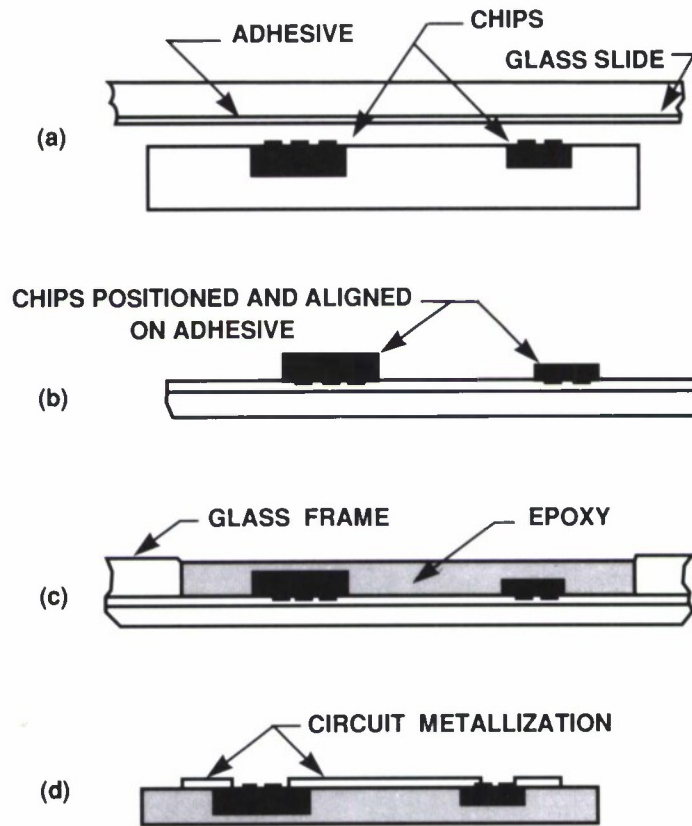


Figure 5-7. Multichip-integration casting technique. (a) IC chips are positioned and planarized with a custom RTV mold, and then affixed to adhesive. (b) RTV mold is removed leaving chips planarized on adhesive in precise alignment. (c) Glass frame is set on the adhesive to define the substrate, and filled with epoxy. (d) Epoxy with chips embedded is separated from the glass and the adhesive is removed. Circuits are then interconnected with standard photolithography and metallization.

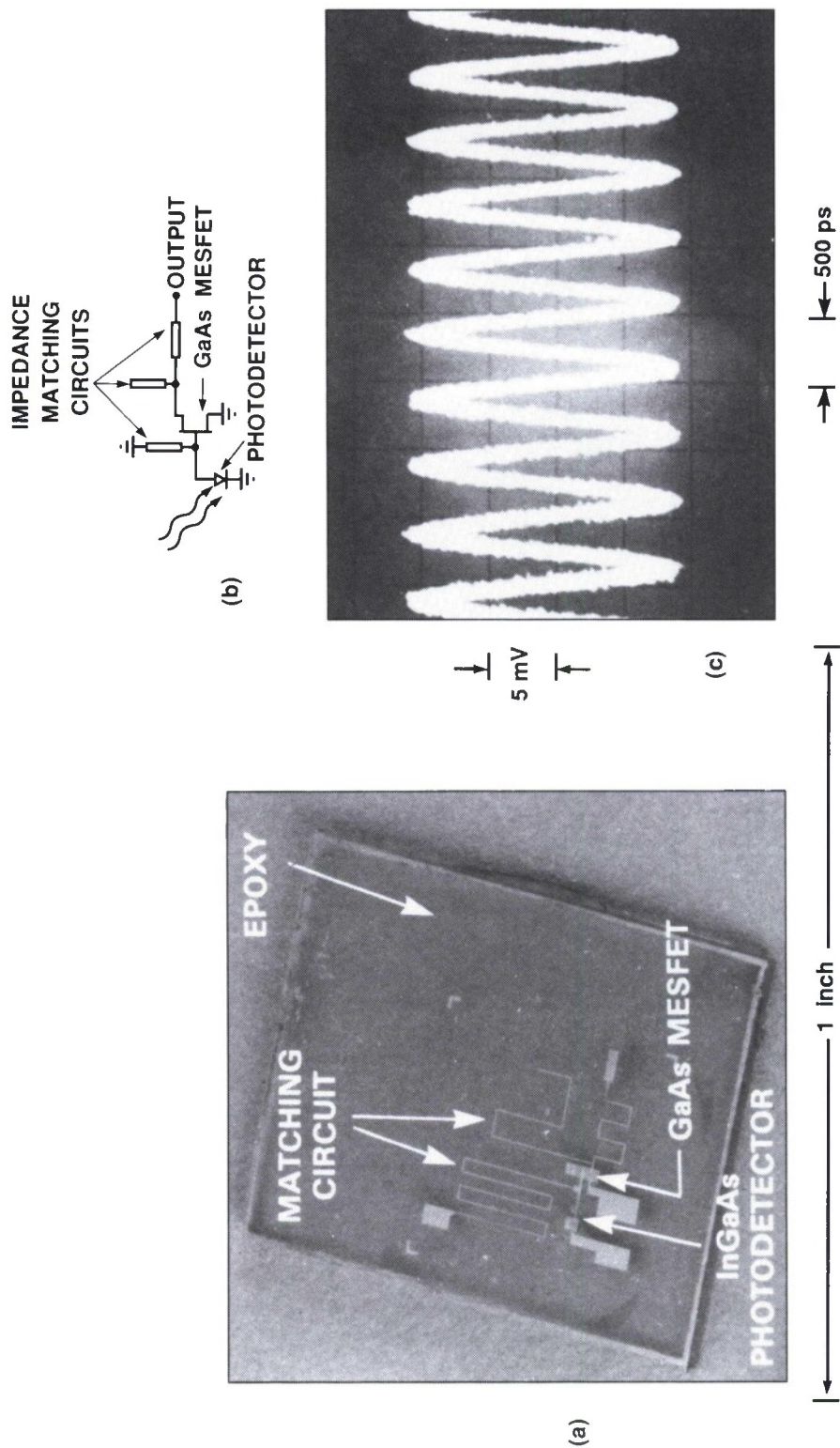


Figure 5-8. (a) Completed multichip optical receiver. (b) Circuit diagram of preliminary test measurement. (c) Measured waveform at the amplifier output in response to a 2-GHz amplitude modulation signal detected by the photodiode.

## REFERENCES

1. E.R. Brown, W.D. Goodhue, and T.C.L.G. Sollner, J. Appl. Phys. **64**, 1519 (1988).
2. E.R. Brown, C.D. Parker, and T.C.L.G. Sollner, Appl. Phys. Lett. **54**, 943 (1989).
3. T.P.E. Broekaert, W. Lee, and C.G. Fonstad, Appl. Phys. Lett. **54**, 1545 (1988).
4. M. Helm, E. Colas, P. England, F. DeRosa, and S.J. Allen, Appl. Phys. Lett. **53**, 1714 (1988).
5. Solid State Research Report, Lincoln Laboratory, MIT (1987:3), p. 56, DTIC AD-192837.

## 6. ANALOG DEVICE TECHNOLOGY

### 6.1 ATOMIC OXYGEN SOURCE FOR SUPERCONDUCTING FILMS

A variety of deposition methods have produced high-temperature superconducting films with very high critical current densities (well above  $10^6$  A/cm<sup>2</sup>).<sup>1-5</sup> With few exceptions, all these methods have two factors in common: (1) the films are deposited onto hot substrates (usually between 600 and 800°C) and (2) some enhanced form of oxidation is used during deposition. Ozone,<sup>5</sup> activated oxygen,<sup>1</sup> atomic oxygen,<sup>3,4</sup> or some form of metallic oxide moieties<sup>6</sup> all have been used with some success. There is little controversy about the need for high temperature during deposition, but it is not yet clear what form of oxygen delivered to the growing film is the most effective.

Cosputtering from three or more metal targets is one of the many methods that have been used to deposit high- $T_c$  superconducting films. At low partial pressures of oxygen, the surface of the targets will remain metallic during sputtering. At higher oxygen pressures, the target surface becomes oxidized. In general, the use of oxidized targets leads to very slow rates of deposition and, possibly, to the bombardment of the substrate by energetic oxygen atoms. Consequently, most researchers have concentrated on finding some method to enhance the oxidation at the substrate level without oxidizing the targets.

One method to accomplish this oxidation is to use an atomic oxygen beam concurrently with the deposition of the metallic species. Microwave sources,<sup>3,4</sup> electron-cyclotron resonance sources,<sup>4</sup> and dc discharge between metallic electrodes<sup>7</sup> have all been used for films deposited by co-evaporation and cosputtering. In this report we describe experiments with an inductively coupled plasma source that has been fabricated for use with a cosputtering system.

In Figure 6-1 we show the configuration of the atomic oxygen source. RF power is coupled inductively to the plasma through a coil. A simple matching network formed by a series and a parallel capacitor allows for the effective coupling of RF power (13.56 MHz). As shown in the figure, the source is composed of two quartz envelopes, an inner one where the gases are injected and an outer one which provides for vacuum integrity of the whole source. This double-envelope construction is necessary since, as described later, any metal part that touches the atomic oxygen increases recombination drastically, reducing the efficiency for the production of atomic oxygen.

A variety of gas mixtures including combinations of oxygen, argon, helium, krypton, nitrogen, hydrogen, water, and nitrous oxide have been used. Only  $O_2 + N_2$ ,  $O_2 + H_2$ , and  $O_2 + H_2O$  produced large enough concentrations of atomic oxygen to be useful. The pressure inside the inner tube used in most experiments is between  $2 \times 10^{-1}$  and  $5 \times 10^{-1}$  Torr.

The measurement of the concentration of atomic oxygen exploits the fact that atomic oxygen will adhere to silver and silver oxide, diffusing rapidly in the metal. In contrast, the sticking coefficient for molecular oxygen is zero. The implementation of this approach<sup>3</sup> for measuring the output of our sources is illustrated in Figure 6-2.



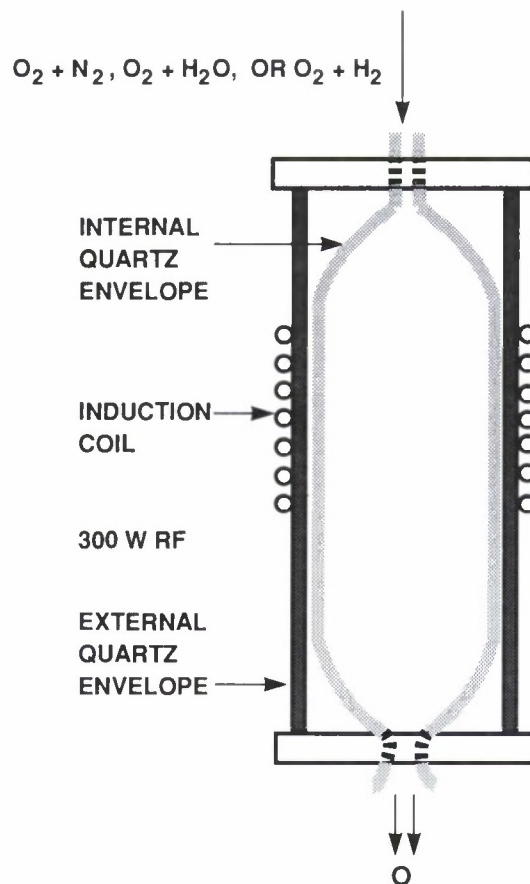


Figure 6-1. Inductively coupled plasma source of atomic oxygen.

Before each run a 1500-Å film of silver is deposited on a quartz-crystal microbalance attached to a table inside the vacuum system. The plasma in the source is ignited and the microbalance is rotated under the atomic oxygen source. The mass added to the crystal can be determined from the change in the oscillation frequency of the crystal. A typical plot of mass gain as a function of time is shown in Figure 6-3.

In the initial part of the curve, the mass gain is determined by the atomic oxygen flux and, in the later part of the curve, by the diffusion of the oxygen into the silver through a layer of silver oxide. To convert the mass gain into an atomic oxygen flux we make two assumptions: (a) that the rate of mass gain for the initial stage of oxide growth is proportional to the atomic oxygen flux, and (b) that the initial sticking coefficient for the atomic oxygen is one. Assumption (b) is probably not correct but, provided that the sticking coefficient is not a strong function of the atomic oxygen concentration, the method still allows us to compare different operating conditions and optimize the source.

Experiments were performed to maximize the flux of atomic oxygen. Very little variation of flux was found for RF powers greater than 250 W, so an RF power of 300 W was used for all the reported measurements. An input molecular oxygen flow of 3 sccm was dictated by the

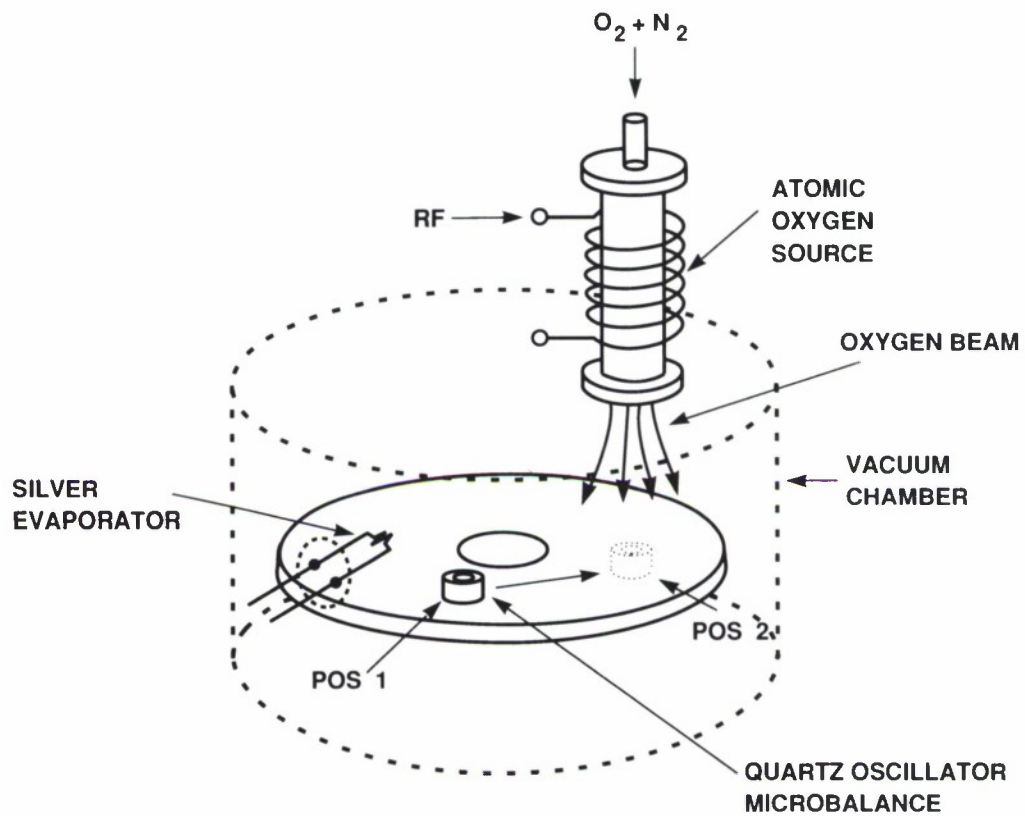


Figure 6-2. Measurement of atomic-oxygen flux by microbalance assay of oxygen captured in silver film.

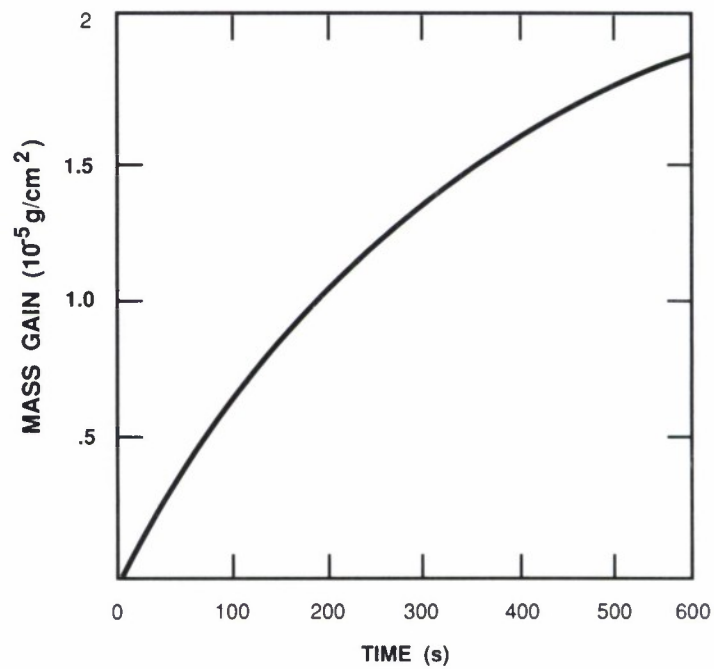


Figure 6-3. Mass gain of silver film bombarded by atomic oxygen as a function of exposure time.

requirement for plasma stability, even though the atomic oxygen flux did not increase significantly for flows above 2 sccm. The flux of atomic oxygen obtained with pure molecular oxygen was very low and it was very difficult to start the plasma. Addition of even a small flow of N<sub>2</sub>, H<sub>2</sub>, or H<sub>2</sub>O increased the flow of atomic oxygen manyfold. The results of these experiments are summarized in Table 6-1.

<p style="text-align: center;"><b>TABLE 6-1</b></p> <p style="text-align: center;"><b>Influence of Gas Flow and Composition on Oxygen Atomic Flux</b></p>			
<b>Auxiliary Gas</b>	<b>Flow (sccm)</b>	<b>Mass Gain Rate 10<sup>-8</sup> g/cm<sup>2</sup>-s</b>	<b>Atomic Oxygen Flux 10<sup>15</sup> Atoms/cm<sup>2</sup>-s</b>
None	—	0.5	0.19
N <sub>2</sub>	4 × 10 <sup>-1</sup>	9.9	3.7
N <sub>2</sub>	3 × 10 <sup>-1</sup>	8.0	3.0
H <sub>2</sub>	2.5 × 10 <sup>-2</sup>	7.5	2.8
H <sub>2</sub>	1.5 × 10 <sup>-2</sup>	9.8	3.7
H <sub>2</sub>	4 × 10 <sup>-2</sup>	5.6	2.1
H <sub>2</sub> O	2 × 10 <sup>-2</sup>	7.0	2.6
H <sub>2</sub> O	5 × 10 <sup>-2</sup>	9.0	3.4

The efficiency of the source is defined as the total flow of atomic oxygen as a percent of maximum possible flow (twice the flow of molecular oxygen). We have measured the atomic flux over the width of the atomic oxygen beam. With the assumption (supported by measurements) that any metallic surface has very high recombination coefficient, so that only direct paths between source and detector are possible, we infer an efficiency of approximately 25 percent.

To avoid oxidation of the metallic targets, we must deliver the atomic oxygen as close to the substrate as possible. To investigate the effect of the transport tube material, we mounted the source at the end of a 48-cm-long stainless-steel pipe that could then be lined with tubes of different materials to be studied. By measuring the flux at the exit end of the tube, a "transmission coefficient" can be calculated. Preliminary results are summarized in Table 6-2. More recent measurements, however, show that the transmission coefficient is a function of the atomic oxygen flux and that, when using the tube, the atomic oxygen is spread over a much larger area.

<b>TABLE 6-2</b> <b>Transmission of Atomic Oxygen Through</b> <b>Tubes of Different Materials</b>	
<b>Tube Material</b>	<b>Flux Transmission Coefficient</b>
Stainless Steel	0.0
Quartz	0.2
Teflon TFA	0.36
Teflon TPFE	0.50

For a typical deposition rate of  $2 \text{ \AA/s}$  the total oxygen flow necessary to fully oxide the superconductive Y-Ba-Cu-O phase is  $8 \times 10^{14} \text{ cm}^{-2} \text{ s}^{-1}$ . As shown in Table 6-1, our atomic oxygen source can provide the necessary flux. However, oxygen flux is attenuated significantly by the transport to the substrate area. Methods of improving the transfer efficiency as well as an absolute calibration of the flux are now under investigation.

A.C. Anderson  
W.T. Brogan

## 6.2 HYBRID ANALOG/DIGITAL CIRCUITRY FOR A SUPERCONDUCTIVE TIME-INTEGRATING CORRELATOR

We have recently completed the design, fabrication, and testing of a superconductive analog signal correlator coupled to on-chip digital readout circuitry. The complete circuit is fabricated using a Nb/Pb tunnel-junction technology and operates at 4.2 K. The block diagram of the superconductive correlator is shown in Figure 6-4. The device consists of a niobium delay line coupled to mixer/integrator/peak-detector (MIP) cells which have been previously described in detail.<sup>8</sup> The function of the delay line is to provide time-delayed wideband signal and reference waveforms to the individual MIP cells. The relative time delay between the two waveforms is linearly increased for each MIP cell along the delay line.

Each MIP cell performs the correlation of the time-delayed analog waveforms provided by the tapped transmission line. The outputs from each of the MIP cells is a binary signal which changes from a "0" to a "1" when the magnitude of the correlation in the respective cell first exceeds a common, externally generated threshold level. These outputs are sent to the binary address encoder for conversion to a digital format representing the location of the MIP cell along the delay line. The Josephson junction-based circuit used in the address encoder was described in detail in Reference 9.



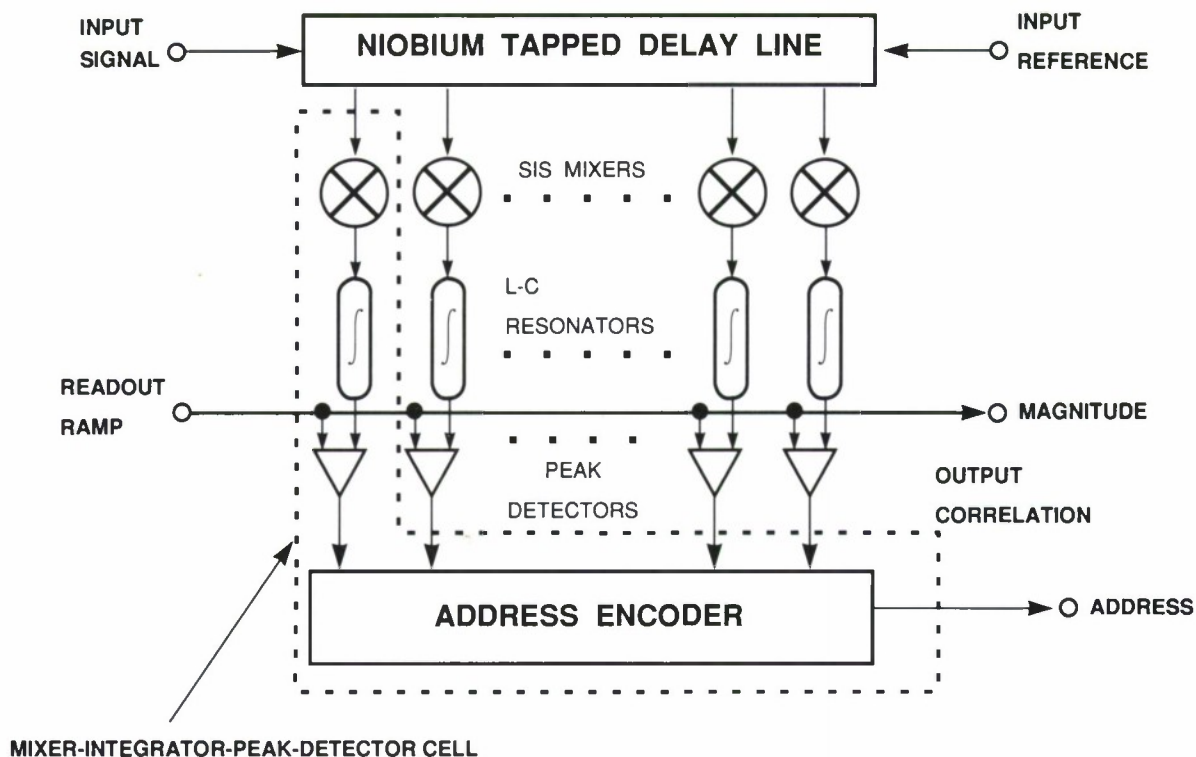
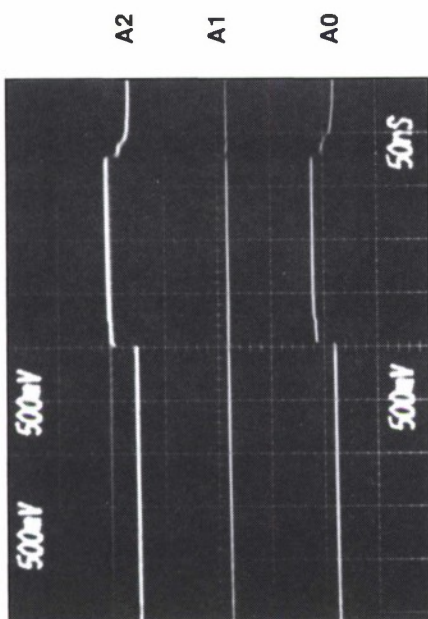


Figure 6-4. Block diagram of superconductive time-integrating correlator. The prototype chip which was tested contains the elements enclosed by the dashed box.

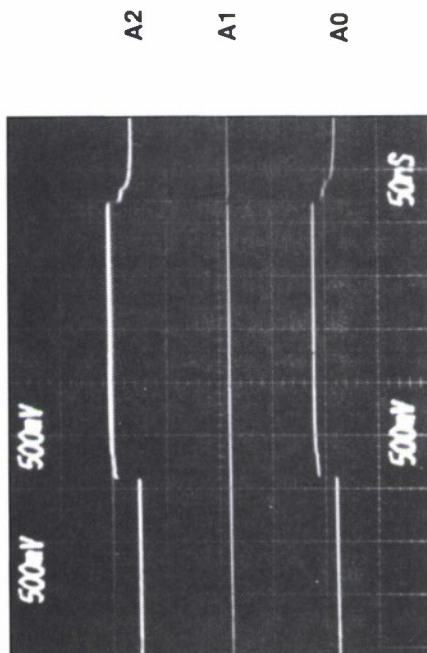
A prototype chip was fabricated and tested which contains the circuitry shown within the dotted line in Figure 6-4. This chip was used to correlate two 4-GHz tones with time durations up to 5  $\mu$ s. Figure 6-5 shows representative results from these tests.

On the left-hand side of Figure 6-5, the top trace represents the time-duration of the 4-GHz waveforms entering the MIP cell. The middle trace shows the address-encoder power-supply current, and the bottom trace shows the ramp current input to the Josephson junction peak-detector circuit. This ramp current effects a linearly *decreasing* threshold for the comparator in the MIP cell. The address-encoder outputs A2, A1, and A0 are shown on the right-hand side of Figure 6-5. For the tested device, the MIP cell was connected to input 5 of the address encoder.

It is observed when the sum of the integrator currents and the peak detector ramp currents exceed the peak-detector's critical current, the peak detector switches to the voltage state, sending its output to the address encoder which then reports that cell number five has fired. The relative timing of the address encoder output reveals the magnitude of the correlation sample as described in Reference 10. Figure 6-5(a) shows typical waveforms for the case where the time-duration of the input waveforms was approximately 0.5  $\mu$ s. Figure 6-5(b) shows the case where the integration was done over a 3- $\mu$ s interval. In (b) it is observed that the address encoder outputs occur



(a)



(b)

→ | ←  
1 $\mu$ s

Figure 6-5. Oscilloscope waveforms showing test structure operation for (a) 0.5- $\mu$ s integration and (b) 3- $\mu$ s integration. The left-hand side shows the input to the MIP cell (top trace), address-encoder supply current (middle), and current input to Josephson junction peak detector (bottom). The right-hand side shows the address-encoder outputs (expanded time scale) during the presence of the peak-detector ramp.

sooner in time. By monitoring the timing of the address encoder outputs in this way, it was inferred that the resonator (integrator) content was variable over a 37-dB dynamic range. The 1-dB compression point occurred for signals  $3\text{ }\mu\text{s}$  long. Based on a 2-GHz input bandwidth, this device should therefore support waveforms with time-bandwidth products equal to 6000.

We have also fabricated a complete integrated circuit containing a 14-channel superconductive time-integrating correlator. A photomicrograph of the device is shown in Figure 6-6. The device measures  $4 \times 2.5\text{ cm}$ . Functional testing is currently under way.

J.B. Green  
M. Bhushan

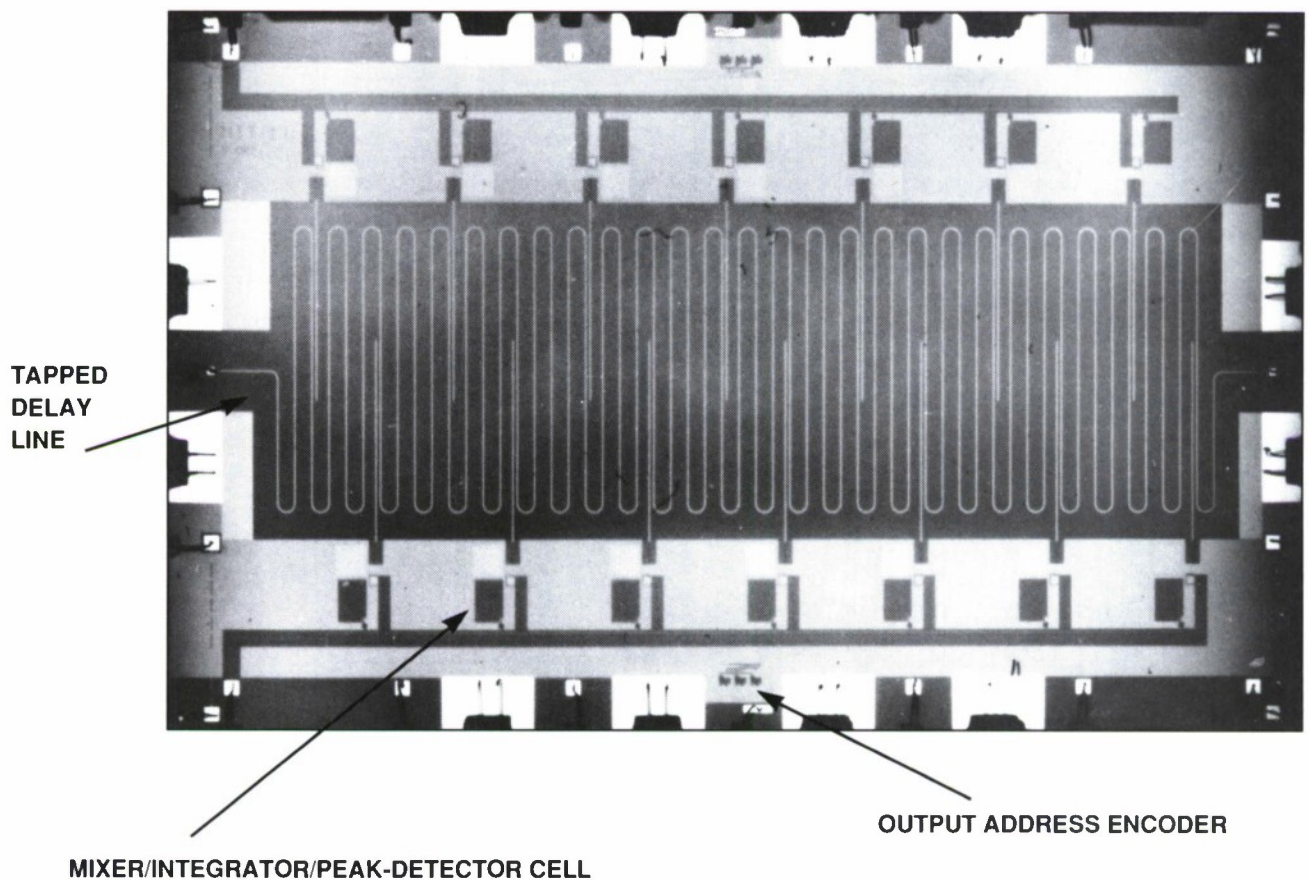


Figure 6-6. Photomicrograph of 14-channel superconductive time-integrating correlator.

126266-44



## REFERENCES

1. D.M. Hwang, T. Venkatesan, C.C. Chang, L. Nazar, X.D. Wu, A. Inam, and M.S. Hegde, Appl. Phys. Lett. **54**, 1702 (1989).
2. X.X. Xi, G. Linker, O. Meyer, E. Nold, B. Obst, F. Ratzel, R. Smithey, B. Strehlau, F. Weschenfelder, and J. Geerk, to be published in Z. Phys.
3. N. Missert, R. Hammond, J.E. Mooij, V. Matijasevic, P. Rosenthal, T.H. Geballe, A. Kapitulnik, M.R. Beasley, S.S. Laderman, C. Lu, E. Garwin, and R. Barton, IEEE Trans. Magn. **MAG-25**, 2418 (1989).
4. T. Terashima, Y. Bando, K. Iijima, K. Yamamoto, and K. Hirata, Appl. Phys. Lett. **53**, 2232 (1988).
5. D.D. Berkley, B.R. Johnson, N. Anand, K.M. Beauchamp, L.E. Conroy, A.M. Goldman, J. Maps, K. Mauersberger, M.L. Mecartney, J. Morton, M. Tuominen, and Y-J. Zhang, IEEE Trans. Magn. **MAG-25**, 2522 (1989).
6. J-J. Yeh, M. Hong, and R.J. Felder, Appl. Phys. Lett. **54**, 1163 (1989).
7. D.G. Schlom, J.N. Eckstein, E.S. Hellman, S.K. Streiffer, J.S. Harris, Jr., M.R. Beasley, J.C. Bravman, T.H. Geballe, C. Webb, K.E. Dessonneck, and F. Turner, Appl. Phys. Lett. **53**, 1660 (1988).
8. Solid State Research Report, Lincoln Laboratory, MIT (1986:2), p. 59, DTIC AD-A180799.
9. Solid State Research Report, Lincoln Laboratory, MIT (1987:3), p. 61, DTIC AD-A192837.
10. J.B. Green, A.C. Anderson, and R.S. Withers, Proc. SPIE **879**, 71 (1988).



